eman ta zabal zazu

Universidad del País Vasco

Euskal Herriko Unibertsitatea

DONOSTIA INTERNATIONAL PHYSICS CENTER

fundación D.I.P.C.

Study of the Geometry and Electronic Structure of Self-Assembled Monolayers on the Au(111) Surface

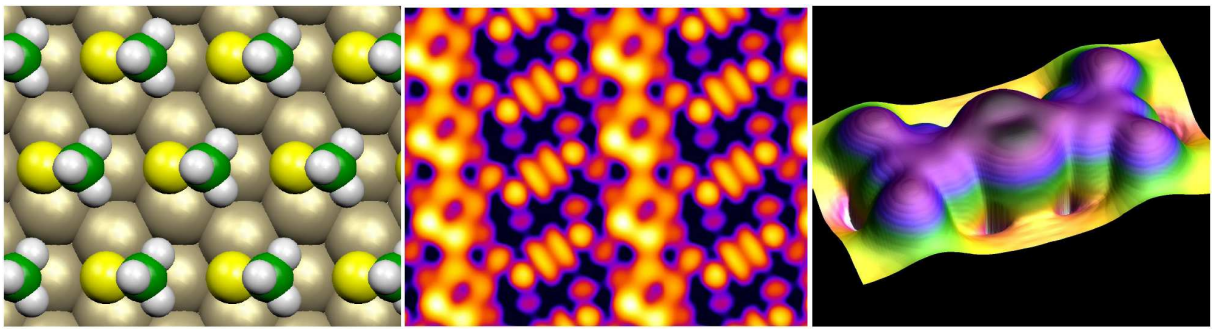

Doctoral Thesis submitted to
The University of the Basque Country
for the Degree of Doctor in Physics

by **Nora Gonzalez Lakunza**

Donostia, November 2008

Cover picture: Relaxed geometries and simulated STM images of three studied systems.

Etxekoei, bihotz-bihotzez

If you shut the door to all errors,
truth will be shut out

Rabindranath Tagore

Study of the Geometry and Electronic Structure of Self-Assembled Monolayers on the Au(111) Surface

Nora Gonzalez Lakunza

Thesis supervisors:

Andrés Arnau Pino

Nicolas Lorente Palacios

author's e-mail: nora.gonzalez@ehu.es

Acknowledgements

Nire tesiari azken ukituak ematen nabilen honetan, eskerrak emateko unea iritsi da. Lau urte pasa dira abentura honetan murgildu nintzenetik... eta hainbat jenderi eskerrak eman behar dizkiot, non ez bait dakit lerro hauek nahikoak izango diren.

En primer lugar, quiero dar las gracias a mi director de tesis, Andrés Arnau, que me ha guiado magnificamente desde el principio. Su total disponibilidad, y su interés por este trabajo, han sido una ayuda inestimable para llevarlo a buen puerto. Gracias también a mi codirector Nicolás Lorente, que con su buena disposición, se ganó una estudiante más. Desde la distancia también ha contribuido activamente. Los dos han formado un buen equipo instructor que me ha enseñado un montón de física.

Pero esta tesis no hubiera sido posible sin la colaboración con los experimentales. Ellos me abrieron las puertas de sus laboratorios y me mostraron los secretos del STM. Muchísimas gracias a Kike Ortega, y Nacho Pascual por contar conmigo. Especialmente a Nacho, que tan bien me acogió en su grupo en Berlin. Y como no, gracias a Miguel Ruiz e Isabel Torrente. Trabajar con vosotros ha sido un placer... pero aún mayor placer compartir tan buenos momentos. ¡Gracias chicos por hacer de Berlin una ciudad inolvidable!

No puedo dejar de agradecer a Pedro Miguel Echenique el que me brindara la oportunidad de trabajar en su grupo. Gracias a ello he vivido la experiencia única que supone un doctorado, más si cabe en tan ejemplar entorno de trabajo aquí en Donostia, a caballo entre el departamento de física de materiales y el DIPC. Gracias por poner a mí disposición tantos recursos, que tanto han enriquecido esta experiencia. Bestalde, Euskal Herriko Unibertsitatetik, lau urte hauetan zehar jasotako finantziazioa ere eskertu beharra dut.

Aquí hay mucha gente de la que me quiero acordar. Quiero agradecer a las secretarias del DIPC, Ana, Marimar, y Amaia, sus gestiones, y sobre todo sus sonrisas en el edificio 1. Vaya mi agradecimiento también a Patxi, el secretario del departamento de materiales, y a Tomás el guarda del DIPC, que a su manera hacen que las cosas funcionen. Mención aparte se merece el equipo de informáticos del DIPC, Txomin, Belen y Carmen. Gracias por vuestra ayuda, por estar siempre dispuestos a solventar cualquier problema relacionado con las máquinas, y sobre todo por vuestra paciencia. Gracias a toda la gente con la que he ido compartiendo cosillas, las comidas, los cafés, las conferencias, Javi, Pepa,

Aran, Thomas, Iñaki, Laura, Fred, Martina y un largo etcetera.

Y no me olvido de los mejores compañeros de despacho. Durante mi primer año en químicas, Iñigo, que me introdujo en el maravilloso mundo del software libre, latex y demás historias. Luego en el hexágono, Isabel, Marina, Maia, Aritz, Aitzol, y Sampsa. Nos hemos ayudado en cuestiones burocráticas varias y además hemos compartido muy buenos momentos, charlas filósoficas, y no tan filosóficas. ¡Una pena, que las máquinas nos echaran!

Honaino ekarri nauen bidea luzea izan da, eta jende askok jarri du bere apurra. Leioan, fisikako karrera haseran nire ikaskideak, Edith, Yoli eta Aitzi aipatu nahi nituzke. También, a mis colegas de la complu en Madrid. Compañeros de clase, de piso, de mus y de juergas. Mónica, Jose, Angel, Dani, Natalia,... aparte de buenos recuerdos me alegra conservar también vuestra amistad. Ya lejos, pero "La nave roja vive".

Eta zientzia eta unibertsitatetik kanpo bizitza ere badagoenez, urteetan horren lekuko izandako nere betiko lagunak ere aipatu behar. Batez ere Olatz, berak ongi bait daki zertaz doan guzti hau! Baita ere netaz eta nere tesiaz arduratu diren, osaba, izeba, eta lehengusuak. Eskerrik asko denei, zuen artean fisikari bat onartzeagaitik!

Eta azkenik, guztien gainetik etxekoei nire eskerrik beroenak eman nahi dizkiet. Zuek gabe hau ez zan posible izango! Anaiari, beti beste ikuspuntu bat erakusteagaitik. Aita eta amari, baldintzarik gabeko laguntza eta maitasuna beti eman izana. Ezin hitzez esan zenbat zor dizuedan, zuen ahaleginei esker honaino iritxi naiz. Eta noski, Xantiri, azken urteotan nire euskarria zentzu orotan (baita ekonomikoan ere!). Eskerrak eman nahi dizkizut beti bertan egoteagaitik, baina batipat gorabehera guztien gainetik, amaieran, irrifar arazten nauzulako. Mila esker txiki!

Nora Gonzalez Lakunza,
Donostian, November 14, 2008

Contents

Chapter 1

Introduction

In 1965, Gordon E. Moore, co-founder of Intel corporation, predicted that the number of transistors that could be placed inexpensively on an integrated silicon circuit would be doubled approximately every two years [1]. This exponential growth became known as Moore's law. This trend has continued since then, going from just over 2000 transistors to over 1 billion transistors per integrated circuit. As the number of transistors has increased, there has been also a corresponding decrease in the size of the transistor minimum feature, from 10 micrometers to 45-65 nanometres in 2007, roughly 180 silicon atoms long. During such miniaturisation, engineers have coped with various technological difficulties. However, as it enters the nanoscale and approaches the atomic limit, scientist and engineers have to tackle more fundamental problems. The physics at the nanoscale follows the laws of quantum mechanics. Thus, our macroscopic knowledge does not result applicable.

The conception of manipulating individual atoms and molecules by adequate precise tools was already suggested by Richard Feynman is his famous talk "There's Plenty of Room at the Bottom" in 1959 [2]. He noted that, as one goes down in size, a number of interesting problems arise because all things do not simple scale down in proportion. For example, gravity would be negligible as compared to van der Waals forces. His idea was not only to create smaller components, but to make them functionals too. It was later in 1974, when Norio Taniguchi coined the term "nanotechnology" [3], which refers to the applied science that aims at controlling matter at the atomic and molecular scale. This control requires a thorough understanding of the physics and chemical reactions that govern at this scale. The invention of the Scanning Tunneling Microscope (STM) in 1981 by G. Binning and H. Rohrer [4] has been of great help in the development of nanotechnology, because it allowed direct visualisation at the atomic scale.

Two main approaches are used in nanotechnology: (i) the *top-down* approach that seeks to create smaller devices by using larger entities, and (ii) the *bottom-up* approach,

where devices are built up from molecular components that self-organised to form complex assemblies [5–7]. The former descends directly from the conventional solid-state silicon methods for fabricating microprocessors, while the latter stands on molecular recognition and supramolecular chemistry [8, 9]. There has been a strong motivation in developing functional nanomaterials, with unique properties arising from their nano-dimension, both from a technological and scientific point of view. Much of the fascination with nanomaterials stems from the size related quantum and surface phenomena that matter exhibits. Nanotechnology or nanoscience is a multidisciplinary field, where physics, chemistry and biology meet, and hence, different techniques from different fields have been adopted to develop such new materials.

Particularly, organic thin films have attracted considerable attention over the last decades [10]. This thesis is concerned with the study of self-assembled organic films adsorbed on different substrates, the so-called, Self-Assembled Monolayers (SAMs). Different strategies have been used to grow SAMs of different nature, ranging from hydrogen bonded networks of saturated planar molecules to surfactants with specific headgroup affinity to a given surface, as well as nanoporous patterns of metal–organic networks. In fact, the design of films with tailored properties requires a better understanding of the driving forces in the self-assembly process. The relative strength of the interactions present in the system plays an important role in determining the structure of the monolayer. In cases where the interactions between the adsorbates (molecules or atoms) and the substrate are weak, e.g., van deer Waals forces, as compared to the interaction between adsorbates, e.g., hydrogen bonds, the overlayer structure is mainly determined by the adsorbate–adsorbate interaction, and the substrate acts like a template on which the 2D network lands. However, when adsorbate–substrate interactions are stronger, e.g., covalent bonds, than the corresponding adsorbate–adsorbate interactions, e.g., van der Waals forces, the interactions between adsorbates play a second role, and the SAM structure tends to be commensurate with the substrate lattice. Finally, when both adsorbate–adsorbate and adsorbate–substrate interactions are of comparable strength, as it is the case of water adsorption on solid surfaces [11], the optimal structures are hard to guess.

In this work we study three different cases of distinct molecules adsorbed on clean Au(111) surfaces. The choice of each system was motivated by STM experimental results. However, we have not restricted ourselves to interpretate the experiments, but tried to shed some light on the underlaying physics that originate such arrangements and electronic properties in each case. The *ab-initio* calculations are a powerful method to test different hypothesis about the origin of the observed physical phenomena. Indeed, our main tool in this thesis has been Density Functional Theory (DFT) based first-principle calculations [Chapter 2].

The starting point of this thesis is the study of alkanethiolates on Au(111) and, spe-

cially, the zig-zag structure observed in STM images. Alkanethiolates are characterised by a headgroup that contains sulphur and a chain or backbone made of carbon and hydrogen atoms. The sulphur-head binds to the Au surface whereas the backbone stands or tilts depending on the coverage. The self-assembly stems from the site selective adsorption and from the weak dispersive interaction between neighbouring backbones. What really raised our interest in such system was the understanding of the singular S–Au interaction [Chapter 3]. Furthermore, the body of the thesis has been organised around this S–Au interaction. We have followed a sequence regarding the relative adsorbate–substrate interaction strength: from stronger to weaker.

Following this criteria, the next system under study is a mixture of tetrathiafulvalene (TTF) and 7,7,8,8-tetracyanoquinodimethane (TCNQ) on Au(111) [Chapter 4]. As TTF has sulphur atoms, it interacts in a similar manner to the thiolates, while TCNQ has weaker interactions with the surface. TTF-TCNQ on Au(111) can be considered as an example of comparable adsorbate–adsorbate and adsorbate–substrate interactions. Apart from the presence of one molecule with sulphur, that will interact quite strongly with Au, they also form a donor–acceptor complex, which could make the system rather interesting for molecular electronics.

The third and last system, naphtalene tetracarboxylic diimide (NTCDI) and 1,4-bis(4,6-diamino-1,2,5-triazin-2-yl)benzene (BDG) co-adsorbed on Au single crystals is the limiting example of weak adsorbate-substrate interaction [Chapter 5]. NTCDI and BDG are planar organic molecules with extended π-systems, that contain complementary amine and imide functional end groups. We are aware that DFT is limited to describe correctly the weak interaction between these planar molecules and the Au(111) surface. However it turns out to be able to describe the bidimensional supramolecular assembly, and a helpful complementary tool to interpretate the experimental results (e.g., NEXAFS).

All studied systems share the same substrate, the Au(111) surface. Thus, an appendix has been devoted to this (111) noble metal face that has a surface state close to the Fermi level and a characteristic surface reconstruction [Appendix I]. In many cases, changes in both characteristics can be used to trace down the adsorbate–substrate interaction. They are also used by experimentalist to prove the cleanliness or perfection of a given sample, and upon molecular adsorption, the surface state's energy is used to check the state of the tip during the STM measurements. As regards theoretical calculations, the well known surface state serves also as a benchmark of the accuracy of the metal slab description used in the calculations.

Chapter 2

Methodology

In this chapter we present a brief overview of Density Functional Theory (DFT) for solving the many-body problem, and a simple description of the Vienna Ab-initio Simulation Package (VASP) plane wave based code that has been used in the calculations. In addition to this, the methodology used for slab calculation and various miscellaneous tools are described in detail.

The scope of this chapter is not to present a scholarly review of DFT, nor to describe in detail the implementation of the method used by the VASP code, but rather to introduce the conceptual basis of DFT and the notation used troughout this work. The definitions of the different physical quantities required to study the electronic structure of the systems are also introduced.

2.1 Density Functional Theory

Density functional theory (DFT) [12, 13] has long been used for electronic structure calculations in solid-state physics and in quantum chemistry. This is because it provides a useful balance between accuracy and computational cost, allowing much larger systems to be treated than other *ab-initio* methods. Nowadays, traditional wavefunction methods, either variational or perturbative, can be applied to find highly accurate results on small systems providing benchmarks for developing exchange-correlation functionals, which can then be applied to much larger systems.

Density functional theory is a completely different, formally rigorous, way of approaching any interacting problem, by mapping it exactly to a much easier-to-solve non-interacting problem. Its methodology is applied in a large variety of fields to many different problems [14–16].

To give an idea of what DFT is all about, we first recall some elementary quantum

mechanics. In quantum mechanics we learn that all the information we can have about a system is contained in the system's wavefunction, Ψ. We work in the Born-Oppenheimer approximation in which the ions and electrons are decoupled, i.e., for the electrons the ion coordinates are parameters, thus, we only want to solve the ground-state quantum mechanical problem for the electrons. The nuclear degrees of freedom (e.g., the crystal lattice in a solid) appear only in the form of an external potential $v(\mathbf{r})$ acting on the electrons, so that the wavefunction depends only on the electronic coordinates[1]. For non-relativistic systems[2], this wavefunction is calculated by solving the Schrödinger equation, which for a single electron moving in a $v(\mathbf{r})$ potential reads[3]

$$\left[-\frac{1}{2}\nabla^2 + v(\mathbf{r})\right]\Psi(\mathbf{r}) = \varepsilon\Psi(\mathbf{r}). \tag{2.1}$$

If there is more than one electron, due to the electron–electron interaction $V_{ee}(\mathbf{r}_i, \mathbf{r}_j)$, one has a many-body problem:

$$\left[\sum_i^N \left(-\frac{1}{2}\nabla_i^2 + v(\mathbf{r}_i)\right) + \sum_{i<j} V_{ee}(\mathbf{r}_i, \mathbf{r}_j)\right]\Psi(\mathbf{r}_1, \mathbf{r}_2..., \mathbf{r}_N) = E\Psi(\mathbf{r}_1, \mathbf{r}_2..., \mathbf{r}_N), \tag{2.2}$$

where N is the number of electrons.

For a Coulomb system, the only type of system considered here, one has

$$\hat{V}_{ee} = \sum_{i<j} V_{ee}(\mathbf{r}_i, \mathbf{r}_j) = \sum_{i<j} \frac{1}{|\mathbf{r}_i - \mathbf{r}_j|} = \frac{1}{2}\sum_{i,j} \frac{1}{|\mathbf{r}_i - \mathbf{r}_j|}. \tag{2.3}$$

The main problem solving Eq. (2.2) is its great demand of computational resources, because the wavefunction depends on $3N$ coordinates. However, the particle density; defined by,

$$n(\mathbf{r}) = N \int d^3r_2 ... \int d^3r_N |\Psi(\mathbf{r}, \mathbf{r}_2..., \mathbf{r}_N)|^2; \tag{2.4}$$

only depends on 3 coordinates. It is here where DFT makes the difference. DFT is an exact formulation of the ground-state of an arbitrary inhomogeneous many-electron system, that uses the particle density of the system, $n(\mathbf{r})$, as a key variable.

DFT is based on two theorems probed by Hohenberg-Kohn in 1964 [17]. According to the first theorem, given a ground-state density, $n_0(\mathbf{r})$, it is possible, in principle, to determine uniquely the corresponding ground-state wavefunction, $\Psi_0(\mathbf{r}_1, \mathbf{r}_2..., \mathbf{r}_N)$. In other words, there is a one-to-one mapping between the ground-state density and the ground-state wavefunction of a many-body system. This means that *any* property of the

[1] To simplify notation spin will not be considered explicitly.

[2] Should one aims to include relativistic effects, one must solve Dirac's equation instead.

[3] Unless otherwise noted, we use atomic units throughout this text: $e^2 = \hbar = m = 1$

system can be viewed as a functional of the ground-state density (n_0). According to the second theorem, the ground-state density minimises the total energy of the system:

$$\frac{\delta E[n]}{\delta n(\mathbf{r})} - \mu = 0, \tag{2.5}$$

where μ is a Lagrange multiplier that assures particle conservation, i.e., $\int d^3r\, n(\mathbf{r}) = N$. However, despite the conceptual advance represented by these theorems, they do not lead to a practical advance in real calculations, because they provide no guidance for constructing the unknown energy functionals.

A classical approach for solving the many-body equation, Eq. (2.2), consists in "building" a system of N *non-interacting* electrons in some effective potential, $v_s(\mathbf{r})$, that mimics the true electronic system. Because this is a non-interacting system, the coordinates decouple and its wavefunction is simply a product or a sum of products of one-electron wavefunctions, called orbitals, satisfying:

$$\left[-\frac{1}{2}\nabla^2 + v_s(\mathbf{r})\right]\phi_i(\mathbf{r}) = \varepsilon_i\phi_i(\mathbf{r}), \tag{2.6}$$

where $\Psi(\mathbf{r}_1, \mathbf{r}_2..., \mathbf{r}_N) = \phi_1(\mathbf{r}_1)\phi_2(\mathbf{r}_2)...\phi_N(\mathbf{r}_N)$ in the Hartree [18] approximation[4], or it is a single Slater determinant [19, 20] in the so-called Hartree-Fock approximation [21], in order to have an antisymmetric wavefunction. Since the electrons are fermions, the wavefunction has to be antisymmetric with respect to the exchange of the coordinates of two particles. Quantum chemistry methods rely on different approximations to the wavefunction which go beyond the single Slater determinant.

This set of equations, Eq. (2.6), are much simpler to solve since they only have 3 coordinates. The effective potential in those equations depends on the electron density, which in turn is calculated from the solution to the set of equations. Therefore, they have to be solved self-consistently. An initial guess is made for the potential, the eigenvalue problem is then solved, the density calculated, and a new potential found. Repeating these steps iteratively until there is no change in the output from one cycle to the other, i.e., until the self-consistency is reached. This method yields to an approximated energy, because the true wavefunction is not a sum of products of single particle orbitals. The difference between the Hartree-Fock energy and the exact ground-state energy is called the correlation energy:

$$E_c = E - E_{HF} \tag{2.7}$$

In an interacting electron system the exchange energy is due to the fact that two electrons

[4]Within this approximation, the fact that the electrons are correlated as a result of the Coulomb interaction between them is ignored, as well as the fact that the many-body wavefunction of electrons must be antisymmetric.

with the same spin cannot occupy the same site, that is the Pauli exclusion principle; and the correlation appears as a result of the Coulomb repulsion between the electrons.

In the framework of DFT, the Kohn-Sham equations [22] share the same spirit as the Hartree equations. The Kohn-Sham (KS) system is simply an auxiliary system of non-interacting electrons, chosen to have the same electron density as the physical interacting system. Then, DFT looks formally like a single-particle theory, although many-body effects are still included via, the so-called exchange-correlation (XC) functional. The KS orbitals are given by Eq. (2.6) and yield[5]

$$n(\mathbf{r}) = \sum_{i=1}^{N} |\phi_i(\mathbf{r})|^2. \tag{2.8}$$

The total energy can be written as a functional of the density,

$$E[n] = T[n] + V_{ee}[n] + \int d^3r\, n(\mathbf{r}) v(\mathbf{r}), \tag{2.9}$$

and this, further rewritten in terms of the non-interacting kinetic energy T_s:

$$E[n] = T_s[n] + E_H[n] + \int d^3r\, n(\mathbf{r}) v(\mathbf{r}) + E_{xc}[n], \tag{2.10}$$

where we have included explicitly the Hartree energy term (or the classical electrostatic interaction) by

$$E_H[n] = \frac{1}{2} \int d^3r \int d^3r'\, \frac{n(\mathbf{r}) n(\mathbf{r}')}{|\mathbf{r} - \mathbf{r}'|}. \tag{2.11}$$

The rest is called the exchange-correlation energy, $E_{xc}[n]$. Now, from the functional dependence of $E[n]$ [see Eq. (2.5)], we can extract the potential felt by non-interacting electrons of the same density:

$$v_s(\mathbf{r}) = v(\mathbf{r}) + V_H(\mathbf{r}) + V_{xc}(\mathbf{r}), \tag{2.12}$$

where V_H is the Hartree potential,

$$V_H(\mathbf{r}) = \int d^3r'\, \frac{n(\mathbf{r}')}{|\mathbf{r} - \mathbf{r}'|}, \tag{2.13}$$

[5] At finite temperature, the occupation number of a state i is governed by the Fermi-Dirac distribution function, $f_i = \frac{1}{e^{(\varepsilon_i - \mu)/k_B T} + 1}$, and electron density is given by, $n(\mathbf{r}) = \sum_{i=1}^{N} f_i |\phi_i(\mathbf{r})|^2$.

and V_{xc} is the exchange-correlation potential given by,

$$V_{xc}(\mathbf{r}) = \frac{\delta E_{xc}[n]}{\delta n(\mathbf{r})}. \tag{2.14}$$

So far, the KS equations are exact and give the exact ground-state density, but the unknown exchange-correlation energy has to be approximated. The simplest approximation within DFT is the local-density approximation (LDA). There, the system is assumed to behave locally as a homogeneous electron gas of density $n(\mathbf{r})$, and the XC functional is written as

$$E_{xc}^{LDA} = \int d^3r\, n(\mathbf{r}) \varepsilon_{xc}^{hom}[n(\mathbf{r}))]. \tag{2.15}$$

In a homogeneous system, i.e., the uniform electron gas, the exchange energy can be easily evaluated ($\varepsilon_x^{hom}[n]$). There, the electrons sit in an infinite region of space, with a uniform positive external potential chosen to preserve overall charge neutrality. Still, the correlation part ($\varepsilon_c^{hom}[n]$) needs to be approximated. Nowadays, this is done based on different parametrisations [23–25] of highly precise Quantum Monte Carlo (QMC) calculations for the uniform electron gas [26]. LDA has been proved to be surprisingly successful, even for systems quite different from the uniform gas, basically thanks to some sum rules.

LDA exploits the knowledge of the density at point $\mathbf{r}$. Nevertheless, any real system is inhomogeneous, i.e., its density varies spatially. Hence, it would be interesting to include some information about the rate of this variation ($\nabla n(\mathbf{r})$). This leads to the so-called generalised-gradient approximations (GGAs) [27],

$$E_{xc}^{GGA} = \int d^3r\, f[n(\mathbf{r}, \nabla n(\mathbf{r})]. \tag{2.16}$$

The choice of the function $f[n, \nabla n]$ gives rise to different GGA parametrisations [28–31]. Quite generally, current GGAs seem to give reliable results for all main types of chemical bonds (covalent, ionic, metallic and hydrogen bond). However, for van der Waals or dispersion interactions, both GGA and LDA fail.

The KS equations are solved self-consistently as follows: For a given guess of the ground-state electron density ($n(\mathbf{r})$), one evaluates the potential of Eq. (2.12) and finds the eigenfunctions (ϕ_i) and eigenvalues (ε_i) of Eq. (2.6). Then, using Eq. (2.8) one calculates a new ground-state density, and starts again. This process is repeated iteratively until it converges[6]. Once one has a converged solution n_0, the total energy can be calculated from Eq. (2.10). It is important to note, that eigenstates and eigenvalues of the non-interacting system are just auxiliary quantities that yield the correct ground-state electron

[6]It follows the same procedure as Hartree approximation.

density. From now on, they are referred to as KS states. It is only the density that has strict physical meaning, while the KS spectrum does not correspond to the true energy spectrum.

2.2 Plane Waves

The ground-state calculations presented through this thesis have been performed within DFT using the Vienna Ab-Initio Simulation Package (VASP) [32,33]. This is a package for performing *ab-initio* quantum-mechanical simulations using a plane wave basis set, that has implemented LDA and different GGA parametrisations for exchange and correlation. Furthermore, the interaction between ions and electrons is described by ultra-soft Vanderbilt pseudopotentials [34] or by the Projector-Augmented Wave method (PAW) [35]. The fundamental idea of a "pseudopotential" is to replace the real potential of the nucleus and the effects of the strongly bound core electrons by an effective ionic potential acting on the valence electrons. Hence, they represent a smooth approximation of the real interaction potential for the valence electrons close to the nuclei. There are different approaches to build these pseudopotentials. One can use auxiliary localised functions to define ultra-soft pseudopotentials, or express the valence wavefunctions as a sum of smooth functions plus core functions, which leads to the PAW method.

In the present study, we use the PW91 parametrisation by Perdew and Wang [30] for the exchange and correlation, together with the PAW method to treat ion–electron interactions.

To calculate the total energy of solids, a plane wave expansion of the Kohn-Sham (KS) orbitals is very useful, as it takes advantage of the periodicity of the crystal. According to Bloch's theorem, the KS eigenstate can be written as

$$\phi_{n,\mathbf{k}}(\mathbf{r}) = e^{i\mathbf{k}\cdot\mathbf{r}} \sum_{\mathbf{g}} a_{n,\mathbf{k}}(\mathbf{g}) e^{i\mathbf{g}\cdot\mathbf{r}}, \tag{2.17}$$

where $\mathbf{k}$ is the wavevector, n the band index, and $\mathbf{g}$ the reciprocal lattice vectors [36, 37]. The corresponding eigenvalues, $\varepsilon_{n,\mathbf{k}}$, form the energy band structure of the periodic system.

The solutions to the Schrödinger equations are periodic in $\mathbf{k}$, hence, all unique solutions are given by the wavevectors in one primitive cell of the reciprocal lattice, which is chosen to be the first Brillouin Zone (BZ). This is a unique cell because Bragg scattering can occur at its boundaries, leading to special features at the BZ boundary, such as the ones reported in Chapter 4. The sampling of k-points needed in the calculation depends very much on the unit cell of the system, the larger the cell in real space the smaller

in reciprocal space, thus, for large cells less number of k-points are required to achieve the same precision. In principle, one has to sample the whole Brillouin Zone, but taking advantage of the space group symmetry of the lattice, this often can be restricted only to the Irreducible Brillouin Zone (IBZ) with some reasonable scheme. Thoughout this work, we use the Monkhorst-Pack scheme [38], where M×N×L means a sampling of M, N and L equidistant points along the first, second and third reciprocal vectors, respectively. For very large systems, we use only the Gamma point (Γ), that corresponds to the centre of the BZ, i.e., $\Gamma \equiv \mathbf{k} = (0, 0, 0)$.

For finite systems, where the periodicity is lost, like atoms, molecules, or clusters, plane waves can also be used, within the *supercell* approach. In those cases, the finite system is placed in a fictitious periodic crystal, that contains the system itself and enough vacuum around to avoid interactions between neighbouring cells. The drawback of this method is that a very large number of plane waves is needed as the electronic density is concentrated on a small fraction of the total volume of the supercell. For such systems, a localised basis set would be more efficient, in contrast to the case of crystals.

We are concerned with the adsorption of molecules on a surface, but before tackling this specific problem, there are some previous steps that have to be done. The different stages in the methodology followed to calculate the adsorption of molecules on a metal substrate are schematically depicted in Fig. 2.1, that includes the concept of supercell introduced before.

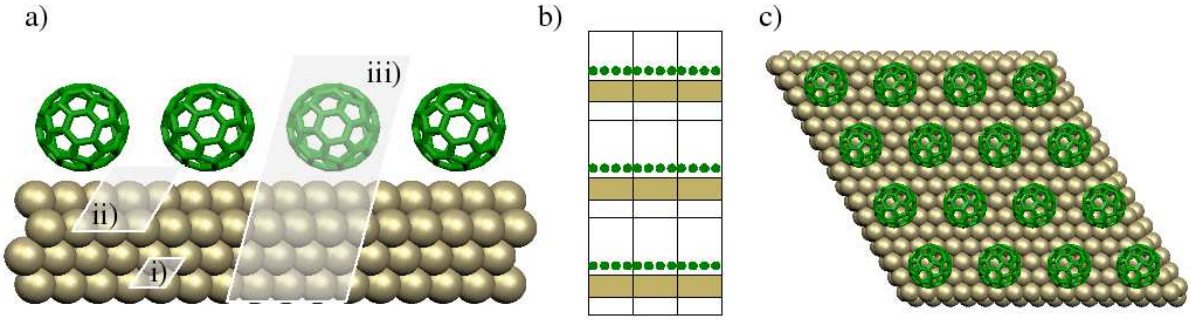

Figure 2.1: Scheme of the supercell method. a) Representation of the different steps and corresponding unit cells used to simulate the adsorption of a molecule on a substrate. b) and c), show respectively the side and top view of the periodic supercell.

First of all, we perform a *bulk* calculation of the bare metal, to get its theoretically optimised bulk lattice constant [see i) from Fig. 2.1a)]. In the case of Gold, we obtain a lattice constant of 4.17 Å, which compares reasonably well with the experimental value of 4.08 Å [39].

Next, the surface we are interested in, e.g. Au(111), has to be described. Surfaces are periodic in the bidimensional (2D) plane, but they lose their periodicity in the z-direction.

Therefore to simulate this, the concept of *supercell* or *slab* has to be used. The unit cell of a surface is made of a given number of atomic planes, with a relaxed interlayer distance, and an empty region of several Å along the z-direction [see ii) in Fig. 2.1a)]. Finally, the adsorbates are placed on top of this slab[7], and a full ionic relaxation of the system is performed [see iii) in Fig. 2.1a)]. We use 3D periodic boundary conditions (PBC), which means that this supercell (metal surface + adsorbate + vacuum) will be repeated periodically as depicted in Fig. 2.1b) & 2.1c). The vacuum region has to be large enough to avoid residual interactions with periodic images along the vertical.

It is very important to perform convergency tests, over k-point sampling, size of the cell for finite systems, and specially with a very critical parameter, namely the energy cutoff, that controls the number of plane waves to be included in the calculation for each k-point.

Once one has followed all these previous steps, and has calculated the ground-state electronic structure of a given relaxed system to a desired accuracy[8], one can use different theoretical tools to extract information from the wavefunctions[9] (or charge density), and try to understand the underlaying physics. This post-processing allows us to identify the adsorption sites and geometry of given molecules, and offers a powerful complementary tool for the interpretation of various experiments in surface physics, such as, scanning tunneling microscopy (STM), scanning tunneling spectroscopy (STS), near-edge X-ray absorption fine structure (NEXAFS), high resolution electron energy loss spectroscopy (HREELS), among others.

2.3 Miscellaneous tools

In the present study, we have used the commercial VASP code, but we have also made various auxiliary post-processing programs, mainly in Fortran, in order to handle the raw output of the code, to plot charge densities, or simulate STM images, etc. Furthermore, we have implemented a new tool to calculate Projected Density of States (PDOS) on Molecular Orbitals (MO) from VASP, that will be described in detail in this section.

[7] In some cases, symmetric slabs are more appropriate, with adsorbates placed in both sides of the slab.

[8] Electronic relaxation to a given accuracy in energy, and relaxation of the atomic position to get forces lower than a tolerance value.

[9] Recall that they are the solution to the KS equation, thus, in principle, they do not have a physical meaning. However in practice they can be considered as "approximations" to the real GS electronic states.

2.3.1 Binding energy

The binding energy (or adsorption energy) of one molecule or atom adsorbed on a surface is defined by

$$E_b = E_{Surf+Ads} - E_{Surf} - E_{Ads}, \tag{2.18}$$

where $E_{Surf+Ads}$ is the total energy of the complete system, E_{Surf} the total energy of the clean surface and E_{Ads} is the total energy of the corresponding adsorbate. All total energies are negative, therefore according to this definition, it must be noted that a negative binding energy implies a stabilisation of the Surface–Adsorbate complex.

2.3.2 Induced electron density

Following a standard method of analysis, we can also compute the adsorption induced electron density[10], defined as follows

$$\rho_{\text{ind}} = \rho(Surf + Ads) - \rho(Surf) - \rho(Ads), \tag{2.19}$$

where $\rho(Surf+Ads)$ denotes the electron density of the whole complex, $\rho(Surf)$ the electron density of the clean surface and $\rho(Ads)$ the density of each adsorbate with the actual geometry upon adsorption. Technically, we perform three independent self-consistent calculations keeping all parameters equal, unit cell, number of k-points, cutoffs, etc., but the numbers of bands. One calculation for the relaxed structure of the complex, another for the clean surface and a third one for the adsorbate alone, keeping in the last two cases the previously relaxed geometry frozen. The idea is to evaluate the locally induced changes in the charge distribution due to a new chemical environment, like the presence of a metal surface.

2.3.3 Projected density of states

The decomposition of the density of states (DOS) onto specified orbitals of given atoms or molecules, namely the projected density of states (PDOS), helps to trace down the bonding in a chemisorbed system. From the experience of quantum chemistry, using very simple concepts, interaction, overlap, symmetry constraints and bonding, with the PDOS we shall try to understand the structure and reactivity of molecules on surfaces [40]. We can perform site pojected DOS or project the DOS on Molecular Orbitals (MO), and both yield complementary information.

[10]So far, we have used $n(\mathbf{r})$ to denote the electron density, nevertheless, $\rho(\mathbf{r})$ notation is also widely used alternatively.

The local density of states (LDOS) per unit energy ε is defined as,

$$\rho(\mathbf{r},\varepsilon) = \sum_{n,\mathbf{k}} |\phi_{n,\mathbf{k}}(\mathbf{r})|^2 \, \delta(\varepsilon - \varepsilon_{n,\mathbf{k}}). \tag{2.20}$$

The density of states (DOS) per unit energy,

$$\rho(\varepsilon) = \sum_{n,\mathbf{k}} \delta(\varepsilon - \varepsilon_{n,\mathbf{k}}), \tag{2.21}$$

counts energy levels with $\varepsilon = \varepsilon_{n,\mathbf{k}}$ over all states $(n,\mathbf{k})$. Its integral in energies up to the Fermi level (E_F) gives the total number of occupied states. Multiplied by two (the spin is not considered), it is the total number of electrons in the system, so the DOS curves plot the distribution of electrons in energy.

$$2 \times \left[\int_{-\infty}^{\mathrm{E}_F} \rho(\varepsilon) d\varepsilon = no.\ occ.\ states \right] = no.\ electrons. \tag{2.22}$$

The occupation of each electronic state in thermal equilibrium, is governed by the Fermi-Dirac statistics, and it is given by the Fermi distribution function,

$$f(\varepsilon, \mathrm{T}) = \frac{1}{e^{(\varepsilon-\mu)/k_{\mathrm{B}}\mathrm{T}} + 1} \tag{2.23}$$

where μ is the chemical potential. The function is plotted in Fig. 2.2 for a given μ, at T = 0 K in the left panel, and non zero temperature in the right panel. The two curves differ only in a small region of range k_BT around μ. Consequently, Eq. (2.22) is strictly true at zero temperature, otherwise $f(\varepsilon, T)$ should be included, and in order to get the total number of electrons extend the integral over all energies.

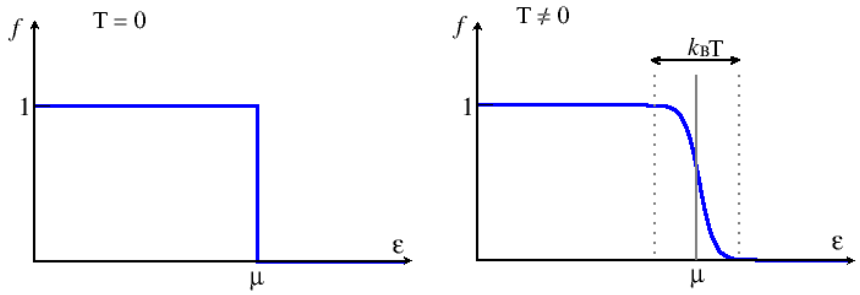

Figure 2.2: The Fermi function for a given μ at T = 0 K in the left panel, and non zero temperature in the right panel.

In an actual calculation, despite being performed at T = 0 K, for convergency reasons it is necessary to introduce some smearing, typically k_BT $\approx$ 200 meV. This is critical specially in the case of metals. Therefore, the states that are close to the Fermi energy

may have partial occupancies that must be taken into account including, the so-called occupation number, $w_{n,\mathbf{k}}$, for each $(n, \mathbf{k})$ state.

Formally, the projected density of states (PDOS) per unit energy can be defined as follows,

$$\mathrm{PDOS}_{\varphi}(\varepsilon) = \sum_{n,\mathbf{k}} \frac{1}{N_k} \left| \int \varphi^*(\mathbf{r}) \times \phi^{\mathrm{TOT}}_{n,\mathbf{k}}(\mathbf{r}) d^3r \right|^2 \delta(\varepsilon - \varepsilon_{n,\mathbf{k}}), \tag{2.24}$$

where $\phi^{\mathrm{TOT}}_{n,\mathbf{k}}$ stands for the $(n, \mathbf{k})$ wavefunction of the full system, φ corresponds to the wavefunction onto we want to project the DOS, and N_k is the number of k-points in the full Brillouin zone.

Projecting the DOS on spherical harmonics centred in one particular atom, the site projected DOS are calculated. Since they correspond to projections at the position of one particular atom, for analogy we call them PDOS on Atomic Orbitals (AOs). They give us information about the band character, s, p or d, and also the directionality of the bonds if the PDOS is decomposed in angular momentum. The PDOS on MOs are obtained when φ corresponds to an orbital from a molecule. There are two important orbitals in a molecule, which are called the frontier orbitals, the highest occupied molecular orbital (HOMO) and the lowest unoccupied molecular orbital (LUMO). Eventually, the PDOS onto these orbitals allow us to approximately estimate the amount of charge transfer between a substrate and the adsorbate by integrating the PDOS up to the Fermi energy.

When a Lorentzian type peak appears in the PDOS plot, we say that upon interaction the state has kept its atomic (PDOS on AO) or molecular (PDOS on MO) character. It means that the electrons are localised in that state due to a weak interaction with its neighbours. In general, when adsorbing a molecule on a surface, there is a broadening of the molecular states due to the interaction with the metal. The larger the broadening, the shorter the lifetime of the state. It becomes an unlocalised state that has lost its molecular character. In contrast, the smaller the broadening, the longer the lifetime, implying that the state is localised in the molecule. This simple picture turns out very useful to understand the interaction mechanism of the systems presented in this thesis.

We have developed a code to calculate the PDOS onto the molecular orbitals of the adsorbate, reading the wavefunctions of a self-consistent calculation from VASP. Because of the PAW method implemented there, we also need to take into account the augmentation charges of the ionic cores [41]. We perform two self-consistent calculations, one for the full system and another one for the molecule once the substrate is removed. All parameters but the number of bands must be kept equal in both calculations. Afterwards, we compute the projections of the wavefunctions from the full system ($\phi^{\mathrm{TOT}}_{n,\mathbf{k}}$) onto the wavefunctions of the free-molecule ($\psi^{\mathrm{MOL}}_{m,\mathbf{k}}$) to obtain the PDOS onto MO with Eq. (2.24)

as:

$$\mathrm{PDOS}_m(\varepsilon) = \sum_{n,\mathbf{k}} \frac{1}{N_k} \left| \int \psi^{\mathrm{MOL}*}_{m,\mathbf{k}}(\mathbf{r}) \times \phi^{\mathrm{TOT}}_{n,\mathbf{k}}(\mathbf{r}) d^3r \right|^2 \delta(\varepsilon - \varepsilon_{n,\mathbf{k}}), \tag{2.25}$$

where the δ function is approximated by a $\sigma \sim 0.15$-0.25 eV wide Gaussian [42].

This home-written tool to compute PDOS on MOs permits as well, to resolve PDOS in electron momentum along different directions of the surface BZ, by simply taking from Eq. (2.25) the term before summing over k-points:

$$\mathrm{PDOS}_m(\varepsilon, k) = \sum_{n} \frac{1}{N_k} \left| \int \psi^{\mathrm{MOL}*}_{m,\mathbf{k}}(\mathbf{r}) \times \phi^{\mathrm{TOT}}_{n,\mathbf{k}}(\mathbf{r}) d^3r \right|^2 \delta(\varepsilon - \varepsilon_{n,\mathbf{k}}). \tag{2.26}$$

This illustrates the dispersive behaviour of molecular bands, in a similar manner as the standard band structure plots. In fact, they are complementary as it will be showed later in Chapter 4.

2.3.4 STM simulations

The working principle of the STM is based on the quantum mechanical tunneling effect; that is, on the nonzero probability of the wavefunction of an electron to transmit through a potential barrier. The wavefunction decays exponentially across the barrier, so, when the barrier is sufficiently narrow, part of the wavefunction may be transmitted to the other side. This effect is depicted in Fig. 2.3a). For the electronic states at the Fermi

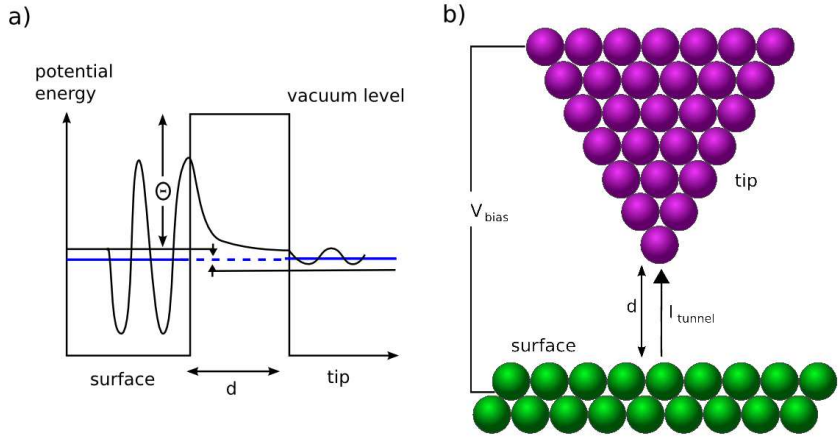

Figure 2.3: a) Tunneling across a potential barrier. b) Schema of a scanning tunneling microscope (STM).

level, the surface represents a potential barrier whose height is equal to the work function (Θ) plus the Fermi energy [43]. As illustrated in Fig. 2.3b), when a very sharp tip is

brought close enough to a conducting[11] surface, the sample, and a small bias voltage is applied between the tip and the sample, electrons can cross the vacuum gap and an electric tunneling current may be measured. Such tunneling current is used to control the tip sample distance (z) with very high sensitivity.

- STM topography

The probe tip is mounted on a piezoelectric tube which is deformed by applying electric fields. This deformation translates into lateral and vertical manipulation of the tip. In the *constant current* mode, the vertical distance of the tip at each point is adjusted via an electronic feedback loop according to the tunneling current, and a two dimensional topography is recorded. There is also another operating mode, the so-called *constant height* mode, in which the sample is scanned keeping the vertical position of the tip constant. This mode requires a perfect alignment of the tip and the sample, which is not easily achieved, and it also requires to have a flat surface to prevent the tip from touching steps or impurities.

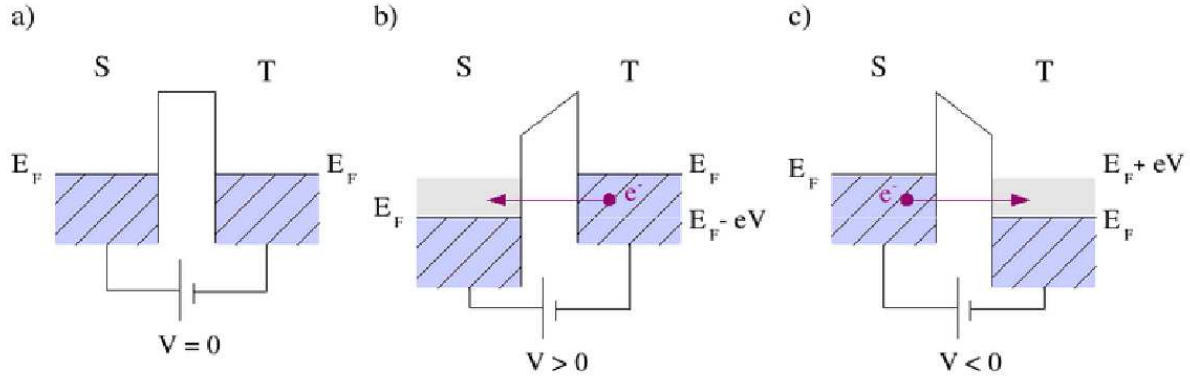

Figure 2.4: Tunneling between a sample (S) and a tip (T). a) No current for V = 0, b) Electrons tunnel from the tip to the sample for V > 0, and c) Electrons move from the sample to the tip with V < 0.

Let us assume that the sample and the probe tip have the same electronic structure, therefore when the applied voltage is zero but they are in contact, the Fermi energy (chemical potential at T = 0 K) will equal in both sides. In this situation, there will be no net current because the electrons do not have available empty states to tunnel to [Fig. 2.4a)]. On the contrary, when a voltage is applied between the sample and the tip, Fermi energies differ. If the applied voltage is positive, the electrons from the tip with energies $\in$ (E_F - eV, E_F) can flow to empty states in the sample [Fig. 2.4b)]. Finally, for

[11] As a general rule the surface must be conductor, but under some conditions STM images can also be obtained for nonconducting samples.

negative voltages, the electrons from the sample with energies between E_F - eV and E_F can occupy empty states at the tip [Fig. 2.4c)].

The energy window for the states that take part in the tunneling depends on the applied voltage, $E_F \pm eV$. However, the spatial distribution of the wavefunction is also important. When working with surfaces, it can happen that some states fall into the energy window due to a large parallel momentum,

$$E = E_z + \frac{\hbar^2 k_{\parallel}^2}{2m^*}, \tag{2.27}$$

but in the tunneling current the most important contribution comes from the states with $k_{\parallel} \sim 0$, i.e., large E_z. In general, the states that are most interesting for the tunneling are those close to the Fermi level and Γ point, states that extend outside the surface.

While a formal expression for the tunneling current is easy to write, many approximations are needed to derive an expression which permits practical computation. In the Bardeen formalism [44] the tunneling current is given by,

$$I = \frac{2\pi e}{\hbar} \sum_{\mu,\nu} \left[f(E_\mu) - f(E_\nu + eV) \right] |M_{\mu\nu}|^2 \, \delta(E_\mu - E_\nu), \tag{2.28}$$

where $f(E)$ is the Fermi function, V is the applied voltage, $M_{\mu\nu}$ is the tunneling matrix element between the states ϕ_μ of the probe and ϕ_ν of the surface, and E_μ and E_ν are the corresponding energies of such states. When the experiments are performed at room temperature or below, and at small voltages, we can cast Eq. (2.28) into Eq. (2.29),

$$I = \frac{2\pi}{\hbar} e^2 V \sum_{\mu,\nu} |M_{\mu\nu}|^2 \, \delta(E_\nu - E_F) \delta(E_\mu - E_\nu). \tag{2.29}$$

The essential problem here is to calculate $|M_{\mu\nu}|$, as it implies knowledge of the electronic structure of the tip, which is almost always unknown.

In the Tersoff-Hamann (TH) approach [45], the tip probe is assumed to be spherical, with its centre labelled $\mathbf{r}_0$, and Eq. (2.29) reduces to,

$$I \propto V \sum_{\nu} |\phi_\nu(\mathbf{r}_0)|^2 \, \delta(E_\nu - E_F) = V \rho(\mathbf{r}_0, E_F) \tag{2.30}$$

Within this approximation, the tunneling current at low bias is found to be proportional to the local density of states (LDOS) of the sample (at E_F), at the position of the tip.

For finite but low voltages, a natural extension of Eq. (2.30) is to assume that the conductance is proportional to the LDOS at an energy $\varepsilon = eV$, at the position $\mathbf{r}$. Only the states within the right energy window, that depends on the voltage, contribute to the

tunneling current. Therefore,

$$I(\mathbf{r},V) \propto \int_{\mathrm{E}_F}^{\mathrm{E}_F+eV} \rho(\mathbf{r},\varepsilon)\, d\varepsilon \qquad \text{for } V>0 \tag{2.31}$$

$$I(\mathbf{r},V) \propto \int_{\mathrm{E}_F-eV}^{\mathrm{E}_F} \rho(\mathbf{r},\varepsilon)\, d\varepsilon \qquad \text{for } V<0, \tag{2.32}$$

where $\rho(\mathbf{r},\varepsilon)$ is the LDOS per unit energy defined in Eq. (2.20), that yields,

$$I(\mathbf{r},V) \propto \sum_{\varepsilon_n>\mathrm{E}_F}^{\varepsilon_n<\mathrm{E}_F+eV} |\phi_{n,\mathbf{k}}(\mathbf{r})|^2 \qquad \text{for } V>0 \tag{2.33}$$

$$I(\mathbf{r},V) \propto \sum_{\varepsilon_n>\mathrm{E}_F-eV}^{\varepsilon_n<\mathrm{E}_F} |\phi_{n,\mathbf{k}}(\mathbf{r})|^2 \qquad \text{for } V<0 \tag{2.34}$$

Within the TH approximation, the tunneling current equals the integration of the charge densities of the states within the energy window that depends on the voltage, the so-called, partial charge densities, that can be directly obtained from the calculation. These data are then manipulated accordingly with different programs in Fortran, finally obtaining an isosurface plot on a 2-dimensional grid, that translated into a colour scale produces the simulated STM image.

- Scanning tunneling spectroscopy & conductance maps

In addition to the STM imaging, scanning tunneling spectroscopy (STS) is also a powerful experimental technique based on the tunneling microscope to obtain information on the electronic structure of the sample. STS involves measurement of the changes in the tunneling current versus bias voltage, I-V curves, or measurements of the differential conductance (dI/dV) spectrum locally. It also permits the observation of the changes with the bias voltage on a constant current topography, the so-called conductance map.

If we assume that the DOS of the tip is constant, and neglect the energy dependence of the transmission, which is sustained at low bias, the tunneling conductance is found to be directly proportional to the DOS of the sample. Therefore, STS probes the local density of states (LDOS) of the sample for an applied voltage (V),

$$\frac{dI}{dV}(\mathbf{r},V) \propto \rho(\mathbf{r},eV), \tag{2.35}$$

where the LDOS given by Eq. (2.20) is:

$$\rho(\mathbf{r},eV) = \sum_n |\psi_n(\mathbf{r})|^2\, \delta(\varepsilon_n - eV). \tag{2.36}$$

In practice, to simulate STS spectra or dI/dV maps, we only need to evaluate the LDOS. The procedure is to rewrite the KS orbitals given by Eq. (2.17), using a Fourier transform in the vertical direction (z). When one is calculating the electronic structure of a surface, it usually uses a quite thick slab, and the vertical direction in the reciprocal space is sampled only with one k-point at the origin: $\mathbf{k} = (\mathbf{k}_\parallel, 0)$. This means that the parallel component of the wavevector is sufficient to define each state, $(n, \mathbf{k}) \equiv (n, \mathbf{k}_\parallel)$. Eq. (2.17) is decomposed in vertical and parallel components,

$$\phi_{n,\mathbf{k}}(\mathbf{r}) = e^{i\mathbf{k}_\parallel \cdot \mathbf{r}_\parallel} \sum_{\mathbf{G}_\parallel} \left\{ \sum_{g_z} a_{n,\mathbf{k}}(\mathbf{g}) e^{ig_z \cdot z} \right\} e^{i\mathbf{G}_\parallel \cdot \mathbf{r}_\parallel}, \tag{2.37}$$

where $\mathbf{r} = (\mathbf{r}_\parallel, z)$, and $\mathbf{g} = (\mathbf{G}_\parallel, g_z)$. By doing a Fourier transform in the z-direction the new expansion coefficients are found and Eq. (2.37) casts into,

$$\phi_{n,\mathbf{k}_\parallel}(\mathbf{r}) = e^{i\mathbf{k}_\parallel \cdot \mathbf{r}_\parallel} \sum_{\mathbf{G}_\parallel} c_{n,\mathbf{k}_\parallel}(\mathbf{G}_\parallel, z) e^{i\mathbf{G}_\parallel \cdot \mathbf{r}_\parallel}, \tag{2.38}$$

where $c_{n,\mathbf{k}_\parallel}(\mathbf{G}_\parallel, z)$ are the complex coefficients of the wavefunction's new expansion. During VASP's calculation, those coefficients are written to a file, then this file is read with some auxiliary programs and the LDOS is evaluated as,

$$\rho(\mathbf{r}, \varepsilon) = \sum_{n,\mathbf{k}_\parallel} \left| \sum_{\mathbf{G}_\parallel} c_{n,\mathbf{k}_\parallel}(\mathbf{G}_\parallel, z) e^{i\mathbf{G}_\parallel \cdot \mathbf{r}_\parallel} \right|^2 \delta(\varepsilon - \varepsilon_{n,\mathbf{k}}). \tag{2.39}$$

The delta function is numerically approximated by a Gaussian, $\frac{1}{\sigma\sqrt{\pi}} e^{-\frac{1}{2}\left(\frac{\varepsilon - \varepsilon_{n,\mathbf{k}}}{\sigma}\right)^2}$, and the summation over k-points is then performed.

There are different type of simulations that can be done. The tunneling current can be evaluated in a fixed point ($\mathbf{r}_c$) for different bias voltages, obtaining the I-V characteristics:

$$\mathbf{r}_c \equiv (x_c, y_c, z_c) \Rightarrow I(\mathbf{r}_c, V) \; vs \; V. \tag{2.40}$$

In the same manner, instead of the tunneling current the conductance can be calculated too, and simulate a tunneling spectrum:

$$\mathbf{r}_c \equiv (x_c, y_c, z_c) \Rightarrow \frac{dI}{dV}(\mathbf{r}_c, V) \; vs \; V. \tag{2.41}$$

Alternatively, for a given voltage (V_c), one can map the whole (x, y) unit cell to obtain a

conductance map:

$$z'(x,y) : I_c \equiv I(x,y,z,V_c) \Rightarrow \frac{dI}{dV}(x,y,z'(x,y)) \; vs \; (x,y). \tag{2.42}$$

2.3.5 Bader charge analysis

We have mentioned in Sec. 2.3.3 that the PDOS allows to draw conclusions about the chemical bonding of a system. It permits to estimate the charge transfer taking place between different components too. Nevertheless, there are alternative ways for performing a charge transfer analysis, based on the knowledge of the number of electrons in an atom or molecule. One method was introduced by Mulliken in 1955 [46], using the so-called, overlap populations. However, this method is only valid for a basis set of localised atomic orbitals. The alternative method when working with plane waves is due to Bader [47, 48]. He developed a mathematical method to divide molecules into atoms, based on the electron charge density. The Bader charge analysis uses the zero flux surfaces to divide atoms. A zero flux surface is a 2D surface on which the charge density is a minimun perpendicular to the surface. We use a code developed by Henkelman *et al.* [49, 50] to perform a Bader charge analysis on a charge density grid, and the results permit to study the charge transfer processes in different systems.

Chapter 3

Chemisorption of Sulphur and Sulphur-Based Simple Molecules

3.1 Introduction

The sulphur–metal bond plays a determinant role in molecular junctions, between metal electrodes and the headgroup of different thiols [51], and in the self-assembly of monolayers (SAMs) on surfaces [10, 52, 53]. For this reason, understanding the interaction between thiolates and metal atoms at a quantitative level has recently motivated both theoretical and experimental works [54–59]. However, the adsorption states of these molecules are not fully understood yet, especially the interaction between the S headgroups and the Au substrate. It is difficult to disentangle the factors that determine the geometric and electronic structure of SAMs. Effects such as increasing coverage and the presence of defects at the surface seem to be relevant in determining important chemical processes, ranging from cleavage of the S–H bond [60–62] to S–S dimerisation [63–65] or adatom migration [66–69]. Although most of the experimental work has focused on long chain thiols, where the interaction between neighbouring chains plays an important role in the formation of the SAM, first principles theoretical studies are restricted to short chain thiols. Most of the theoretical studies have been done for small systems using density functional theory (DFT) total energy minimisation and, therefore, one must be aware of its limitations when comparing with experimental data. Furthermore, data taken at room temperature should be carefully analysed, as the energy barriers for the different processes (adatom diffusion, dimerisation or dissociation of molecules) are not always known. Being aware of all these facts, a systematic study of the S–Au bond in different systems will increase the level of understanding in problems related to the adsorption of thiols on Au surfaces.

In this chapter we present a DFT-based analysis of the S–Au bond with a progressive

increase in the complexity of the system. We start with the S–Au dimer and end with a full monolayer (ML) coverage of methylthiolates (SCH_3) on Au(111) [70, 71]. The tools that we use to characterise the S–Au bond are, besides relaxed geometries and energetics, induced electron densities and projected densities of states (PDOS) onto molecular orbitals and spherical harmonics at atomic sites [see Sec. 2.3]. We find that the essence of the S–Au interaction is already contained in the simplest system, i.e., the S–Au dimer. A comparison with other dimers, such as O–Au, S–Ag, O–Ag, S–Cu or O–Cu, leads us to conclude that relativistic effects are responsible for the unique behaviour of the S–Au bond [72–75]. We also compare the adsorption of atomic sulphur and oxygen on Au(111) at a coverage below 1 ML, to study the metal–adsorbate interface.

Next, we focus on the adsorption of sulphur-based molecules on Au(111) in the $(\sqrt{3} \times \sqrt{3})$R30° unit cell because this is the structure experimentally measured for 1 ML alkanethiol coverage on Au(111) [10, 76–79]. For S, mercapto (SH) and SCH_3 adsorption on Au(111), no essential difference in the S–Au bond is found, although the adsorption geometry depends on the end group (–H or $–CH_3$) attached to the S atom. Finally, for SH and SCH_3, we also consider interactions between different adsorbed molecules by using a c(4×2) supercell, that contains four adsorbates per unit cell.

The c(4×2) unit cell is a matter of controversy, and several models to explain this structure have been proposed. On the basis of a multiparameter analysis of grazing-incidence X-ray diffraction (GIXD) data, Fenter *et al.* [80] propose that S atoms in the c(4×2) superlattice are located on different sites, and sulphur dimers are formed with an S–S distance of 2.2 Å. They note that in the limit of short chain length thiolates, the high-density phase adopts a $(\sqrt{3}\times\sqrt{3})$R30° structure because the S–Au interaction is dominant over interchain interactions, whereas longer chain thiolates adopt the c(4×2) structure. However, recent experimental works show that short-chain systems like butanethiol, also form stable c(4×2) monolayers [81, 82]. From STM studies, it has been suggested that the double zig-zag structure seen for octanethiol on Au(111) [83–85], and the light and dark alternating rows for butanethiol, cannot be explained only with differences in twist angle, but instead, they require at least two nonequivalent adsorption sites. Theoretically, a few works [64, 65, 86] have addressed this issue using DFT. Vargas *et al.* [64] found that all trial geometries relaxed to a unique c(4 × 2) cell with dimers on bridge sites and S–S distances of 3.7 Å. Nevertheless, they emphasise the small energy difference with the pure $(\sqrt{3} \times \sqrt{3})$R30° structure, as well as the possible importance of including dispersion forces to discriminate the most stable phase. Yourdshayan *et al.* [65] also found one stable structure with two dimers with S–S distances of 2.4 Å. However, similar studies by Morikawa *et al.* [86] do not find a structure more stable than the $(\sqrt{3} \times \sqrt{3})$R30° one. Our calculations confirm this last result by studying a complete set of metastable structures. DFT calculations are probably not precise enough to distinguish

between the two mentioned structures, as energy differences per adsorbed thiol are small (below 50 meV) [64]. In this respect, it is important to recall the importance of different experimental techniques, like LEED, HREELS and STM, that help in understanding the whole adsorption process.

The chapter contains 6 other sections, apart from this introduction. A brief section for computational details followed by an initial study addressing the S and O dimers with the noble-metal atoms. Next, we present the comparison between S and O atomic adsorption on Au(111) using the p(2×2) cell. The fifth section studies S, SH, and SCH_3 $(\sqrt{3} \times \sqrt{3})$R30° structures on Au(111). The adsorption of SH and SCH_3 in a c(4×2) cell is analysed in the sixth section, and the chapter finishes with a concluding section.

3.2 Computational details

The ground-state electronic structures were calculated as explained in Chapter 2, i.e., within DFT using the VASP code, together with the PAW method to treat ion-electron interactions and the GGA (PW91) for exchange and correlation.

To account for the ground-state of dimers and isolated atoms, we performed spin polarised calculations, using the same unit cell ($10 \times 10 \times 10$ Å^3) in all cases, with a $5 \times 5 \times 5$ k-point sampling[1]. For the isolated fragments of SCH_3 and SH, being open-shell systems, spin polarised calculations were also performed, where it is interesting to note the splitting of molecular orbitals. The Au(111) surface was modelled by a periodic supercell made of seven Au atomic planes separated by an empty region of $\geq$ 10 Å along the z-direction, where the species were adsorbed only on one side of the slab. For the $(\sqrt{3} \times \sqrt{3})$R30° superstructure an hexagonal unit cell with three Au atoms per layer was used, with the full Brillouin zone sampled by a $9 \times 9 \times 1$ gamma centred k-point grid[2]. In the first stages of this work, particularly in the calculation of methylthiolate adsorption, valence electron wavefunctions were expanded in plane waves up to a kinetic energy cutoff of 500 eV, and 650 eV for the augmentations charges [70]. The reason was that we used a hard PAW pseudopotential for carbon. This calculation, in spite of being very precise, has a high computational cost. Therefore, later on, we checked that using a softer pseudopotential for the C atom and smaller energy cutoffs, 280 eV and 400 eV for electron wavefunction expansion and augmentation charges respectively, all calculations were already converged to the desired accuracy [71]. In the case of atomic sulphur and oxygen adsorption on the Au(111) surface, as mentioned before, we were interested in comparing the interaction between the adsorbate and the metal, thus we used the p(2×2) unit cell, i.e., a coverage

[1] In the case of diatomic oxygen, a previous convergency test in k-points showed that $3 \times 3 \times 3$ grid gives the required precision in energy.

[2] Monkhorst-Pack scheme with odd number of k-points is analogue to gamma centred scheme.

of 3/4 ML. In this case, the system was modelled with four Au atoms per layer, and one adsorbate per unit cell, with the full Brillouin zone sampled by a $7 \times 7 \times 1$ k-point grid. Spin polarised calculations were also performed to account for the correct binding energy of the adsorbates. The so-called c(4×2) structure, has a rectangular unit cell with 12 Au atoms per layer, and four adsorbates per unit cell. First, we did some Gamma (Γ) only calculations to study different geometries, and later we used a $5 \times 5 \times 1$ k-point grid for the full Brillouin zone. We also compared this system with $4 \times (\sqrt{3} \times \sqrt{3})$R30°, both have the same size but the latter with hexagonal lattice. Unless otherwise stated, the results that we are presenting here correspond to a valence electron wavefunction cutoff of 280 eV kinetic energy and 400 eV energy cutoff for the augmentation charges, with no dipole corrections.

Energy convergence was required to be lower than 10^{-6} eV. In the geometry optimisation process of the adsorbate–metal substrate system, the geometry of the molecule was allowed to vary along with the three outermost metallic layers[3]. Relaxation of the third layer of Au in z gives rise to negligible changes in the geometry and also in the total energy, allowing us not to include it[4]. All atoms were relaxed in the three directions until all forces were less than a maximum tolerance value. This value was 0.01 eV/Å for all the considered systems, except for the SCH_3 adsorption using hard pseudopotentials where it was 0.03 eV/Å, and for the c(4×2) supercell calculations presented in the sixth section, where it was relaxed to 0.04 eV/Å.

3.3 S– and O– dimers with Cu, Ag and Au

In this section we focus on the simplest case, the S–Au dimer, comparing it with O–Au, S–Ag, O–Ag, S–Cu and O–Cu dimers. The aim of this section is to give a first analysis of the different behaviour of the S–Au bond. While gold is particularly inert to atomic adsorption, the S–Au bond is very strong. Indeed, it is stronger than the O–Au bond despite the fact that, in general, O is more reactive than S. This last fact is evidenced in the stronger bond of O with Cu and Ag as compared to S binding. Hence, it is interesting to understand the particularities of the S–Au bond in the simplest case.

The consistency between the spin state of isolated atoms and dimers was checked. The ground-state of sulphur and oxygen is a triplet, while the ground-state of noble metals and all dimers was found to be a doublet. In Table 3.1 the equilibrium bond length, binding energy and stretch mode's vibration frequency of each dimer are listed. The binding energy is calculated following Eq. (2.18), where in this case $E_{Surf+Ads}$ corresponds to the calculated total energy of the A–B dimer, while E_{Surf} and E_{Ads} are the total energy of A

[3]For the c(4×2) supercell only the topmost layer was relaxed.
[4]Dipole corrections are negligible, and hence not included.

and B atoms, respectively. The vibrational modes were calculated by diagonalising the Hessian matrices obtained from finite differences displacing both atoms by 0.05 Å. The vibrational frequency of a bond usually helps to give an idea of the strength of that bond, although in this case it depends on the length of the bond rather than in its binding energy. Data in Table 3.1 show that, the shorter the bond the higher the vibration frequency, but this correspondence is not true for the binding energy.

Table 3.1: Calculated bonding parameters for S–Ag/Au/Cu and O–Ag/Au/Cu dimers. d_{bond} is the dimer's equilibrium bond length, E_b the binding energy and $\nu_{stretch}$ the stretch mode's vibration frequency.

Dimer	d_{bond} (Å)	E_b (eV)	$\nu_{stretch}$ (cm^{-1})
S–Ag	2.28	-2.55	328.8
S–Au	2.19	-3.01	406.5
S–Cu	2.03	-3.39	446.3
O–Ag	1.99	-2.57	486.9
O–Au	1.88	-2.91	632.3
O–Cu	1.71	-3.72	691.2

The shorter bond length of Au containing dimers as compared to Ag containing dimers suggests that scalar relativistic effects [72–75] play a role in rationalising the observed trends. As the nuclear charge increases along the periodic table of elements, the attraction of the electrons to the nucleus grows leading to a higher velocity of the electrons, which eventually comes close to the speed of light. Thus, the electron gets heavier[5] which results in a decrease of its orbit size and an increase of the ionisation energy. This relativistic contraction affects mostly to states that can interact directly with the nucleus, like the s and p orbitals that become more compact. In contrast, d and f orbitals expand due to the increased core screening created by the more compact s and p orbitals. Once scalar relativistic effects are included, the mean size of noble metal atoms, i.e., the atomic valence shell radii, become 1.73 Å, 1.83 Å and 1.62 Å for Cu, Ag and Au, respectively. Hence, in Au the valence electron charge is more localised than in Ag, or even in Cu. These relativistic effects also lead to larger ionisation energies, -6.66 eV, -6.45 eV and -7.93 eV for Cu, Ag and Au respectively. The ionisation energy is the energy required to remove one electron from the isolated atom (or molecule).

As shown in Table 3.1, we find that the equilibrium distance for dimers containing Au and Ag atoms follows the same trend. The difference in bond length between S–Ag and S–Au ($\sim$ 0.1 Å) is approximately the same as between O–Ag and O–Au. This means

[5]The mass of the 1s electron of gold is 20% higher as compared to that of hydrogen.

that the difference in bond length is essentially given by the different extension of Ag's and Au's s and d orbitals that participate in the S–Ag and S–Au bond. The case of Cu is different, because it is much more reactive, leading to shorter bonds, no matter what the extension of the other atom's (S or O) orbitals is. However, S is more strongly bound than O only in the Au case. This is a relativistic effect due to the contraction of the 6s shell and the concomitant expansion of the 5d shell [87]. The 6s and 5d electrons of Au have just the extension that leads to a stronger bond with the more extended 3p of S, as compared to the 2p of O.

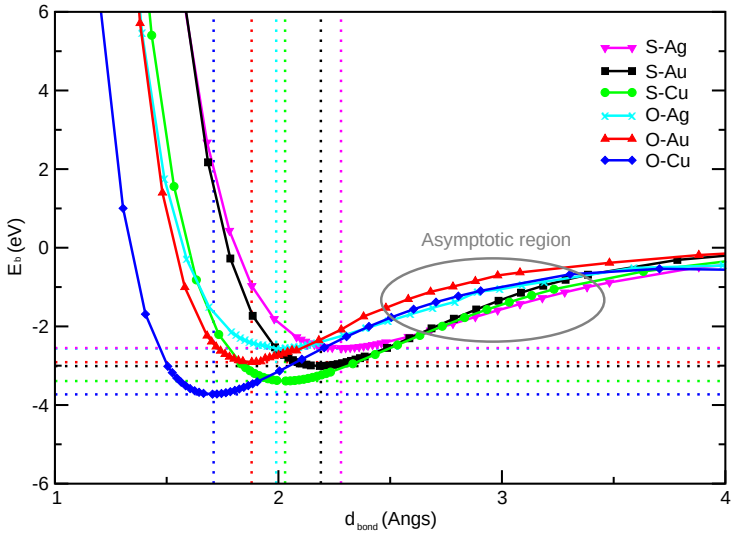

Figure 3.1: Binding energy *vs* dimer's bond length.

We can plot the binding energy of each dimer against the distance between the two atoms, namely, the interaction curve, as done in Fig. 3.1. In the asymptotic region of those curves, far from the metal atoms, the behaviour of the interaction curve is governed by the electron affinity of sulphur and oxygen[6]. In this region, it is the polarisation of the atomic cloud the leading mechanism for the interaction between atoms. The electron affinity is the energy released in an electron capture by the isolated atom, $E(N+1) - E(N)$. It yields information on the stability of the negative ion species and hence on the capability of the atom to capture electrons. As the two atoms approach each other, the extension of the charge clouds enter into play. Given the lack of long-range interactions in the present DFT calculations, the results in the region beyond 3 Å can only be taken qualitatively.

In order to have a better understanding of the character of the bond, next we explore the induced electron densities of the different dimers. Comparison of the relative value of electronegativities is a simple criteria to estimate the degree of ionicity of a bond, although not its strength. The electronegativity is a measure of the ability of an atom or molecule to attract electrons in the context of a chemical bond. The type of bond formed is largely

[6]Gold's electron affinity (eV) is 2.31, silver's is 1.30, copper's 1.23, sulphur's 2.07 and 1.46 for oxygen.

determined by the difference in electronegativity between the atoms involved. Atoms with similar electronegativities will share an electron with each other and form a covalent bond. However, if the difference is very large, the electron transfer between atoms leads to an ionic bond. Therefore, based on a simple comparative analysis of electronegativities[7] the S–Au dimer is expected to have a large covalent character, whereas the other dimers should be more ionic. This is confirmed by a Bader charge analysis [see Sec. 2.3.5]. It shows that the charge transfer for the S–Au dimer is negligible, whilst the rest present charge transfers from 0.35 e^- in the case of S–Cu, to 0.55 e^- transfer in the case of O–Au. In addition, this can be also seen in Fig. 3.2, where contour plots of the induced electron

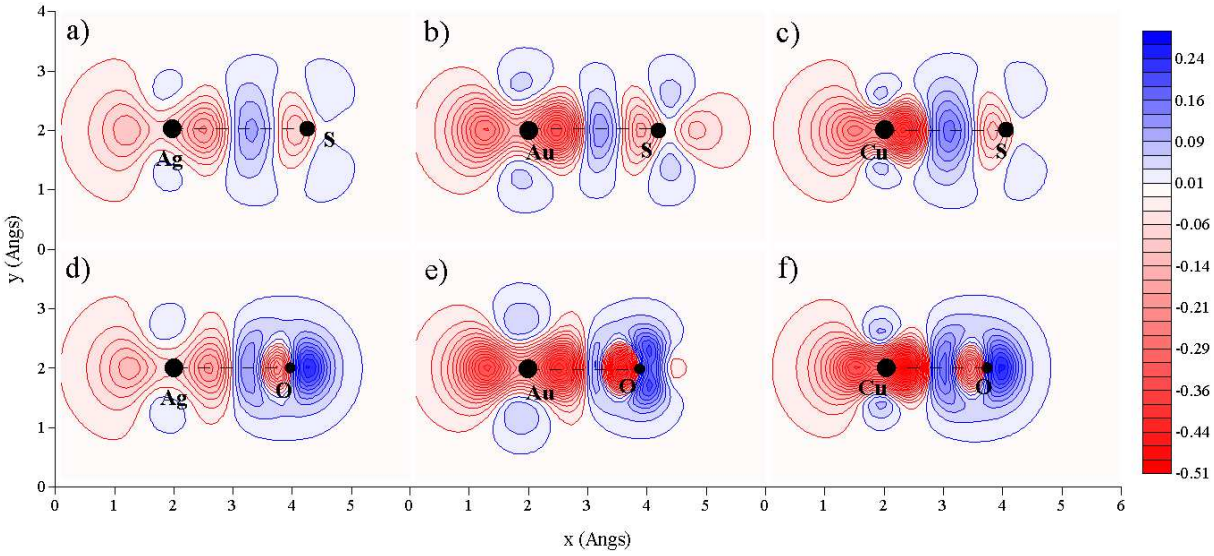

Figure 3.2: Contour maps of the induced electron density for S– and O– dimers with Cu, Ag and Au noble metals plotted in the plane containing the atoms. Positive and negative electron density differences ($e^-/\text{Å}^3$) are represented by blue and red colour respectively, and the corresponding colour scale is shown.

density, $\rho_{\text{ind}} = \rho(\text{A-B}) - \rho(\text{A}) - \rho(\text{B})$, for different A–B dimers are shown. Sulphur has a quite complex induced electron density distribution capturing charge in a 3p-like orbital, while oxygen has a very compact distribution in agreement with its 2p configuration. Dimers formed with sulphur [see Fig. 3.2a), 3.2b) & 3.2c)], present a charge accumulation approximately halfway along the bond, typical of covalent bonds. In the case of oxygen, the positive induced electron density, i.e., electron excess, is sourrounding the O atom [see Fig. 3.2d), 3.2e) & 3.2f)], hence we retrieve the ionic character of the O–noble metal interaction in the corresponding induced electron density. Ag and Cu containing dimers show the same qualitative behaviour both with O and S, although the rearrangement of charge is larger for Cu containing clusters, in agreement with a stronger binding.

[7] Gold's electronegativity (Pauling Scale) is 2.54, silver's is 1.93, copper's 1.90, sulphur's 2.58 and 3.44 for oxygen [88, 89].

3.4 S/Au(111) and O/Au(111): p(2×2) unit cell

We have seen in the previous section that the stronger interaction of Au atoms with S as compared to the interaction with O is explained by the relativistic contraction of Au. Let us now increase the complexity of the system and compare the adsorption of sulphur and oxygen on the Au(111) surface.

In order to focus on the metal–adsorbate interaction and reduce the adsorbate–adsorbate interaction, a coverage below 1 ML was studied. We adsorbed sulphur and oxygen atoms on the hcp, fcc, top and bridge sites to find the actual adsorption site on Au(111). Fig. 3.3 depicts schematically the sites considered. Upon relaxation of the adsorbate and the three

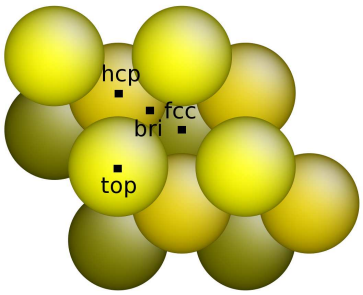

Figure 3.3: Schematic picture of the different adsorption sites on the Au(111) substrate.

outer layers of gold, we find that for both adsorbates the most stable adsorption site is the fcc hollow, in agreement with previous works [90–92]. The hcp site is about 0.2 eV less stable, and the top site is 1.5 eV less stable than the fcc site. During relaxation of sulphur and oxygen on the bridge site, they moved away to the fcc hollow, showing that at best, the bridge site is a saddle point for the adsorption of these atomic species. The bridge site turn out to be important when studying the adsorption geometry of short chain alkanethiolates, as we will show later in Sec. 3.5.1.

Table 3.2: Structural parameters and binding energy of S/Au(111) and O/Au(111) on the fcc site. d_{X-Surf} is the vertical distance from the X atom (either S or O) to the Au surface, d_{X-Au} the distance from the X atom to its nearest Au atoms, δ_{Autop} vertical displacement of the Au atom from the topmost layer which is not bound to the adsorbate, $\delta_{Au2^{nd}}$ vertical displacement of the Au atom from the second layer underneath the hcp site and E_b the binding energy. All distance parameters are in Å.

System	d_{X-Surf}	d_{X-Au}	δ_{Autop}	$\delta_{Au2^{nd}}$	E_b (eV/at.)
S/Au(111)	1.59	2.39	-0.29	0.18	-3.60
O/Au(111)	1.12	2.13	-0.28	0.13	-3.35

Structural parameters and binding energies for the fcc adsorption geometry of S and O are summarised in Table 3.2. It should be noted that O is adsorbed closer to the Au

surface than S, but the latter has a larger binding energy, i.e., S interacts more strongly with the metal. This is in accord to what we had found for the dimers [see Sec. 3.3].

Finally, Fig. 3.4 shows contour maps of the induced electron density for S/Au(111) and O/Au(111) complexes in the p(2 × 2) cell, which allows us to compare the nature of sulphur–gold and oxygen–gold interactions on the surface. Again, we see comparing Fig. 3.4a) and 3.4b), that sulphur, being larger, has a quite complex induced electron density distribution capturing charge in a 3p-like orbital, while oxygen has a very compact distribution in agreement with its 2p configuration. This was also the case for the S–Au and O–Au dimers. In the case of oxygen, the positive induced electron density, i.e., charge accumulation, is surrounding the O atom with the largest accumulation region located on top of it and a depletion region underneath, as shown in Fig. 3.4d). This positive and negative charge distribution agrees with the ionic character of the O–Au interaction. In contrast, the largest positive induced electron density for S/Au(111) is located halfway along the S–Au bond [see Fig. 3.4c)], fingerprint of the covalent character of the bond [91].

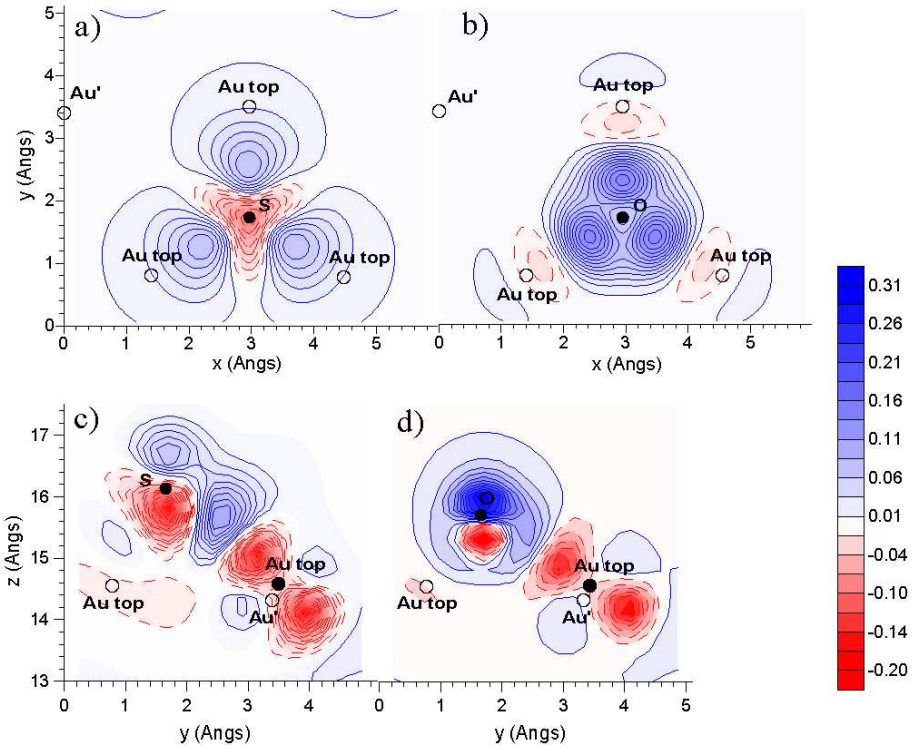

Figure 3.4: Contour maps of the induced electron density (ρ_{ind}) for S/Au(111) and O/Au(111) at the fcc sites. a) and b) are the top views of the ρ_{ind} plotted in the plane of each adsorbate. c) and d) side view contour maps in a vertical plane containing one S–Au bond and one O–Au bond respectively. Positive and negative electron density differences ($e^-/\text{Å}^3$) are represented in blue and red colours, respectively, and the corresponding colour scale is shown. Filled circles state for atoms contained in the plotted plane, and empty ones for atoms out of plane.

3.5 S-based molecules on Au(111): $(\sqrt{3} \times \sqrt{3})$R30° unit cell

Now, we study the adsorption of thiols on Au(111) in the $(\sqrt{3}\times\sqrt{3})$R30° unit cell because it is the structure experimentally measured for 1 ML alkanethiol coverage on Au(111) [10, 76–79]. In the last section of this chapter, we will address a larger superstructure, the c(4 × 2) unit cell. We first focus on the most stable adsorption geometry of mercapto (SH) and methylthiolate (SCH_3). Afterwards, we end the section by comparing S, SH and SCH_3, where we will only refer to the adsorption of different species in the fcc site, as it is found to be the most favourable S atomic adsorption site on Au(111) [90, 91].

3.5.1 SH/Au(111) and SCH_3/Au(111)

Different high symmetry adsorption sites were studied, such as the fcc-hollow, hcp and bridge sites [see Fig. 3.3]. In the case of mercapto molecules, starting the molecular relaxations with the S atom over the bridge site, the same final configuration was found, no matter which initial tilt angle the molecule has. This final molecule – substrate conformation was reproduced even with the molecule adsorbed on the fcc site with a nonzero tilt angle (30°). This final configuration, the most stable one, consists in the sulphur atom nearly located on the bridge site and the S–H bond tilted around 74° with respect to the surface normal. However, when starting from the fcc vertical configuration the molecule stayed upright without moving from the fcc hollow site, because it is a metastable configuration. Fig. 3.5 shows a picture of the two final (meta)stable geometries for mercapto on Au(111).

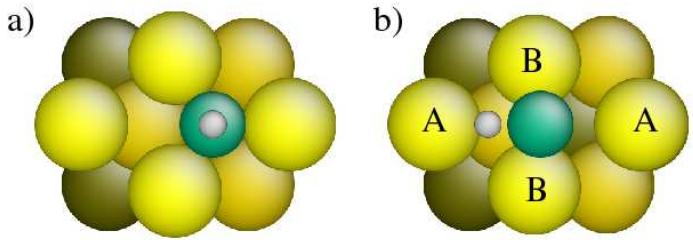

Figure 3.5: a) Top view of SH adsorbed in the fcc vertical configuration. b) Top view of the bridge tilted adsorption geometry.

The most stable adsorption geometry of methylthiolate molecules on Au(111) is in good agreement with most of recent calculations [54, 57, 65, 93–95]. Nonetheless, our results are at odds with several proposals of ontop adsorption sites [66–68] through some surface reconstructions. After checking that the tilting of the molecule favoured the adsorption, and that the fcc-hollow site was slightly more stable than the hcp site; the SCH_3 molecule was adsorbed both, in fcc and bridge positions, with a tilt angle of 30° and

a staggered orientation [65] for hydrogen atoms. Then, full relaxation of the geometries were performed. We find that the most stable binding site lies between the bridge and fcc sites with an S–C tilt angle of about 54° with respect to the surface normal. In this configuration, the molecule is tilted towards the hcp site. Hereafter, this configuration will be referred as the bridge-fcc one. In analogy with mercapto molecules, the methylthiolate molecule shows a preference for an upright geometry on the hollow site. On the bridge site, the molecule tends to tilt. Fig. 3.6 shows a schematic picture of the fcc vertical and bridge-fcc configurations.

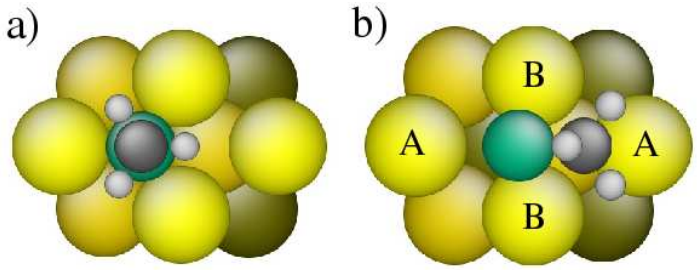

Figure 3.6: a) Top view of SCH_3 adsorbed in the fcc vertical configuration (staggered orientation). b) Top view of the bridge-fcc adsorption geometry.

Gottschalck and Hammer [90] have investigated mercapto's as well as methylthiolate's adsorption on Au(111). In opposition to our present study, they used a p(2×2) cell corresponding to a 3/4 ML coverage. The site preference remains unchanged with coverage, but the tilt angle differs as compared to the $(\sqrt{3} \times \sqrt{3})$R30° cell [94]. In Table 3.3, our calculated structural parameters and binding energy for both, mercapto and methylthiolate molecules are listed[8]. The calculated binding energy for SCH_3 is in good agreement

Table 3.3: Structural parameters for the bridge/bridge-fcc and fcc vertical adsorption geometries of SH/Au(111) and SCH_3/Au(111). Δd_{bri} is the lateral distance of S to the actual bridge position, Δd_{fcc} the lateral distance to the fcc site, and θ the tilt angle between the molecular backbone and the surface normal. d_{S-Surf} is the vertical distance from S to the Au surface, d_{S-Au} the distance from the S atom to its nearest Au atom, d_{S-X} is the S–C or S–H bond length and E_b the binding energy. All distances are in Å.

System	Δd_{bri}	Δd_{fcc}	θ(°)	d_{S-Surf}	d_{S-Au}	d_{S-X}	E_b (eV)
SH/Au(111)							
bridge	0.03	0.82	74	1.94	2.49	1.36	-2.04
fcc vert	-	0	0	1.71	2.54	1.38	-1.58
SCH_3/Au(111)							
bridge-fcc	0.23	0.62	54	1.91	2.49	1.84	-1.81
fcc vert	-	0	0	1.70	2.53	1.84	-1.52

[8]The structural parameters obtained using hard pseudopotentials [see Sec. 3.2 for details] are very similar, thus, they are not included here.

with the experimental value of -1.73 eV [96]. The bridge-fcc configuration is about 0.3 eV more stable than the fcc-vertical one for methylthiolate molecules. For mercapto molecules, this energy difference between bridge and fcc configurations goes up to 0.5 eV, slightly larger than in the previous system. Mercapto's behaviour turns out to be very similar to methylthiolate's one. Despite having distinct binding position for the S atom and different tilt angles, the S–Au bond length is the same in both cases and the binding energies are of the same order of magnitude [see data in Table 3.3].

To evaluate the binding energy, we used as reference the energy of the isolated fragment of SH/SCH_3 including spin polarisation. However, it is interesting to point out that, regarding the chemisorption process, the binding energy or adsorption energy of a molecule on a given substrate can be defined in different ways. One can assume for instance, that in such SAMs, thiols undergo an S–H bond cleavage, and bind to gold via the sulphur head. The hydrogen then, can also bind to the surface or evaporate as molecular hydrogen (H_2). Experimentally in some cases, clean Au(111) surfaces are exposed to gaseous dimethyl disulphide (CH_3S–SCH_3), which dissociates spontaneously into methylthiolates on Au. In particular for methylthiolate, and according to these different chemical reactions paths, using different energy references for the adsorbate, different binding energies from Eq. 2.18 can be calculated as follows:

1. $E_{Ads} = \mathrm{E}(SCH_3)$
2. $E_{Ads} = \frac{1}{2}\,\mathrm{E}_{Dmds}$, *Dmds* refers to $(SCH_3)_2$ molecule.
3. $E_{Ads} = \mathrm{E}(SCH_3^-)$
4. $E_{Ads} = \mathrm{E}(HSCH_3) - \frac{1}{2}\,\mathrm{E}(H_2)$
5. $E_{Ads} = \mathrm{E}(HSCH_3) - \mathrm{E}(H/Au) + \mathrm{E}(Au)$

In Table 3.4 we have summarised the different binding energies found in the literature for SCH_3 [7th column], depending on the different reaction path [4th column] that has been considered in each reference [2nd column]. We have also included our own results, both using the hard pseudopotentials and the softer ones. For comparison, we include as well some structural parameters, such as the S–substrate vertical distance [5th column] and the tilt angle with respect to the surface normal [6th column]. In general, we observe that the largest binding energies are obtained when the methylthiolate radical is taken as energy reference for the adsorbate [labelled with 1 in 4th column of Table 3.4]. It is interesting to note that using dimethyl disulphide [labelled with 2 in 4th column of Table 3.4], the binding energy in the bridge-fcc configuration is $\sim$ -0.30 eV. The same chemisorption path in the case of fcc site yields a binding energy of $\sim$ -0.02 eV, and

Table 3.4: Methylthiolate's binding energies from different references. XC states for the parametrisation used for the exchange and correlation, E_{Ads} represents the chemisorption path considered, d_{S-Surf} is the vertical distance from S to the metal surface, and θ the tilting angle.

Site	Reference	XC	E_{Ads}	d_{S-Surf} (Å)	θ(°)	E_b (eV/mlc.)
bridge-fcc	[86, 93]	PBE	2	2.05	52.7	-0.27
	[54]	BLYP	-	2.09	46.97	-1.84
	[65]	PBE	1	2.03	43.2	-1.73
	[94]	PW91	-	-	56	-1.62
	[90][a]	PW91	1	2.07	61.1	-1.72
			2			-0.20
			4			-0.03
			5			+0.12
	[70][b]	PW91	1	1.89	50	-1.76
			2			-0.29
			3			+0.04
			4			-0.12
			5			+0.06
	[71]	PW91	1	1.91	54	-1.81
			2			-0.31
fcc	[86, 93]	PBE	2	1.78	16.7	-0.03
	[54]	BLYP	-	1.97	0.11	-1.77
	[64]	PW91	-	1.81	-	-0.13
	[65]	PBE	1	1.92	34.4	-1.49
	[94]	PW91	-	-	0	-1.31
	[97]	-	1	-	0	-2.39
			5	-	0	-0.69
	[90][a]	PW91	1	2.04	55.7	-1.49
	[70][b]	PW91	1	1.72	0	-1.48
			2			-0.03
			3			+0.31
			4			+0.16
			5			+0.34
	[71]	PW91	1	1.70	0	-1.52
			2			-0.02
hcp	[64]	PW91	-	1.90	-	+0.05
	[90][a]	PW91	1	2.06	56.9	-1.47
	[94]	PW91	-	-	0	-1.29
	[70][b]	PW91	1	1.80	0	-1.39
			2			+0.07
			3			+0.41
			4			+0.25
			5			+0.43

[a] Coverage (Θ) of 0.75

[b] Hard pseudopotentials

it becomes positive ($\sim$ +0.10 eV) for hcp adsorption. This shows that the S–Au bond strength is comparable to the S=S one. According to DFT calculations, the rest of reaction cases are not energetically favourable. Nevertheless, this does not mean that they do not occur in actual experiments.

In addition, the induced electron density provides interesting information about the nature of the bonding between the sulphur head and the substrate. In the upper and lower panels of Fig. 3.7, we plot the contour maps of the induced electron density for the mercapto's and methylthiolate's most stable configuration, respectively. Both molecules show essentially the same effects. Hence, they seem to have the same bonding mechanism. This suggests that the sulphur–metal bonding character is independent of the type of radical, $-CH_3$ or –H. In Fig. 3.7a) and 3.7c) it can be seen an accumulation of charge in

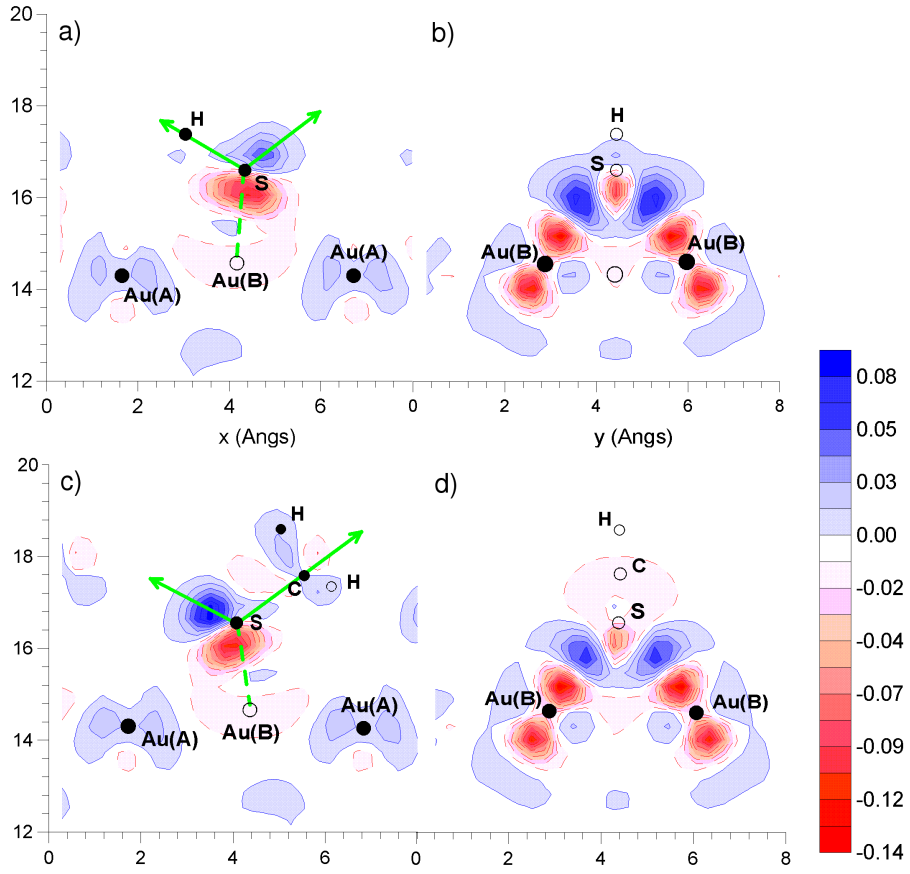

Figure 3.7: Contour maps of the adsorption induced electron density (ρ_{ind}). a) Induced electron density for SH on the bridge site, plotted in a vertical plane containing the S–H bond and Au(A) atoms [see Fig. 3.5]. b) ρ_{ind} in a vertical plane containing the two Au(B) atoms with which the sulphur atom is coordinated. c) & d) ρ_{ind} for methylthiolate adsorbed on the bridge-fcc configuration, the plots correspond to a vertical plane containing the S–C bond and the Au(B) atoms, respectively. Positive and negative electron density differences ($e^-/\text{Å}^3$) are represented by blue and red colour respectively, and the corresponding colour scale is shown. Filled circles state for atoms contained in the plotted plane, and empty circles represent atoms out of the plane. Green arrows mark S–H/C, S–Au(B), and S–(lone pair) bond directions.

a region over the S atom, that corresponds to a lone pair electron; while in Fig. 3.7b) and 3.7d) there is an accumulation in a region more or less halfway between S and Au(B) atoms [see definition of Au(B) in Fig. 3.5b) or Fig. 3.6b)], showing the covalent character of the S–Au(B) bond [98]. In contrast, it will be shown later [see Fig. 3.14] that the induced electron density plots for the fcc vertical configuration of both molecules, SH and SCH_3, present no evidence of the existence of a lone pair, but only the electron excess halfway the S–Au bond, similar to the one depicted in Fig. 3.7b) and 3.7d), respectively.

The SCH_3 molecule adsorption site is found to be between the fcc-hollow site and the bridge site. This position refers to the vertical projection of the S atomic position. However, the adsorption geometry illustrated in Fig. 3.6b) is easier to visualise by imaging that the whole thiolate uses as pivots two S–Au(B) bonds leaving a lone pair pointing upwards, as shown in Fig. 3.7c). In this way the S–C and S–Au bonds form an angle of about 111° that resembles the optimal 109.5° of the sp^3 orbitals. Furthermore, the lone pair saturated orbital extends in a direction forming an angle of approximately 110° with respect to the S–C bond [Green arrows in Fig. 3.7c)]. Starting from the fcc-hollow site's configuration, we have seen that as the sulphur atom moves towards the bridge site, the S–Au(B) bond strengthens, while the S–C bond length does not change appreciably. The whole picture suggests a stabilisation of the adsorption geometry due to steric effects [94]. Fig. 3.8 tries to illustrate this stabilisation going from the threefold symmetry fcc-hollow site to a twofold bridge-fcc configuration with a saturated lone pair pointing upwards, resembling the sp^3 hybridisation [70].

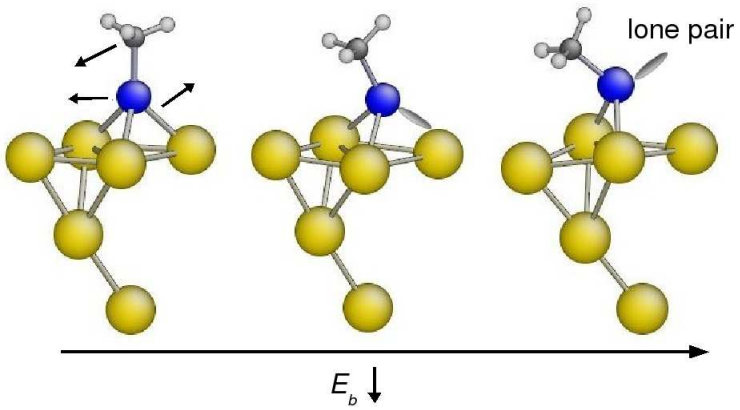

Figure 3.8: Sequence representing the stabilisation of the geometry of the methylthiolate adsorbed on Au, going from the threefold symmetry fcc-hollow site to a twofold bridge-fcc site with a saturated lone pair pointing upwards.

In the case of mercapto, the sulphur atom lies almost on the bridge site and the S–H bond is more tilted than in the case of methylthiolate's adsorption, where the sulphur atom is located between the fcc and bridge sites. These differences are due to a larger repulsion between the substrate and the methyl group as compared to the hydrogen–

substrate repulsion in the mercapto's case. This repulsion leads the molecule to decrease its tilt angle and to move away from the bridge site in order to recover an sp^3 configuration with bond angles close to 109.5°.

It has been already mentioned in the first chapter of this thesis [Sec. 2.3.3], that Projected Density of States (PDOS) on spherical harmonics at the atomic sites (PDOS on AO) or molecular orbitals (PDOS on MO) help to trace down the bonding in a chemisorbed system [40]. Both types of PDOS provide complementary information. The results obtained when projecting the DOS on sulphur's and carbon's (in the case of SCH_3) atomic sites are presented first. This analysis allows us to shed light on the fact that bridge (for SH) or bridge-fcc (for SCH_3) configurations are more stable than the fcc vertical configuration. Next, the PDOS onto mercapto's and methylthiolate's frontier orbitals, the highest occupied molecular orbital (HOMO) and the lowest unoccupied molecular orbitals (LUMO), permit us to compare the adsorption mechanism of both molecules, where the adsorbate–metal bonding is determined by the S–Au interaction.

- PDOS on AO: Bridge *vs* Fcc

The methylthiolate molecule has molecular orbitals that are formed from the hybridisation of different atomic orbitals of its components, mainly C and S [see Fig. 3.11]. However, it can be seen in Fig. 3.9c) and 3.9d) that there is a state located right at the Fermi energy that keeps its atomic character after the formation of the molecule. This state corresponds to a partially occupied sulphur state, and we found that upon adsorption on Au, it is the state that contributes most to the bonding [black arrow in Fig. 3.9]. Fig. 3.9c) shows how it shifts below the Fermi level, becoming occupied, and spreads losing its atomic character. This sulphur state interacts strongly with the orbitals of Au(B) atoms that have a vertical component; and due to its chemisorbed geometry, specially with d_{yz} as shown in Fig. 3.9b). A rearrangement of charge around the Fermi level involving the p_z orbitals of Au(B) can be also observed [see box in Fig. 3.9a) and Fig. 3.9e)]. We find a similar mechanism to form the bond at the fcc-hollow site. The state that contributes most is again the sulphur state at the Fermi level, but in this case, as it is spatially distributed in a horizontal plane, it does not have component in p_z [see Fig. 3.9g)]. Its interaction with Au orbitals is less effective than in the bridge-fcc configuration. In Fig. 3.9e) and Fig. 3.9f) the small peak near the Fermi level, marked with the arrow for the bridge-fcc case, is now missing. Thus, it is important to note that the different chemical environment due to the adsorption geometry leads to a different electronic structure.

In the case of mercapto, the PDOS on AO at sulphur's and gold's sites, for the bridge and fcc adsorption configurations, shown in Fig. 3.10, present essentially the same features as the PDOS for methylthiolate. There is a charge rearrangement around the Fermi energy

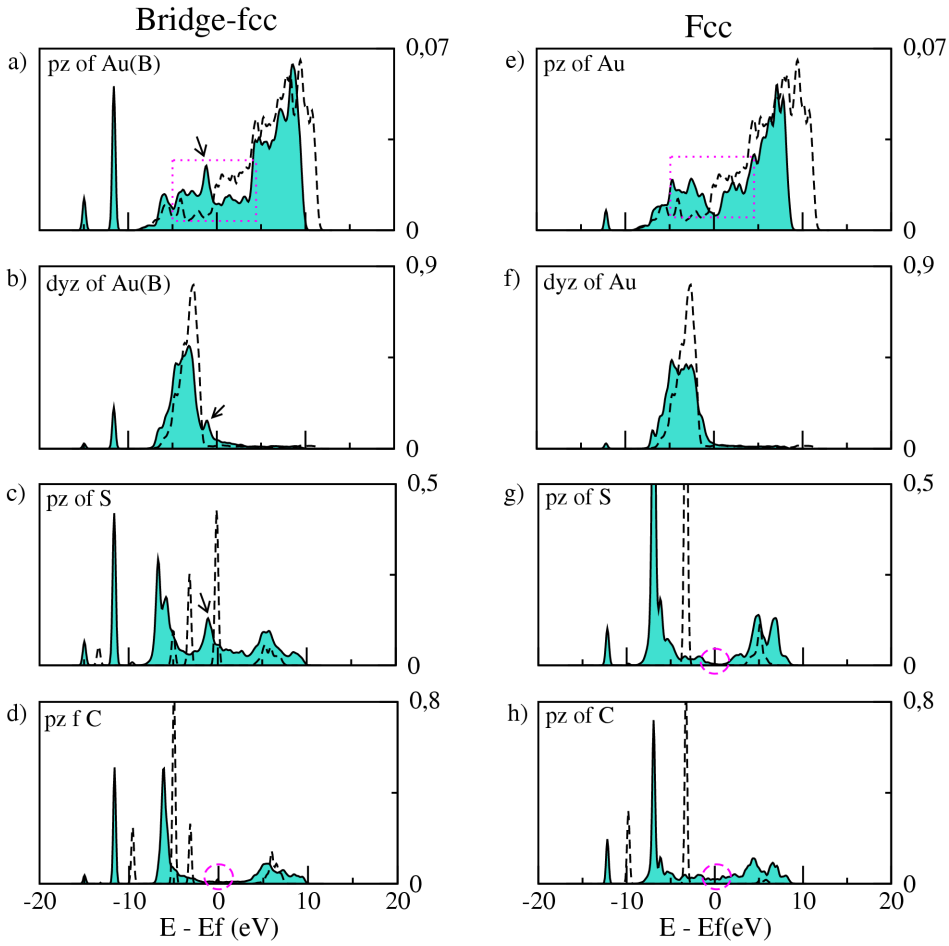

Figure 3.9: SCH_3/Au(111): Green areas, a) PDOS onto pz for Au(B) in the bridge-fcc geometry, b) onto dyz, c) PDOS onto pz for S, d) onto pz for C, e) PDOS onto pz for Au in the fcc vertical configuration, f) onto dyz, g) onto pz for S, and h) onto pz for C. Dashed lines in a), b), e) & f) correspond to PDOS for Au in the clean gold slab, and in c), g) and d), h) correspond to PDOS on S and C in isolated SCH_3 molecule, respectively.

[see Fig. 3.10a) and 3.10d)], and a strong interaction of the sulphur orbital located at the Fermi level [black arrow in Fig 3.10] with gold. This state, like in the case of SCH_3, does not have p_z component in the fcc vertical configuration [see Fig. 3.10f)]. We can also see that the interaction of this sulphur state with the metal substrate is less effective for the fcc adsorption configuration. The peak feature close to Fermi energy is missing in Fig. 3.10d) and Fig. 3.10e). This explains why the bridge tilted configuration is more stable than the fcc vertical one.

- PDOS on MO: SH *vs* SCH_3

It turns out that the frontier orbitals dominate the interaction between molecules and also between molecules and surfaces. These are the valence orbitals, the orbitals most easily perturbed in any interaction, thus in them resides the control of the chemistry of

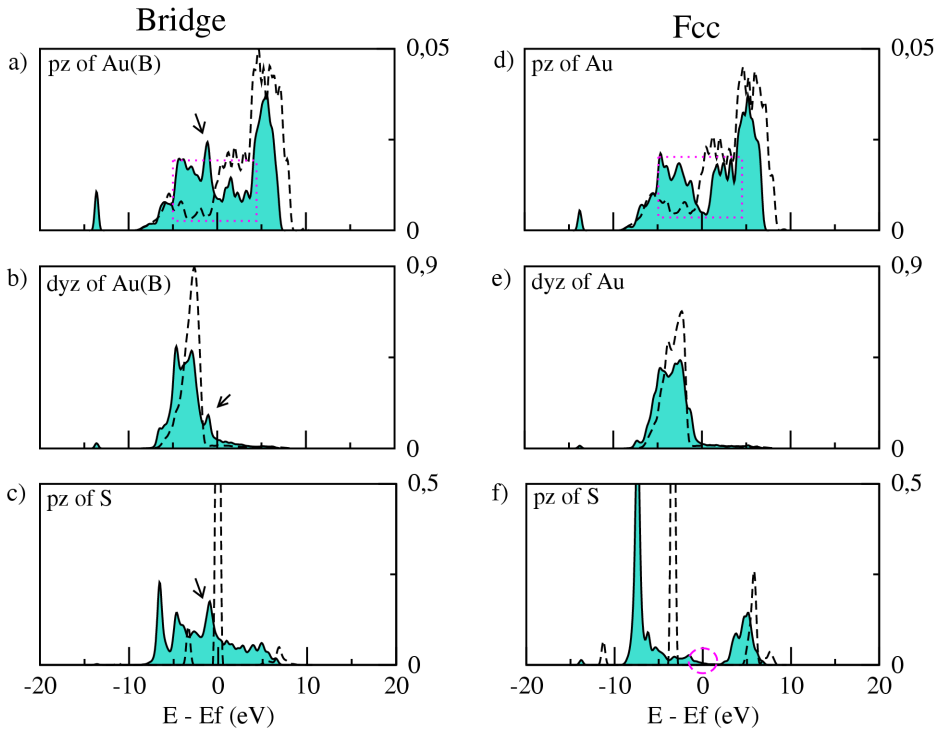

Figure 3.10: SH/Au(111): Green areas, a) PDOS onto pz for Au(B) in the bridge tilted geometry, b) onto dyz, c) PDOS onto pz for S, d) PDOS onto pz for Au in the fcc vertical configuration, e) onto dyz, and, f) onto pz for S. Dashed lines in a), b), d) & e) correspond to PDOS for Au in the clean gold slab, and in c), and f) PDOS for S in isolated SH.

the molecule. In Fig. 3.11, the HOMO and LUMO of the molecular radical including spin polarisation are shown. Spin up and spin down states are depicted in cyan and magenta shaded colours respectively. Note that only one of the degenerated HOMO[9] is plotted for each molecule, and that for the LUMO the spin polarisation is negligible [see also Fig. 3.12]. Despite the different nature of the radical attached to the sulphur atom, the HOMO and LUMO around the S atom are very similar in both molecules, SCH_3 and SH.

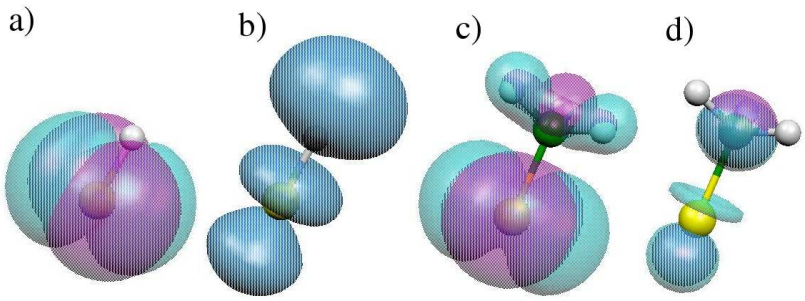

Figure 3.11: A contour of electron densities is plotted for the SH's HOMO a) and LUMO b), and for the SCH_3's HOMO c) and LUMO d). Spin up and spin down states are depicted in cyan and magenta shaded colours respectively

[9]Calculations results in two degenerated HOMOs for mercapto and methylthiolate.

Therefore, and taking into account that these are the dominant states in the molecule–surface interaction description [40], we conclude that the bonding mechanism for both molecules is essentially the same and is determined by the S–Au interaction.

In Fig. 3.12, the PDOS onto these frontier orbitals for mercapto and methylthiolate molecules in their most stable adsorption configuration are shown. Qualitatively, the great similarities between both systems are evident. At the Fermi energy the most active states are the HOMOs (π^*). This HOMO orbital is mainly located around the sulphur atom. Hence, it is directly related to the sulphur's atomic orbital described before. In Fig. 3.12a) & 3.12c) it is shown that upon adsorption, the HOMOs interact strongly with the d-band of Au, which is located between -8.0 eV and -2.0 eV below the Fermi energy. The PDOS onto HOMOs shift to lower energies and spread notoriously. The HOMO-1 (σ^*) of the molecules (not shown) also interacts with the Au d-band, but it keeps more its molecular character. The rest of the states located lower in energy, do not interact

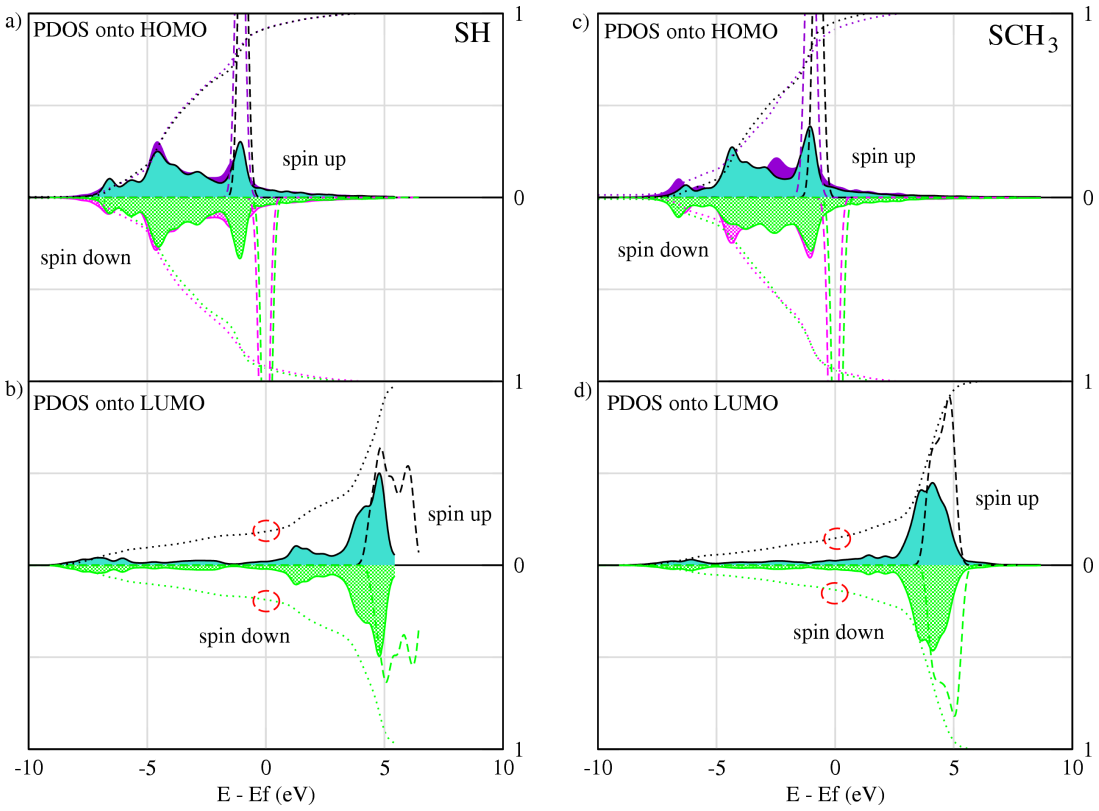

Figure 3.12: Coloured areas: a) PDOS onto the SH's degenerated HOMOs and b) onto the LUMO, for the bridge adsorption configuration. c) PDOS onto the degenerated HOMOs of SCH_3, and d) onto the LUMO, for the bridge-fcc adsorption configuration. Dashed lines: a) and b), PDOS for the SH molecule in the $(\sqrt{3} \times \sqrt{3})$R30° conformation without the metallic substrate, and c) and d) PDOS without substrate for the corresponding SCH_3 array. Dotted lines: the integration over energy of each PDOS curve, and the red circles in b) and d) show the value of this integral at the Fermi energy, i.e., the estimated charge transfer to the LUMOs.

effectively with gold states. The corresponding PDOS (not shown) present peaks that are shifted upon adsorption, but keeping their molecular character. There are two orbitals partially occupied (spin down states) and two other already occupied in the radicals (spin up states) [see dashed lines in Fig. 3.12a) & 3.12c)]. These open-shell systems tend to capture a full electron to close their singly occupied molecular orbital (SOMO). This fact is revealed by integrating the PDOS onto MOs up to the Fermi energy, which allows us to approximately estimate the amount of charge transfer. The net charge transfer from Au to the molecules' HOMOs is calculated to be about 1 e^-. Indeed, projection onto the radicals' SOMO leads to basically occupied electronic states, showing that both molecules on the surface behave as close-shell systems with some charge transfer into their LUMOs, as well. The LUMO of both molecules also interacts with the d-band of gold. It can be seen in Fig. 3.12b) & 3.12d) that there is a significant contribution below the Fermi level, which means that the LUMO gets partially occupied (~ 0.4 e^- charge transfer).

The dashed lines in Fig. 3.12 correspond to PDOS onto the molecular orbitals themselves for the molecules. On isolated molecules, this PDOS should be a delta function. However, we notice a certain structure in Fig. 3.12b) & 3.12d). Our method to obtain PDOS onto MOs requires the same unit cell for the adsorbate–surface complex and for the free adsorbate. The deviation from a peak manifests a residual interaction with neighbouring molecules, that increases for unoccupied states because the corresponding orbitals are more extended. Therefore, the corresponding LUMO band width results about 1 eV. Indeed, the PDOS yields the broadened structure of a weakly dispersing band [see Eq. (2.25)] due to the periodic molecular array.

So far, we have used different theoretical tools to rationalise the adsorption mechanism for SH and SCH_3. However, it is always interesting to contrast the results with experimental measurements. With this in mind, we did a theoretical analysis of the vibrational modes of the methylthiolate adsorbed on Au(111) for the two adsorption geometries, i.e., fcc-hollow vertical and bridge-fcc configuration. The results are summarised in Table 3.5, together with some HREELS experimental data. Recently, Hayashi *et al.* [93] provided strong support to the bridge-fcc adsorption geometry for the methylthiolate on Au(111). They showed an excellent agreement of DFT-based calculated vibrational modes of the bridge-fcc adsorption geometry with experimentally measured HREELS spectra. In the present work, the vibrational spectra obtained for frequencies (ω) $\in$ (220–1413 cm^{-1}) in the case of the bridge-fcc adsorption configuration are in better agreement with the experimental data than the frequencies in the case of the fcc vertical adsorption [see modes' frequencies in Table 3.5]. Therefore, aside from the energetics and the analysis of the PDOS, based on a comparison with experimental data, we also conclude that the adsorption site of the methylthiolate on Au(111) is between fcc and bridge sites, with a tilt angle of the molecular backbone of around 54°.

Table 3.5: Vibrational modes of SCH_3 on Au(111): $\nu_a(CH_3)$ CH_3 antisymmetric stretch, $\nu_s(CH_3)$ CH_3 symmetric stretch, $\delta_a(CH_3)$ CH_3 antisymmetric bending, $\delta_s(CH_3)$ "Umbrella mode", $\rho(CH_3)$ CH_3 rock, ν(S–C) S–C stretch, ν(S–Au) S–Au stretch, R hindered rotation and T frustrated translation.

$\omega(\text{cm}^{-1})$			
Bridge-fcc	Fcc	HREELS Exp. [93]	Description
3087.7	3081.4		$\nu_a(CH_3)$
3067.6	3074.3		$\nu_a(CH_3)$
2979.3	2984.1		$\nu_s(CH_3)$
1413.1	1413.1	1415	$\delta_a(CH_3)$
1408.8	1403.3		$\delta_a(CH_3)$
1276.0	1249.6	1298	$\delta_s(CH_3)$
923.6	868.4	949	$\rho(CH_3)$
902.2	854.1		$\rho(CH_3)$
654.6	620.2	680	ν(S–C)
220.2	189.1	230	ν(S–Au) + R
178.0	174.3		ν(S–Au) + R
152.2	157.3		ν(S–Au)
94.3	96.5		$R + T$
63.4	96.5		$R + T$
63.4	96.5		$R + T$

The Scanning Tunnelling Microscope (STM) is a widely used experimental technique in surface science physics, because it permits direct imaging of a sample with atomic resolution [see Sec. 2.3.4]. However, the interpretation of STM images is complex most of the time, and theoretical simulations result essential for that. In particular, the interpretation of STM images of alkanethiol-based SAMs is not straightforward [99]. In the case of short chain thiols, like methylthiolate, most experiments do not show atomic resolution [100], while for longer chain thiols it is not clear yet whether a c(4×2) or a $(\sqrt{3} \times \sqrt{3})$R30° superstructure is seen [10]. We will focus on this issue later in this chapter.

In order to clarify the role played by the different geometrical degrees of freedom (twist and tilt angle, as well as adsorption site) in determining the aspect of STM images of methylthiolates on Au(111) at high coverages (1ML), we simulate constant current topographical STM images as described in the methodology section [Sec. 2.3.4]. In Fig. 3.13, we show constant current contour plots to simulate STM images for four different adsorption geometries. On the left side, Fig. 3.13a) and 3.13c) correspond to a fully relaxed methylthiolate on the fcc-hollow and bridge-fcc adsorption sites, respectively. On the right, Fig. 3.13b) corresponds to a rotation of the twist angle by 60° (eclipsed orientation [65]) with respect to Fig. 3.13a), while Fig. 3.13d) corresponds to a fcc-hollow site

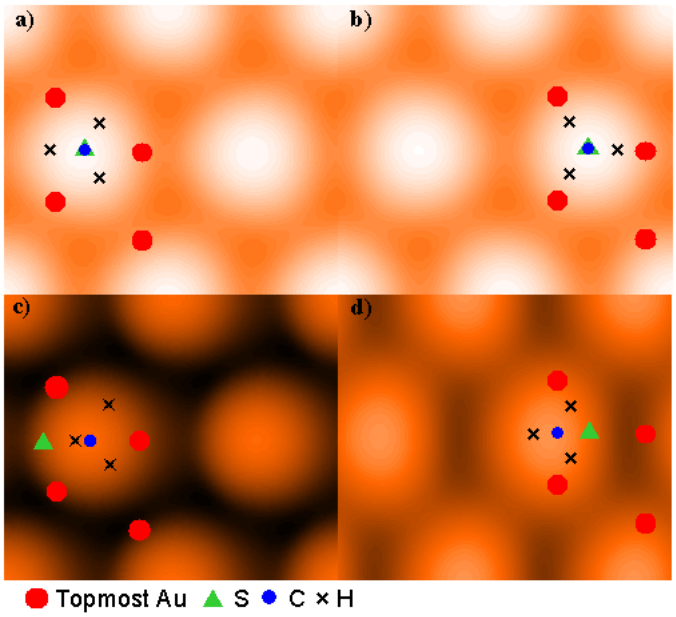

Figure 3.13: Simulated STM images for fcc-vertical staggered orientation a), fcc-vertical eclipsed orientation b), bridge-fcc configuration c) and fcc-hollow tilted d). The local density of states (LDOS) has been integrated up to 1 eV, and the contours have been plotted for the integrated LDOS value of 1×10^{-5} $e^-/\text{Å}^3$.

tilted 30° with respect to the surface normal. In these two latter cases, the geometry does not correspond to a fully relaxed one, i.e, they are not metastable geometries for SCH_3 on Au(111). By comparing figures 3.13a) and 3.13b) we can state that the role of the twist angle in the aspect of the STM image is negligible. However, a comparison between figures 3.13a) and 3.13d) shows that tilted geometries present a higher corrugation as compared to vertical geometries. For the fcc vertical phases the corrugation is $\sim$ 0.6 Å, $\sim$ 0.8 Å for the tilted fcc, and $\sim$ 1.3 Å for the bridge-fcc phase. Finally, comparing Fig. 3.13a) and Fig. 3.13c) we see that STM images with atomic resolution would help in determining the adsorption geometry of methylthiolate on Au(111). In all cases the bright spot in the STM image coincides with the location of the methyl group [56, 81]. These results can be summarised by saying that geometric factors predominate over electronic effects [99, 101]. Very recently Maksymovych *et al.* [95] have probed that comparison between simulated STM images and atomic resolution experimental STM images permits to determine the adsorption geometry of methylthiolate on Au(111). Low temperature experimental STM images of methylthiolate at low coverage show a two-lobed shape, as well as a particular relative position of the lobes with respect the underlaying Au atoms. The higher lobe corresponds to the CH_3 group, and the more diffuse lobe is originated from the S atom. By comparing the experimental images with simulated TH-STM images, they conclude that the shape agrees well only with the case of SCH_3 species chemisorbed on the bridge-fcc configuration.

3.5.2 S, SH, and SCH_3 on fcc

We have concluded, that in the case of methylthiolate and mercapto molecular adsorption, the essential chemisorption features are given by the S–Au bond properties, independently of the nature of the molecular radical. This is also revealed by a comparison with the adsorption of atomic sulphur on Au(111). In order to facilitate the comparison, we analyse the adsorption of sulphur, mercapto and methylthiolate species on fcc-hollow sites in the vertical configuration.

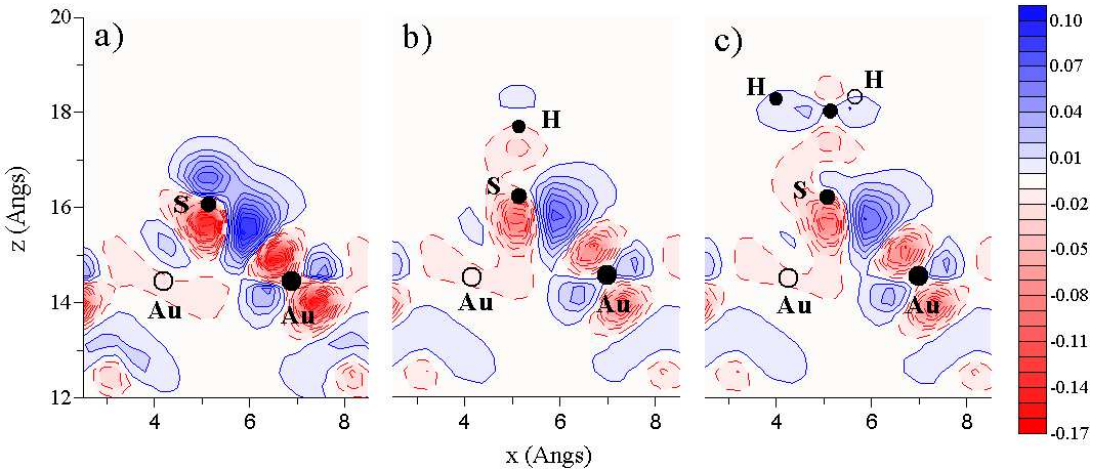

Figure 3.14: Adsorption induced electron densities ($\rho_{\rm ind}$) of S, SH, and SCH_3 fcc vertical adsorption geometry in the $(\sqrt{3}\times\sqrt{3})$R30° cell, plotted in a vertical plane containing the sulphur atom and one Au atom. Positive (electron excess) and negative (electron defect) electron density differences ($e^-/$Å^3) are represented by blue and red colour respectively, and the corresponding colour scale is shown. Filled circles represent atoms that are contained in the plotted plane, empty circles depict out-of-the plane atoms.

In Fig. 3.14, we show a comparison of the induced electron densities for S/Au(111), SH/Au(111) and SCH_3/Au(111) in the fcc vertical adsorption geometry using a hexagonal unit cell (the $(\sqrt{3}\times\sqrt{3})$R30° unit cell). The $\rho_{\rm ind}$ for mercapto and methylthiolate in the vertical plane that contains one S–Au bond are very similar. However, the contour map for S presents two distinct features: (i) the amount of the induced electron density is larger, and (ii) the sulphur atom piles up charge above it. These differences stem from the fact that the two molecules present an S-bond saturated by either C or H. The saturation of one of the sulphur's dangling bonds leads to slightly different chemisorption properties that mainly affects the adsorption geometry (site and orientation) and bond strength. However, the S–Au interaction is qualitatively the same in all cases.

This is also revealed by the PDOS onto the 3p of S atoms, and onto the HOMO of the radical molecules, SH and SCH_3, shown in Fig. 3.15[10]. The energy spreading of

[10]For simplicity, the figure corresponds to a nonspin polarised calculation. However, no generality is lost in the analysis since the spin polarisation effect is negligible upon radical's adsorption on Au(111).

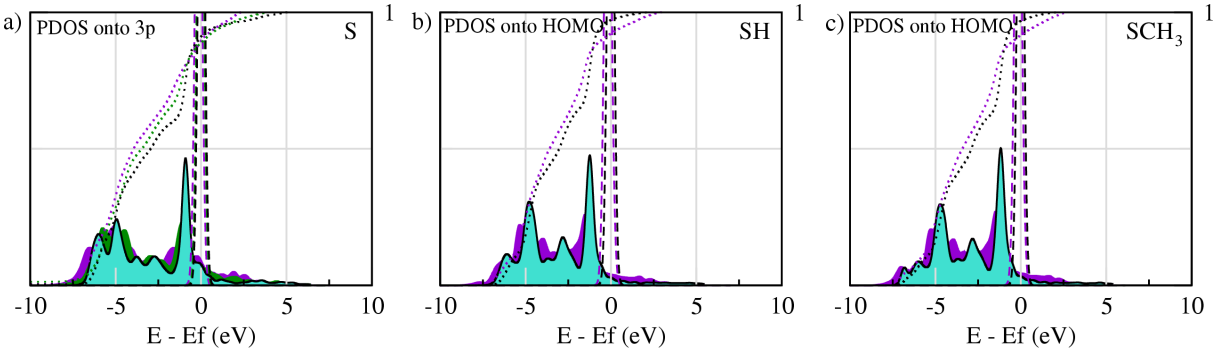

Figure 3.15: Coloured areas are the PDOS onto highest occupied orbitals, a) for S (triple degeneration), b) for SH (double degeneration) and c) for SCH_3 (double degeneration) adsorbed in the fcc site on Au(111). The open-shell structures of the adsorbed species are largely passivated by the substrate, leading to basically populated 3p orbitals in a), and HOMOs in b) and c), as revealed by the integration of the charge depicted by dotted lines. Projection onto the orbitals themselves are also shown by dashed lines, in order to show the very small dispersion of the 3p and HOMO bands in each case.

about 8 eV after adsorption for the HOMO practically covers the whole Au d-band energy range. In particular, the peak at about 1 eV below E_F also appears in PDOS onto Au's atomic d orbitals [see Sec. 3.5.1]. Therefore, Fig. 3.15 shows the important role played by S(3p)–Au(5d) hybridisation in the formation of the S–Au bond, similar to the S–Au dimer studied before in Sec. 3.3. However, the rearrangement of charge after S–Au bond formation shows quite a large degree of charge transfer from Au(111) to the adsorbate as compared to that from Au to S in the S–Au dimer. This is explained by the larger coordination of S atom on the surface.

3.6 SH and SCH_3 on Au(111): the c(4×2) structure

In order to complete the study of thiolate adsorption on Au(111), we investigate possible molecular arrangements of alkanethiol monolayers on Au(111) in a c(4×2)[11] superlattice of the $(\sqrt{3} \times \sqrt{3})$R30° structure. This rectangular unit cell is four times larger than $(\sqrt{3} \times \sqrt{3})$R30°, therefore it contains four molecules. This structure, was primarily observed by a Helium diffraction experiment [102], and further supported by GIXD [103], X-ray standing wave [104] and STM [83–85]. Recent UHV-STM work by Poirier and coworkers [105, 106] has shown that for decanethiol on Au(111) the c(4×2) superstructure is the only one found for full monolayer coverages.

Based on previously suggested models with non-equivalent adsorption sites, we designed some initial geometries for SCH_3, and also for SH on Au(111) within the c(4×2) unit cell. Upon geometry relaxation, we reached different metastable configurations. De-

[11] A more conventional notation would be $(2\sqrt{3}\times3)$ but historically it has been introduced as c(4×2)

pending on the trial configuration one dimer or even two dimers are found in the final metastable configuration, whereas in other cases molecules adsorb tilted on distinct bridge-like[12] sites. In Table 3.6 some of the tested trial configurations for methylthiolate and mercapto are summarised. In order to emphasise the initial configuration dependence, we have included the data of the initial guess, marked with (i). These configurations thus present very large forces on the atoms [sixth column]. The final relaxed structures, (f), are given subsequently. The configurations are described by the S adsorption site with the number of molecules that have that site, i.e., "3 bridge 1 hcp" corresponds to 3 molecules on the bridge site and one on the hcp site. In the case of dimers the adsorption site is difficult to describe. The final structure is basically determined by the S–S distance (d_{S-S}) and the vertical S–surface distance (d_{S-Surf}). In order to complete the description, the smallest S–Au distance is also given (d_{S-Au}). In the case of dimers, two distances are given, one for each S atom. Finally, the energy difference with respect to the most stable configuration is given.

The optimal geometry corresponds to four equivalent methylthiolates adsorbed on bridge-fcc sites corresponding to the hexagonal cell, the $(\sqrt{3} \times \sqrt{3})$R30° structure. This is the first configuration given in Table 3.6. Four mercapto molecules in the bridge configuration correspond also to the $(\sqrt{3} \times \sqrt{3})$R30° structure and to the minimum energy one. These two structures have been previously described in Sec. 3.5.1.

From our results, we conclude that for SCH_3 as well as for SH, there are two critical parameters: (i) the initial vertical distance to the Au surface and (ii) the initial smaller S–S distance. When molecules are initially located far enough from the substrate, ~ 3 Å, and the distance between two sulphur atoms is at most 4 Å, they form a dimer. However, when in the initial configuration molecules are located fairly close to the substrate, less than 2.5 Å, and the shortest S–S distance is at least larger than 2.3 Å, molecules tend to adsorb on bridgelike sites trying to move away from their nearest sulphur neighbour. For the chemisorbed species, the vertical distance to the substrate is around 2 Å, a value in agreement with the adsorption distance in the optimal configuration. Finally, no matter how far from the substrate the molecules are initially placed, provided that they have a periodicity similar to the hexagonal cell, they chemisorb keeping the same S–S distance of 5.1 Å. The fact that the formed dimers have an S–S bond length of ~ 2 Å, similar to the isolated dimethyl disulphide is an indication of the weak interaction with the substrate. Accordingly, they are located far above the surface, further than 3 Å.

Now, we compare the calculated total energies of different relaxed metastable geometries for methylthiolates in the c(4×2) cell to quantify the strength of the formed bonds. We take as reference the energy of the most stable configuration in the large cell, with four methylthiolates adsorbed tilted on bridge-fcc sites, i.e., four times the hexagonal cell. The

[12] A site close to the bridge site but slightly moved away

Table 3.6: Initial (i) and final (f) configurations for SCH_3 and SH in the c(4×2) unit cell. d_{S-S} is the distance between neighbouring sulphur atoms, d_{S-Surf} the vertical distance to the Au surface and d_{S-Au} the shortest S–Au distances. In the case of dimers, two distances are given for each S atom. Max. force is the largest force onto adsorbate's and Au topmost layer's atoms and ΔE is the energy difference with respect to the most stable configuration. All distances are in Å, forces in eV/Å, and energies in eV.

Adsorbate	Sites	d_{S-S}	d_{S-Surf}	d_{S-Au}	Max. force	ΔE
SCH_3	(f) 4 bridge-fcc	5.1	1.9	2.5	0.01	0
	(i) 4 fcc-vert	5.1	3.0	3.5	1.5	-
	(f) 4 fcc-vert	5.1	1.7	2.5	0.04	1.15
	(i) 2 bridge-vert	3.9	3.0	3.3	1.52	-
	2 bridge-vert	5.1	”	”	”	-
	(f) 2 dimer	2.1	2.8-3.2	2.9-3.4	0.02	0.76
	2 dimer	2.1	3.2-3.4	3.3-3.7	”	”
	(i) 3 bridge	5.1	1.9	2.5	10.26	-
	1 hcp	2.3-3.1	1.9	2.4	”	-
	(f) 2 bridge	5.1	1.9	2.5	0.04	0.42
	1 dimer	2.1	2.8-3.0	3.0-3.9	”	”
	(i) 3 bridge	5.1	1.9	2.5	-	-
	1 fcc	3.1-3.7	1.9	2.4	-	-
	(f) 2 bridge	5.0-5.1	1.9-2.0	2.5	0.04	0.19
	2 bridge	3.6-3.7	1.9-2.1	2.5	”	”
	(i) 4 bridge	3.0-5.1	3.0	3.3	-	-
	(f) 2 bridge	3.4-5.4	1.9-2.1	2.5	0.02	0.56
	1 dimer	2.1	3.1-4.2	3.2-4.5	”	”
SH	(f) 4 bridge	5.1	2.0	2.5	0.01	0
	(i) 2 bridge-vert	3.9	3.0	3.3	3.59	-
	2 bridge-vert	5.1	”	”	”	-
	(f) dimer	2.1	3.2-3.7	3.2-3.9	0.03	1.65
	dimer	2.1	3-3.7	3.1-3.9	”	”
	(i) 3 bridge	5.1	2.0	2.5	1.22	-
	1 hcp	3.1-3.7	2.0	2.5	”	-
	(f) 2 bridge	5.1	1.9-2.1	2.5	0.04	0.07
	2 bridge	4.0	2.0-2.1	2.5	”	”
	(i) 3 bridge	5.1	2.0	2.5	0.65	-
	1 fcc	4.2-4.7	2.0	2.7	”	-
	(f) 4 bridge	5.1	2.0	2.5	0.01	0

largest energy difference, excluding the fcc vertical adsorption, corresponds to the case where two dimers are formed, $\Delta E = 0.76$ eV per cell. Thus, it can be considered that each weakly adsorbed dimer is ~ 0.38 eV less stable than the two tilted methylthiolates on Au on bridge-fcc sites. This value approximately agrees with the energy difference obtained for the cases where just one dimer is formed, whereas the other two methylthiolates are adsorbed on bridgelike sites, $\Delta E = 0.42$ eV and $\Delta E = 0.56$ eV. The difference between the values is due to the non-equivalence of the two bridgelike sites and the dimer's adsorption geometry.

We find a structure that has two dimers with an S–S distance of 2.1 Å and the shortest Au–S bond distance of 2.9 Å, see Table 3.6. This structure is the closest one to the one found by Yourdshayan *et al.* [65]. Indeed, they find a 2.4 Å S–S distance and the shortest Au–S bond distance of 2.9 Å. However, their adsorption energy is 0.16 eV more stable per c(4×2) unit cell than four times their most stable hexagonal cell. In our case, we find that four times the hexagonal cell is 0.76 eV more stable than this structure with two dimers. In agreement with Morikawa *et al.* [86], we conclude that the minimum energy configuration corresponds to the $(\sqrt{3} \times \sqrt{3})$R30° structure.

In a recent paper by G. Scoles and coworkers [69], based on molecular dynamics simulations at finite temperatures, it is found that two different configurations exist in dynamic equilibrium, since the energy barrier between them is small. The most stable configuration appears after significant reconstruction of the Au(111) surface upon adsorption. Therefore, our calculated most stable structure at T = 0 K could well be a metastable structure too.

3.7 Summary and conclusions

Through this chapter, we have presented a detailed computational study of the S–Au bond for the adsorption of S atoms, as well as SH and SCH_3 radical molecules on Au(111).

In order to rationalise our findings, we have first analysed free dimers of S atoms with noble metal atoms (Cu, Ag and Au). S–Cu dimer presents the largest binding energy, in agreement with the larger reactivity of Cu in the noble metal family. However, the S–Au dimer follows closely, showing the uniqueness of the S–Au bond. The particularities of this bond are further revealed when studying dimers containing O atoms. Indeed, O is very reactive, and a binding energy larger than the one of S-containing dimers was expected. This is the case of dimers containing Cu and Ag, but the S–Au dimer is more strongly bound than the O–Au dimer. A simple explanation of this behaviour is traced back to the extension of the orbitals of the different atomic components. Au atoms present the most compact s and p orbitals and an enhanced extension of the d orbitals, among

noble metals. This is a purely relativistic effect that privileges the binding with the more extended S atom. Hence, the S–Au bond presents very interesting properties due to the relativistic nature of gold's electronic structure.

Although the binding on an extended Au(111) surface is somewhat different from the local dimer picture, e.g., a higher coordination of adsorption sites appears, the essential features of the S–Au bond are already contained in the dimer: the sharing of charge forming the bond originated to a large extent from S(3p) and Au(5d) orbitals. However, the spatial distribution of this rearrangement of charge differs. Furthermore, the two different S-containing radicals under study (SH and SCH_3), present very similar adsorption properties. Indeed, the computed electronic structures are basically the same: charge transfer from the Au(111) substrate to the radical is large, reaching an almost complete saturation of the radical's HOMO, and partial filling of the LUMO. The main difference between the adsorption states of the two molecules is due to steric forces, which determine the different adsorption geometries. Steric forces also explains the reason why bridgelike adsorption sites are energetically favoured with respect hollow sites. In the case of methylthiolate, comparison of calculated vibrational modes with experimental HREELS spectra confirms that the actual adsorption geometry is the bridge-fcc, while STM simulations show that the aspect of STM images is determined by geometrical factors, like adsorption site and tilt angle that cannot be treated separately.

Finally, we have addressed the controversy on the actual lowest energy molecular configuration of methylthiolate adsorption. Despite the experimental and theoretical indications of a possible c(4×2) phase, our calculations at T = 0 K conclude that the minimum energy configuration corresponds to the $(\sqrt{3} \times \sqrt{3})$R30° structure. We have studied many different initial configurations, and in the course of relaxation we have either retrieved the $(\sqrt{3} \times \sqrt{3})$R30° structure or we have finished in higher-energy conformations.

Chapter 4

TTF-TCNQ charge-transfer complex on Au(111)

This chapter is focused on the study of tetrathiafulvalene (TTF, $C_6H_4S_4$) and 7,7,8,8-tetracyanoquinodimethane (TCNQ, $C_{12}H_4N_4$) adsorption and self-assembly on the Au(111) surface. It is divided in different sections. A first section briefly introduces the TTF-TCNQ organic crystal, and the motivation to study this organic–metal system. Next, DFT calculations of the individual adsorption of both types of molecules are presented, where references to experimental results are given too. Later on, the structural properties of the TTF-TCNQ supramolecular assembly are also described with the help of STM experiments and simulations. Finally, the last two sections are devoted to the characterisation of the electronic properties of the TTF-TCNQ and Au(111) interface. Combined local STS measurements and DFT calculations show the formation of dispersive hybrid bands at the organic-metal interface, with both metallic and molecular character.

4.1 Introduction

4.1.1 Organic-Metal interface: Hybrid bands

Over the last few decades, the development of organic-based electronic devices has attracted a lot of interest. Organic materials are interesting in diverse fields due to their ease of processing and the tunability of their properties by selectively modifying functional end groups [8]. In particular, attention has been paid to the growth of organic thin films, where organic compounds are deposited on low-cost substrates like glass, plastic or metals. Thanks to the recent advances in understanding the properties of such films [10, 107] there are already several devices based on organic materials. Organic-light emitting diodes (OLEDs) [108, 109], photovoltaic solar cells for energy conversion [110–112], and organic

thin film transistors (OTFTs) [113] are examples of such electronic devices.

The strong metallic or covalent bonds between the atoms that form inorganic crystals cause charge carriers to be delocalised and to move in wide bands with high mobility. In contrast, due to weak intermolecular interactions, organic materials inherently have narrow bands and, thus, low electron mobility [114]. In order to use organic thin films in electronic devices it is important to have electronic bands with high conduction properties. That is why organic-inorganic hybrid materials are subject of an increasing interest. They would combine the high carrier mobility of metals with the advantages of the organic compounds, i.e., their low-cost, growth easiness and their modifiable electronic properties by using organic synthesis [115]. Organic-metal (OM) hybrid materials open new perspectives for developing organic-based electronic devices with improved efficiency. However, this approach remains sustained on empirical bases. A conceptual picture at the molecular scale describing the formation of OM hybrid bands is still missing [116].

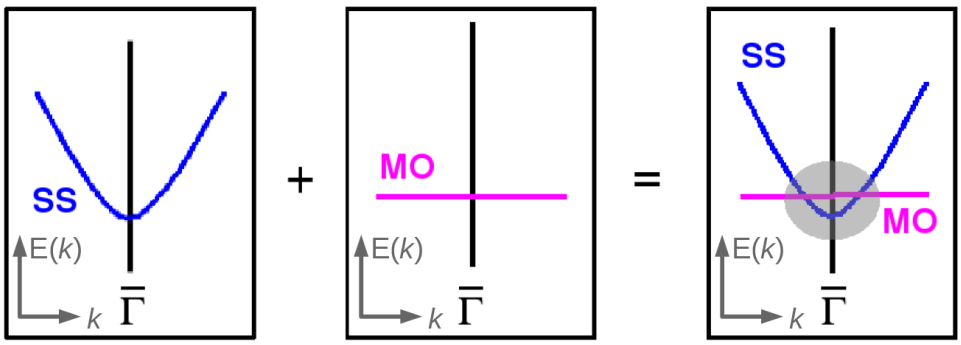

Figure 4.1: Schematic illustration of the interaction between metallic dispersive bands (blue) with localised molecular orbitals (pink) at the organic-metal interface. Main interaction occurs at the crossing of the metallic band and the molecular orbital (around $\overline{\Gamma}$ in this particular case).

The electronic structure of an OM interface is determined by the interaction between molecular and metal states. Fig. 4.1 illustrates the situation at the OM interface. The metallic dispersive bands, like the surface state (SS), may interact with the localised molecular orbitals (MO). This interaction causes re-alignment, splitting, and broadening of molecular states as a response to charge transfer, structural distortions, and hybridisation with metal states [117, 118]. These processes usually mask the properties of the molecular thin film, and the interface band structure is dominated by the highly dispersive metal states [119]. For example, when there is a weak coupling between planar molecules and a metallic substrate, like Au(111), the surface state just shifts due to induced dipoles [120]. Furthermore, molecules at the OM interface can scatter [121] and confine metal surface states [122], or mix with them [123]. Therefore, if one aims to design functional OM interfaces, a detailed understanding of the basic principles behind these interactions is essential.

4.1.2 TTF-TCNQ organic crystal

The molecules selected for this study, TTF and TCNQ, are known because they were use more than 30 years ago in the synthesis of the first organic metal based on a charge-transfer complex [124]. The molecular charge-transfer complexes are formed upon interaction of a *donor* and an *acceptor* molecule. The donor molecule has a small ionisation energy (IP), while the acceptor molecule is characterised by a large electron affinity (EA). The result of the interaction is that the donor molecule losses charge (oxidises) and the acceptor gains charge (reduces), forming a charge-transfer salt. In some cases, these donor–acceptor interactions give rise to the formation of crystalline solids, in which organic molecules are stacked in homomolecular chains. Within the chains the interaction between neighbour molecules is driven by the overlap of the π molecular orbitals, i.e., it has $\pi - \pi$ character. This increases the mobility of the charge carriers. The overlap leads to the formation of bands within the organic crystal. Nevertheless, the properties of such bands differ from metallic bands. The effective carrier mass, m^*, is typically larger than the mass of the free electron (m_e) [125–127].

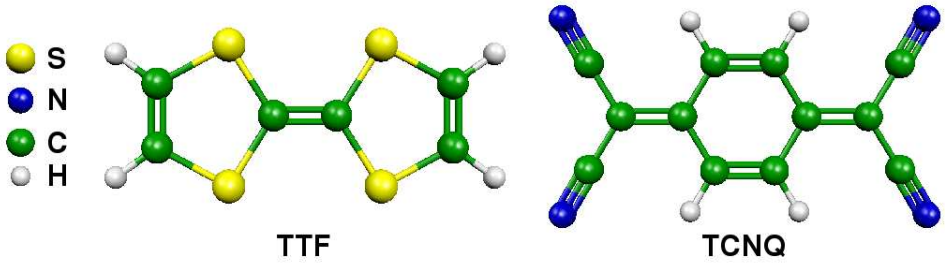

Figure 4.2: Scheme of the TTF (donor) and the TCNQ (acceptor) molecules.

TTF has a donor character with a gas phase IP of 6.83 eV [128], while TCNQ is an acceptor molecule with an EA of 2.8 ± 0.1 eV [129]. Fig. 4.2 shows the structure of both molecules. TTF-TCNQ crystallises through non-covalent interactions, in a well-defined structure with alternating linear stacks of planar TTF and TCNQ molecules . The stacks are oriented along one crystallographic direction b, as shown in Fig. 4.3a). TTF-TCNQ bulk structural and electronic properties have been extensively studied [131–134]. The formation of bands due to the overlap of π orbitals, and their partial occupation at the Fermi level is the origin of the metallicity of the compound. Free carriers, either holes or electrons, are generated in both stacked molecular rows, thanks to the charge transfer from the highest occupied molecular orbital (HOMO) of TTF to the lowest unoccupied molecular orbital (LUMO) of TCNQ. This charge transfer accounts for 0.6 e^-, and is delocalised along the b direction of the crystal. It results in a quasi-one-dimensional electron dispersion that has been described by DFT calculations [130] [see Fig. 4.3b)], as well as experimentally observed [135].

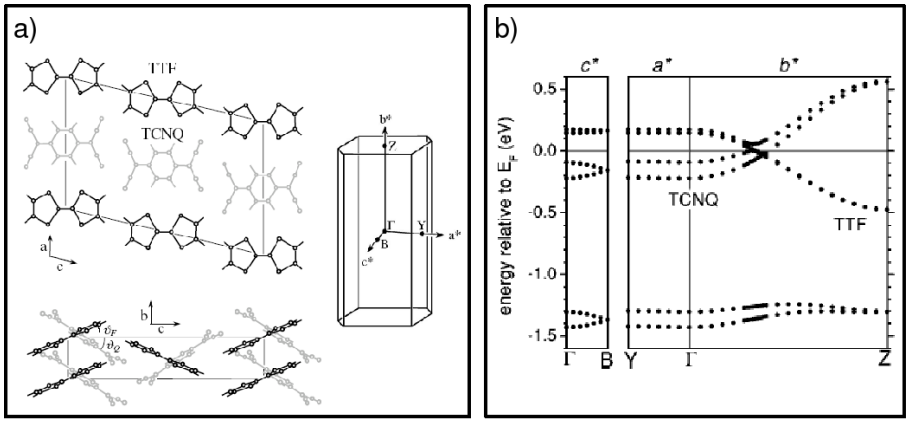

Figure 4.3: a) Crystal structure of TTF-TCNQ showing the main directions a, b and c of the unit cell. On the left, the monoclinic Brillouin zone with its high symmetry points is shown. b) DFT band structure near the Fermi level along the three major high-symmetry lines of the Brillouin zone of the TTF-TCNQ crystal [130].

At room temperature, the TTF-TCNQ organic crystal is highly conducting. However, at low temperature, the compound undergoes two Peierls transitions[1] and becomes an insulator. These phase transitions are associated to the one-dimensionality of the material [133].

On going from bulk TTF-TCNQ to the organic thin film deposited on a metal substrate, it is expected the organic-metal interface to play a key role in the electronic properties of the organic layer.

4.2 Computational details

First principles calculations, following the procedure described in Chapter 2, have been performed to account for the ground-state electronic structure of the studied systems: TTF/Au(111), TCNQ/Au(111), and TTF-TCNQ/Au(111).

We start our study with the isolated molecules, then the molecules adsorbed on Au, and finally the SAM on Au. For all the calculations presented in this chapter, we used energy cutoffs of 280 eV and 440 eV for electronic wavefunction and the augmentation charge density expansion in plane waves, respectively. Energy convergence was required to be lower than 10^{-6} eV. The size of the cells was sufficiently large to use only one k-point, the Γ point, and get reasonable precise geometries and energies. However, in the case of TTF-TCNQ/Au(111), as we were interested in subtle electronic details, the number of k-points was increased to 15 k-points in the full Brillouin zone.

[1]There are two independent Peierls phase transitions, at 54 K for the TCNQ chains and at 38 K for the TTF chains

Isolated TTF and TCNQ: To calculate the ground-state of isolated TTF and TCNQ molecules, we used a 15×10×10 Å^3 unit cell, and the positions of all atoms were optimised until all forces were lower than 0.01 eV/Å.

TTF/Au(111) & TCNQ/Au(111): Next, both isolated TTF and TCNQ, were adsorbed in a c(6×4) Au(111) slab made of four layers of gold and 24 atoms per layer, with 14 Å of vacuum. Although in this case, geometries were relaxed only down to forces of 0.05 eV/Å.

2D pure TCNQ & 2D TTF-TCNQ: In the case of periodic structures, pure TCNQ phase and TTF-TCNQ mixed phase, the initial guess of the geometries was based on the experimental unit cells. These unit cells were deduced from the STM images that will be presented in the following sections. In this case, the positions of all atoms were optimised down to forces of 0.01 eV/Å.

2D TCNQ on Au(111): To perform the calculation of the periodic TCNQ overlayer adsorbed on Au(111), we used a c(5×3) unit cell that contains a slab with 15 Au atoms per layer and four layers of Au. This Au slab was further passivated with hydrogen atoms on the bottom to quench one of the Au(111)'s Shockley surface states close to the Fermi level[2]. The details about how gold's surface state can be described using a periodic supercell made by only four layers of Au and passivated with hydrogen in one of the sides of the slab, can be found in Appendix I of this thesis. Atomic relaxations were done, until all forces were lower than 0.05 eV/Å.

2D TTF-TCNQ on Au(111): Finally, in the case of TTF-TCNQ overlayer adsorbed on Au(111), we used a unit cell containing 19 Au atoms per layer, that will be named C19. The vectors of this unit cell can be written as a function of the 1×1 cell's vectors:

Au(111) 1×1:

$$\begin{Bmatrix} a_1 = a_s & 0 & 0 \\ b_1 = \sin 30° a_s & b_2 = \cos 30° a_s & 0 \\ 0 & 0 & c_3 \end{Bmatrix}$$

Au(111) C19:

$$\begin{Bmatrix} 6a_1 & -2b_2 & 0 \\ -b_1 & 3b_2 & 0 \\ 0 & 0 & c_3' \end{Bmatrix}$$

where, $a_s = \sqrt{2}/2a_0$, and $a_0 = 4.17$Å is gold's bulk lattice constant.

This C19 Au(111) substrate consists in four atomic layers and has around 14 Å of vacuum. As before, in order to remove one of the Au(111)'s Shockley surface states, we also passivated this Au slab with H atoms at the vacuum metal interface opposite to where the adsorbed molecular overlayer sits. This is essential to analyse

[2]A symmetric slab of a noble metal has two (111) faces, hence two Shockley surface states [136], each located at each side of the slab.

in detail the OM interface. In the geometry optimisation process, due to the large size of the cell and the number of k-points (15 points), only the molecular overlayer, the H atoms and two Au layers were allowed to move. The forces we relaxed down to 0.05 eV/Å.

All the results compiled in this chapter do not take into account spin polarisation. For the TTF-TCNQ/Au(111) system, spin polarised calculations were also performed, although within the accuracy used in the calculation the effect turned out to be negligible. Indeed, it may be that the passivation of the Au(111) slab with hydrogen affects the spin polarisation, as it seems to be the case in other systems. However, we did not go beyond in the present study.

4.3 STM experiments and theoretical simulations

The experiments were carried out at the Freie Universität in Berlin (Germany) [137]. A custom-built Low-Temperature STM, working in ultra-high vacuum (UHV), was used in the experiments. The deposition of molecular overlayers was done on an atomically clean Au(111) surface[3] by molecular sublimation from the commercial solid compound Aldrich. The sublimation of molecules was done in a sequential fashion in UHV from a home-made evaporator that consists of three crucibles with independent heating.

In TTF and TCNQ ultra thin film preparation, either individual TTF and TCNQ powders, or the TTF-TCNQ molecular compound were used. The sublimation temperatures in those powders are slightly different for each type of molecule. TTF sublimates at room temperature from the pure powder, but its sublimation temperature from the mixed compound is around 70°C. In the case of the TCNQ, 120°C is the sublimation temperature from the pure powder, and 140°C from the mixed compound. The preparation of the TTF-TCNQ thin film is better controlled by previously depositing TTF from the mixed compound, followed by a subsequent addition of TCNQ from the pure powder.

In general, for low substrate temperatures, molecular diffusion is hindered, and adsorbates pin to their initial adsorption places. When the temperature is increased, molecules have sufficient kinetic energy to overcome the diffusion barrier and they can find the most favourable adsorption sites. Therefore, the substrate temperature during deposition is important in the formation of distinct assemblies. In this case, the Au(111) substrate was held at 80 K. Nevertheless, the heteromolecular TTF-TCNQ structure shown in Sec. 4.3.3 needs to be thermally activated with a minimum temperature of 150 K. Once the self-assembled monolayer is formed the whole sample is cooled down to 4.8 K, which is the operating temperature for data acquisition (STM topography and spectra).

[3]The Au(111) sample was cleaned under UHV conditions by multiple sputtering-annealing cycles.

This section is mainly focused on the adsorption geometry and energetics of the systems under study. Theoretical simulations are contrasted with experimental STM images.

4.3.1 TTF on Au(111): A chemisorbed system

The TTF molecule contains two rings formed by sulphur atoms. Therefore, in the light of what we have learnt about S–Au interaction in the previous chapter, it is expected to have a stronger interaction with the substrate than TCNQ. Indeed, this is confirmed by theoretical calculations. Fig. 4.4 shows the interaction curves of TTF monomer, TCNQ monomer and TTF-TCNQ dimer[4] adsorbed on Au(111), i.e., binding energy [Eq. (2.18)] against surface–molecule vertical distance. Each point of the plot corresponds to the energy of the adsorbate frozen at a given vertical distance from the substrate. The data have been fitted with a Morse potential[5]. The resulting values of the vertical distance

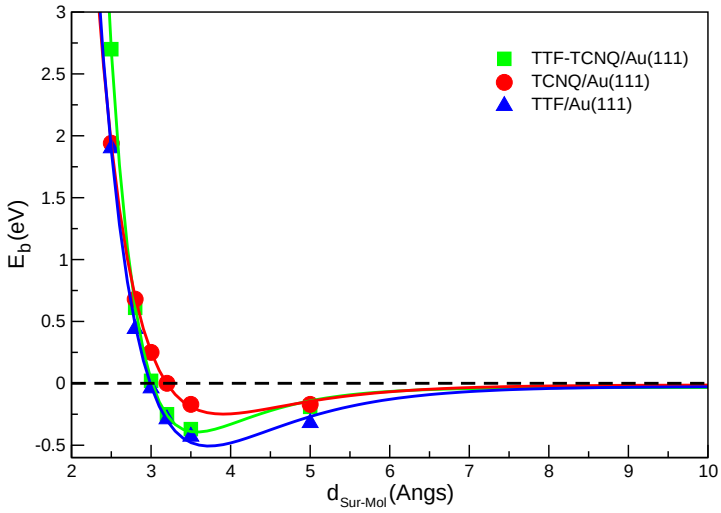

Figure 4.4: Interaction curves for TTF monomer, TCNQ monomer and TTF-TCNQ dimer adsorption on Au(111). Solid lines are the fittings to a Morse potential.

($d_{Surf-Mol}$) and binding energy (E_b) at the minima are summarised in Table 4.1. It can be seen that TTF has the largest E_b, but TTF-TCNQ binary phase seems to have a closer equilibrium adsorption distance. However, these values result from non-relaxed structures, thus, full optimisations may be relevant in this case.

According to DFT optimisation of the adsorption geometry, TTF's interaction with the surface is driven by S–Au bonds. The only way to optimise the S–Au coordination is by tilting the molecular plane with respect to the gold surface. The binding energy after geometric relaxation is -0.59 eV. Two sulphur atoms are adsorbed on top sites, with a S–Au bond distance of 2.90 Å; while the other two sulphurs are located on bridge sites further

[4]The unit cell corresponds to the periodic TTF-TCNQ mixed system, that has a dimer per unit cell.

[5]Morse potential: $y = a_0 + a_1 \left(1 - e^{-a_2(x-a_3)}\right)^2$

Table 4.1: Fitted values of surface–molecule vertical distance ($d_{Surf-Mol}$) and binding energy (E_b) at the interaction curves minima obtained from non-relaxed structures.

System	$d_{Surf-Mol}$ (Å)	E_b (eV)
TTF/Au(111)	3.73	-0.51
TCNQ/Au(111)	3.91	-0.25
TTF-TCNQ/Au(111)	3.57	-0.39

away from the surface [see Fig. 4.5a)]. The tilt angle from planar adsorption accounts for $\sim 10°$. This is in accord with previous calculations, and explains the asymmetry observed in experimental STM images at negative bias. There, the image is dominated by the shape of the TTF HOMO where the main contribution originates in the S atoms [see Fig. 4.5b) & 4.5c)]. Fernández-Torrente *et al.* [139], based on statistical analysis of

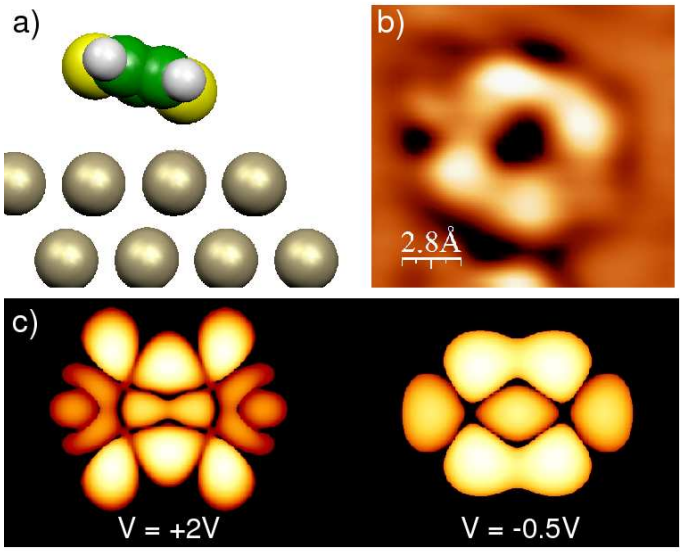

Figure 4.5: a) Side view of the fully relaxed geometry of TTF/Au(111). b) Experimental STM image of a TTF monomer on Au(111) (V = -0.03 V, I = 0.3 nA). c) Tersoff-Hamman constant current STM images of isolated TTF[a]. Left panel V = +2 V, and right panel V = -0.5 V, corresponding to the LUMO and HOMO orbitals, respectively.

[a]Simulations done with the WSxM software [138]

STM experimental images for different TTF coverages, have suggested that the molecular adsorption is based on long-range repulsive interactions of electrostatic nature. They assert that the chemisorption through covalent S–Au bonds results in charge transfer from the donor molecule to the substrate, leading to an electrostatic lattice formation. They show different self-assembled TTF patterns depending on the different TTF coverages, and explain them as a result of a competition of long-range repulsive interactions and short-range hydrogen bonding forces that start to play a role at high coverages.

4.3.2 TCNQ on Au(111): A physisorbed system

STM experiments show that TCNQ forms highly ordered self-assembled extended domains on the Au(111) surface [140]. STM images show that superimposed on the molecular corrugation, the herringbone reconstruction of Au survives underneath [Fig. 4.6a)]. This is considered to be a fingerprint of a weak interaction between the molecular layer and the surface. Furthermore, the strong resemblance of the molecular shape of STM images taken at positive bias [Fig. 4.6b)] with the LUMO of the isolated TCNQ molecule [Fig. 4.6c)], also suggests a weak adsorption, i.e., physisorption of TCNQ on Au(111). It has been reported that for weakly adsorbed molecules, the intramolecular structure resolved by STM can be usually correlated to the shape of the molecular orbitals [141]. In spite of this weak adsorption, TCNQ islands exhibit a certain degree of commensuration with the Au(111) lattice.

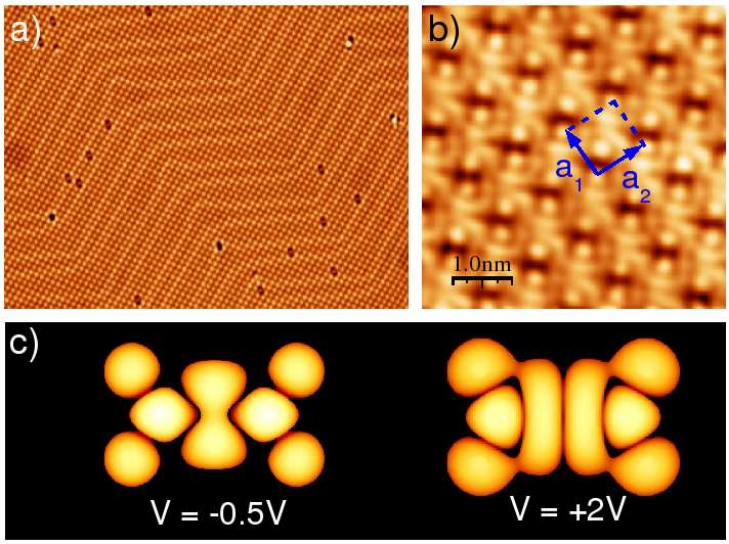

Figure 4.6: a) Large STM area of a self-assembled domain of TCNQ. The characteristic herringbone reconstruction of Au(111) is visible underneath. b) Zoom with intramolecular resolution in a TCNQ island (V = 0.8 V, I = 0.32 nA). The experimental rhombic unit cell vectors are $a_1 = a_2 \sim 10$ Å [137]. c) Tersoff-Hamman constant current STM images of isolated TCNQ. Left panel V = -0.5 V, and right panel V = +2 V, corresponding to the HOMO and LUMO orbitals, respectively.

The experimental unit cell is rhombic with lattice vectors $a_1 = a_2 \sim 10$ Å [see Fig. 4.6b)]. The self-assembled structure is stabilised by a saturated C–N$\cdots$H–C hydrogen bond (H-bond) network. Each TCNQ molecule has eight H-bonds shared with four neighbouring molecules. A model of this assembly is depicted in Fig. 4.7a). Based on this experimental unit cell, we performed DFT calculations of the free standing monolayer of a bidimensional phase of pure TCNQ. We find out that the length of the H-bonds is ~ 3.0 Å, and the stabilisation energy of the free standing monolayer is -0.39 eV per unit

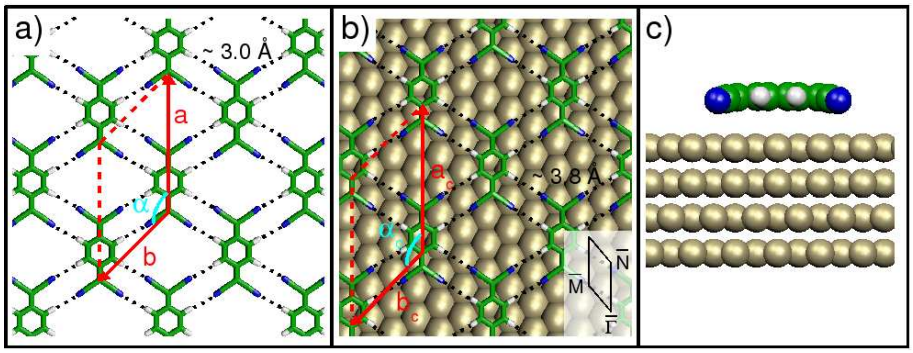

Figure 4.7: a) Model of non-commensurable 2D-TCNQ phase. The vectors a = 14.0 Å, and b = 9.9 Å, define the unit cell with $\alpha = 135°$, and H-bonds' length is $\sim$ 3.0 Å. b) Forcing commensuration with Au(111), unit cell vectors expand to a_c = 14.7 Å and b_c = 10.6 Å with $\alpha_c = 133.9°$, and H-bonds expand to $\sim$ 3.8 Å. Inset shows the corresponding surface Brillouin zone[a]. c) Bent adsorption of TCNQ monomer on Au(111).

[a]The surface Brillouin zone (SBZ) is defined by the points $\overline{\Gamma}$= (0,0), $\overline{N}$= (0,1/2) and $\overline{M}$= (1/2, 1/2) in units of the reciprocal cell vectors.

cell (each cell contains one TCNQ molecule and four H-bonds). The stabilisation energy, similar to the binding energy defined by Eq. [2.18], is defined as, $E_{St} = E_{2D} - E_{TCNQ}$, where E_{2D} is the energy of the free standing overlayer, and E_{TCNQ} is the energy of the isolated TCNQ molecule[6]. Now, if one aims to study the adsorption of this monolayer on Au, we need to force the dimension of the monolayer to be commensurate with the theoretical Au(111) substrate. In such a case, the whole structure has to be expanded[7]. The H-bonds' length increases to 3.8 Å [see Fig. 4.7b)], and the stabilisation energy decreases to -0.21 eV/cell or $\sim$ 53 meV per H-bond. This "extended H-bond" is longer than the typical H-bond [142, 143]. However, in such weakly adsorbed systems is more important to be aware of the intrinsic limitations of DFT.

The adsorption geometry of isolated TCNQ on Au(111), and the molecule within the H-bond network is quite similar. This agrees with weak H-bonds not modifying appreciably the molecular structure. The four nitrogens tend to adsorb closer to the surface than the central carbon-ring. Therefore, the molecule appears slightly bent [Fig. 4.7c)]. The vertical distance from the N atom to the surface, d_{N-Surf}, is $\sim$ 3.45±0.15 Å, and the vertical distance from the central ring $\sim$ 3.75±0.15 Å[8]. In the case of the periodic phase, we can define two different binding energies, $E_{b1} = E_{Surf+Ads} - E_{2D} - E_{Surf}$, that accounts for the strength of the bonding with the surface, and $E_{b2} = E_{Surf+Ads} - E_{TCNQ} - E_{Surf}$, that also computes the binding due to the interaction between molecules. E_{b1} = -0.09±0.03

[6]The unit cell in the two calculations is different, so the error when evaluating energy differences increases.

[7]Experimental lattice constant of Au is 4.08 Å, and theoretical lattice constant 4.17 Å.

[8]Dispersion of ±0.15 arises from the different values obtained in the non-passivated and the passivated Au surfaces.

eV, and E_{b2} = -0.28±0.03 eV. Hence, $E_{b2} - E_{b1}$ = -0.19 eV/cell is the binding energy between the TCNQ molecules within the assembly. This value compares well with -0.21 eV obtained previously without substrate. Moreover, as reported in other molecular assemblies, it agrees with the fact that the strengthening of the surface–adsorbate interaction leads to a weakening of the adsorbate–adsorbate interaction.

So far, based on STM images and DFT calculations, we conclude that the interaction between TCNQ and Au(111) must be relatively weak. Therefore, one would not expect a significant charge transfer between the molecule and the substrate. Nonetheless, TCNQ has a strong acceptor character (at least with respect TTF). Scanning tunneling spectroscopic (STS) measurements provide interesting information to clarify the electronic properties at the OM interface of this system. In Fig. 4.8a) differential conductance spectra taken on clean Au(111) and a TCNQ island are shown. The spectrum taken on the TCNQ island exhibits two distinct fingerprint not present in the bare Au(111) surface: i) a broad resonance located at 0.7 eV, and ii) a shift of $\sim$ 150 meV of the onset of the Au(111) surface state signal towards the Fermi level [140].

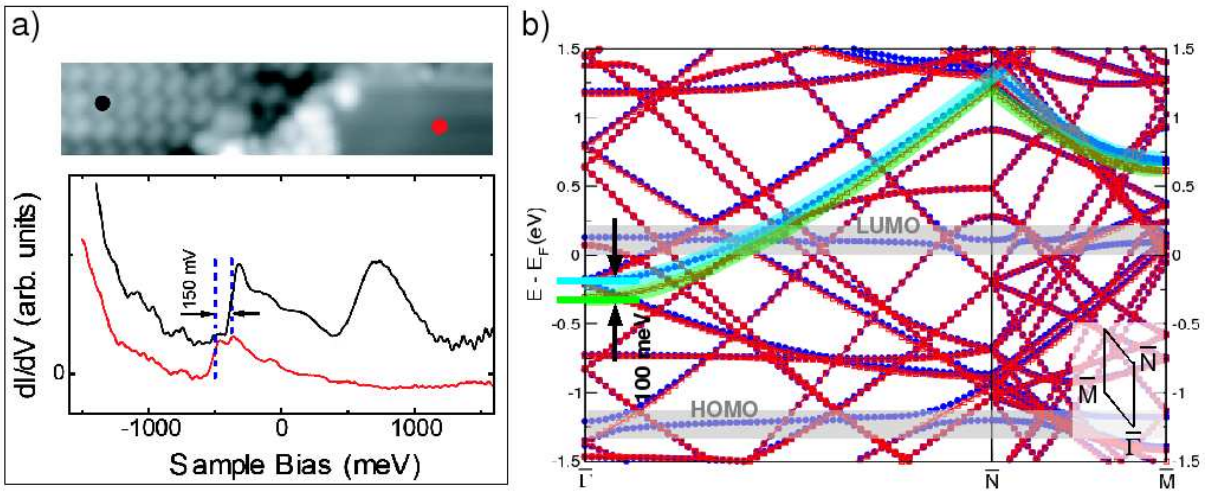

Figure 4.8: a) STS spectra taken on clean Au(111) (red curve) and a TCNQ island (black curve). The black curve has two distinct features, namely, a broad peak at 0.7 eV and a shift of the Au(111) surface state's onset. b) Calculated band structure of Au(111)+H slab (red dots), and TCNQ/Au(111)+H system (blue dots), plotted along the $\overline{\Gamma N}$ and $\overline{NM}$ directions of the SBZ. The bands that do not match in both systems, and do not disperse at all, can be associated to the MOs of TCNQ (grey shadow). TCNQ molecules hardly interact with neighbouring molecules, their orbitals stayed localised and thus do not disperse. A shift between the bare Au(111) SS (green shadow) and the perturbed SS upon molecular adsorption (blue shadow) can be also seen.

The molecular resonance at 0.7 eV can be identified as the TCNQ LUMO. Topographic images taken at bias voltages close to that value, show contour shapes that resemble the LUMO [see Fig. 4.6b) & 4.6c)]. The fact that this resonance is located far away from the Fermi level, suggests that there is no charge transfer from the metal into this state. Shifts

of the metal surface state (SS) have been reported for different types of adsorbates on noble metal surfaces [120, 120, 144, 145]. The observed shift of the onset of the Au(111) surface state is due to changes in the surface potential. These changes are attributed to the presence of the molecular layer, that induces surface dipoles or even charge transfer, depending on the strength of the molecule–substrate interaction. In this particular case, charge transfer can be excluded, proving the weakness of the interaction between TCNQ and Au(111).

Now, we analyse the calculated band structure along main directions of the SBZ, in order to contrast the experimental findings. Fig. 4.8b) shows the band structure of the passivated Au(111) c(5×3) cell (red points) together with the band structure of the bidimensional TCNQ phase adsorbed in the same surface unit cell (blue points). The interaction of TCNQ with the substrate is thought to be weak, as concluded before. Hence, we do not expect large perturbations in the electronic structure of either the metal substrate, or the adsorbed molecular layer. By comparing the band structure with and without the molecules, we can extract information about the induced electronic properties or new states. It can be seen that most of the band structure matches in both systems. However, the system with TCNQ layer exhibits two extra planar bands [marked in grey shadow in Fig 4.8b)]. One occupied state located at $\sim$ -1.2 eV below E_F, and another one unoccupied located at $\sim$ 0.1 eV above E_F. They are the HOMO and the LUMO of the TCNQ molecular layer respectively, as it can be verified by looking the spatial charge distribution at different k-points. Furthermore, we also identify the bare Au(111) dispersive surface state [marked in green shadow in Fig 4.8b)]. It can be seen that upon molecular adsorption an upward shift of this band is induced [marked in blue shadow in Fig 4.8b)]. This shift accounts for 100 meV, and agrees with the experimentally observed shift of the Au(111) surface state.

In contrast, the theoretical position of the LUMO does not agree with the position determined from the STS measurements [0.1 eV *vs* 0.7 eV]. We assign this difference to both a well known DFT underestimation of the HOMO-LUMO gap, as well as to a limited reliability of the alignment of molecular orbitals with the substrate Fermi level when the interaction between them is weak [116, 146]. Unfortunately, the HOMO of the TCNQ was not accessible in the STS experiment, so that, we have no possibility to compare the experimental and the theoretical band-gaps. In practice, the Fermi level is essentially determined by the electronic states of the substrate. The calculated positions of the frontier orbitals with respect to the Fermi level could be wrong, and one has to be careful when extracting conclusions based only in that information. In our calculations, the LUMO is aligned at the Fermi level. That is, the TCNQ gets some charge from the Au substrate. In fact, a Bader charge transfer analysis gives a transfer of 0.30 e^-, which is against to experimental evidence.

4.3.3 Mixed adsorption of TTF and TCNQ on Au(111)

When both molecules are co-deposited, provided a minimun temperature for thermal activation ($\sim$ 150 K), they recognise each other and self-assemble into mixed ordered domains.

The heteromolecular structures vary with the concentration of each molecular species. After co-deposition with excess of TCNQ molecules, there is a preferential formation of a 1:1 stoichiometric phase of alternating donor and acceptor rows, while the surplus of TCNQ nucleates in homomolecular islands [Fig. 4.9]. A highly anisotropic molecular structure, with one-dimensional homomolecular chains is formed. On the contrary, an excess of TTF reveals the formation of a mixed phase with 2(TTF):1(TCNQ) stoichiometry, which has been described elsewhere [137]. Here, we will focus on the study of the 1:1 mixed phase.

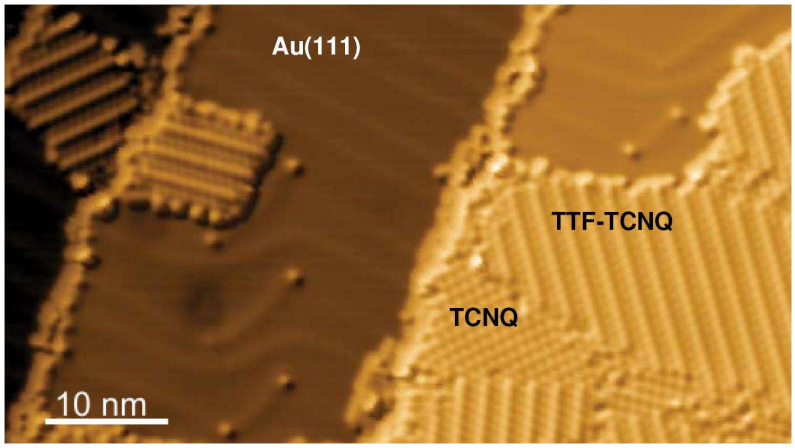

Figure 4.9: Large scale STM image obtained by co-deposition of TTF and TCNQ on Au(111) with excess of TCNQ (V = 1.7 V, I = 0.1 nA). The 1:1 mixed domains of alternating TTF and TCNQ rows follow different orientations according to the symmetry of the underlaying substrate. Surplus of TCNQ molecules appears segregated in pure islands.

The 1:1 stoichiometric TTF-TCNQ phase brings to mind the anisotropy of the bulk structure presented in Sec. 4.1.2. However, while in the crystal the molecules within the rows are stabilised by $\pi-\pi$ interactions, in the thin film TTF and TCNQ lie almost parallel to the surface, as it can be deduced from their intramolecular structure [Fig. 4.11a)] and confirmed by *first principles* calculations. The imaged TTF isosurfaces at positive bias are very similar to the HOMO's shape of the isolated TTF [see Fig. 4.5]. The orbital structure of the TCNQ changes slightly as compared to the pure island, but it still resembles the shape of the LUMO [see Fig. 4.6].

Based on experimental images we can guess a model of the planar self-assemble TTF-TCNQ structure built up by an H-bond network (C–N$\cdots$H–C). We used this unit cell to perform calculations of the free standing TTF-TCNQ monolayer [Fig. 4.10]. We find

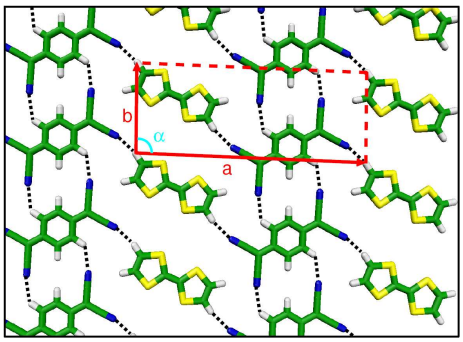

Figure 4.10: a) Relaxed geometry of non-commensurable TTF-TCNQ free standing monolayer. The vectors a = 19.6 Å, and b = 7.8 Å, define the unit cell with $\alpha = 91.6°$. Frontal H-bonds (TCNQ–TCNQ) are 2.5 Å, and lateral H-bonds (TTF-TCNQ) are 2.3 Å and 2.9 Å.

that the length of the H-bonds varies from 2.3 Å to 2.9 Å. The stabilisation energy of the monolayer, defined as, $E_{St} = E_{2D} - E_{TTF} - E_{TCNQ}$, is found to be -1.30 eV per cell. This energy reflects the interaction strength between TTF and TCNQ molecules, namely, the donor–acceptor interaction, together with the interaction through the H-bonds.

As explained before, we need to force commensurability in order to perform DFT calculations of the periodic system adsorbed on the Au(111) surface. The new unit cell, called C19, has been already described in Sec. 4.2. The relaxed structure of a commensurate TTF-TCNQ layer on a Au(111) surface, calculated from an initial guess based on the experimental model, is shown in Fig. 4.11c). It turns out that the molecular layer is bound to the gold surface mainly through TTF via two S–Au bonds per molecule, like in the case of isolated TTF, whereas TCNQ molecules interact weakly with the metal

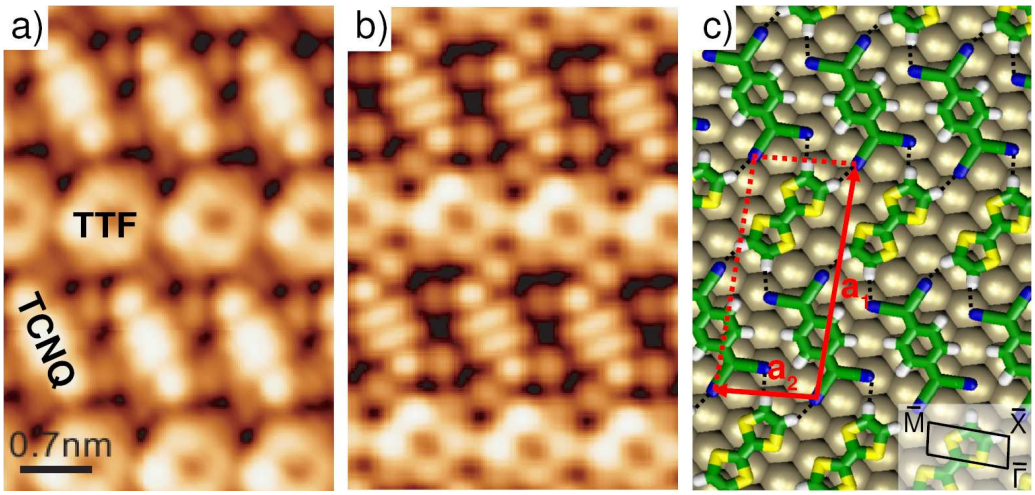

Figure 4.11: a) STM image with intramolecular resolution of the TTF-TCNQ mixed domain (V = 0.3 V; I = 0.4 nA)[a]. The molecular structure of TTF and TCNQ resembles the shape of the respective HOMO and LUMO. b) Simulated constant current STM image (V = 1.0 V) using the Tersoff-Hamann approach [45] on the DFT optimised geometry shown in c). c) The vectors a1 and a2 define the commensurate surface unit cell and the inset shows the corresponding SBZ[b].

[a] Data analysed using WSxM [138]

[b] The SBZ is defined by the points $\overline{\Gamma}$ = (0,0), $\overline{X}$ = (1/2,0), and $\overline{M}$ = (1/2, 1/2) in units of the reciprocal cell vectors. $\overline{\Gamma X}$ and $\overline{XM}$ correspond to the directions across and along the molecular rows, respectively.

surface. The geometric optimisation of such a large system is quite complex[9]. The results presented here are restricted to the most stable geometry obtained with 15 k-points (3×5×1 sampling). We find that TTF adsorbs slightly tilted with two S–Au bonds of $\sim$ 3.0 Å. The distance from TCNQ N atoms to nearest Au atoms is between $\sim$ 3.1 Å (on top) and 3.4 Å (bridge-fcc). 4 H-bonds, between TTF and TCNQ molecules, with lengths $\sim$ 2.3±0.1 Å are formed per cell, and 2 weaker H-bonds between TCNQ molecules that measure 2.6±0.1 Å. A Tersoff-Hamman [45] STM simulation at positive voltage of this stable geometry is shown in Fig. 4.11b). It can be seen the good agreement with the experimental STM image. The main features are reproduced.

Regarding the binding energy, as done previously for the pure TCNQ phase, we can also define two distinct binding energies. $E_{b1} = E_{Surf+Ads} - E_{2D} - E_{Surf}$, that shows the strength of the bonding with the surface, and $E_{b2} = E_{Surf+Ads} - E_{TTF} - E_{TCNQ} - E_{Surf}$, that also computes the binding due to the interaction between molecules. E_{b1} = -0.22±0.03 eV, and E_{b2} = -1.51±0.03 eV. Again, $E_{b2} - E_{b1}$ = -1.29 eV/cell is the binding energy between TTF and TCNQ molecules within the assembly, and it compares well with the stabilisation energy of the monolayer calculated without substrate (-1.30 eV/cell).

4.4 Electronic properties of the OM interface: TTF-TCNQ/Au(111)

The TTF-TCNQ molecular solid is an organic metal with a one-dimensional-like band structure due to the π stacking of each component, and to the transfer of $\sim$ 0.6 electrons from the donor π stacks (TTF) to the acceptor ones (TCNQ). Nonetheless, on the Au(111) surface the TTF-TCNQ layer has different electronic properties because both molecules lie parallel to the surface, as it has been just described. In this section, we present the distinct electronic characteristics of the TTF-TCNQ and Au(111) OM interface. First, the donor-acceptor character of the organic layer is addressed from a theoretical point of view, and then, the experimental STS measurements are presented, as well as their interpretation.

4.4.1 Theory: Donor-acceptor character

It is known that within the organic crystal a charge transfer from the donor rows to the acceptor rows exists. What happens within the planar thin film? Is the donor-acceptor character maintained? To investigate this, we computed PDOS on molecular orbitals [see

[9]It relaxes to different geometries depending on the number of k-points used, and depending on the starting point of relaxation.

Sec. 2.3.3], and evaluated the charge transfer by looking to induced electron densities [Sec. 2.3.2], and by a Bader charge analysis [Sec. 2.3.5].

- PDOS on MO

The role of molecular states during the thin film formation, and upon interaction with the substrate is extracted by projecting the DOS on TTF and TCNQ frontier orbitals, HOMO and LUMO [Fig. 4.12].

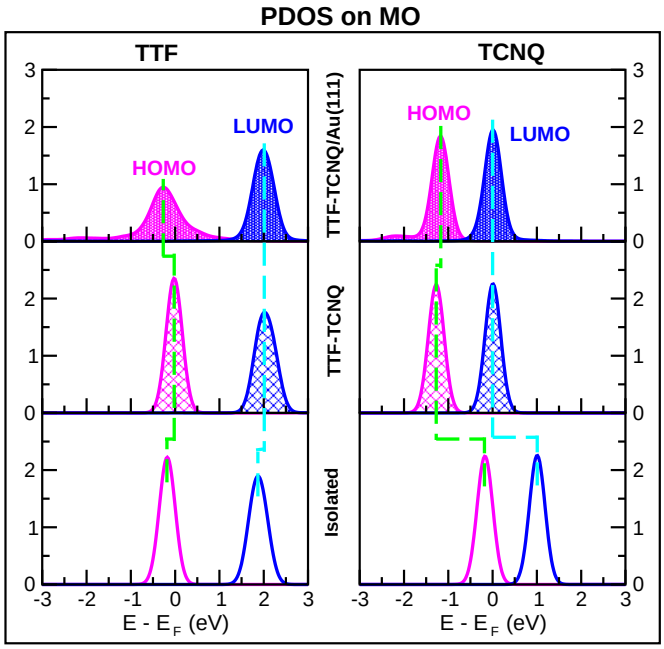

Figure 4.12: PDOS on TTF (left panel) and TCNQ (right panel) HOMO and LUMO orbitals. Upper panels depict PDOS of molecules adsorbed on Au(111), middle panels correspond to molecules within the free standing monolayer, and lower panels to isolated molecules. Dashed lines follow the peaks' shifts from one system to the other. A Gaussian broadening of 250 meV width is employed.

By looking to the PDOS on MO, we find that the donor/acceptor character of each component evidences when the planar thin film is formed. This is shown by the shifts of the molecular peaks when peaks' positions for isolated molecules and molecules within the TTF-TCNQ film are compared. TTF frontier orbitals show a tiny shift to the right (towards empty states) [see Fig. 4.12 low part on the left], while TCNQ peaks shift to the left (towards occupied states) [see Fig. 4.12 low part on the right]. Particularly, the HOMO of the TTF loses charge becoming partially unoccupied [pink peak in the middle panel centred at E_F], whereas the TCNQ LUMO gains charge becoming almost singly occupied [blue peak in the middle panel aligned with E_F]. Furthermore, this donor/acceptor character is maintained after overlayer adsorption on the metal surface [see Fig. 4.12 top part]. TCNQ's interaction with the surface is rather weak. This is revealed by PDOS peaks that keep their molecular character (the Lorentzian peak shape). However, the TTF HOMO suffers a notorious broadening as a consequence of its mixing with gold states [pink broad feature in the upper panel on the left]. Hence, the interaction of the TTF-TCNQ layer with Au(111) is essentially conducted by the TTF molecule.

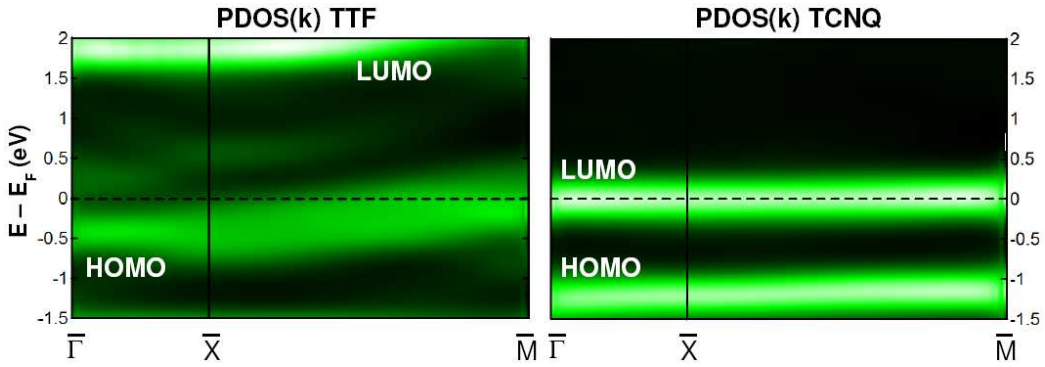

Figure 4.13: Wave vector (k) resolved PDOS on TTF (left panel) and TCNQ (right panel) HOMO and LUMO molecular orbitals along $\overline{\Gamma XM}$ [see Fig. 4.11 inset]. The PDOS colour map on TTF shows some complex structure arising between TTF HOMO and LUMO resonances.

The PDOS above E_F is rather dominated by the tail of the TTF HOMO broadened as a consequence of its hybridisation with metal states. We can explore more details about the nature of this interaction by resolving the PDOS on MO versus the electron momentum along main directions of the molecular SBZ, $\overline{\Gamma X}$ and $\overline{XM}$. As shown in Fig. 4.11c), the vectors that define the unit cell, a_1 and a_2, are almost perpendicular, and thus the vectors that define the corresponding reciprocal unit cell are also almost perpendicular. The a_2 vector goes along the molecular rows, while a_1 goes across the rows. Then, if b_1 and b_2 are the reciprocal cell vectors, b_2 results almost parallel to the molecular rows, whereas b_1 is perpendicular to the rows. The SBZ is defined by the points $\overline{\Gamma}$= (0,0), $\overline{X}$= (1/2,0), and $\overline{M}$= (1/2,1/2) in units of the reciprocal cell vectors. Therefore, the $\overline{\Gamma X}$ and $\overline{XM}$ correspond to the directions across and along the molecular rows, respectively.

Fig. 4.13 depicts maps of the PDOS resolved in k-space, given by Eq. [2.26], that adds the contribution of HOMO-1, HOMO, LUMO and LUMO+1 orbitals, for TTF and TCNQ upon adsorption on Au(111). It reveals the existence of two distinct features in the energy region between TTF HOMO and LUMO states (E - E_F $\in$ 0–2 eV). These features are evidence of a more complex substructure hidden behind the broad TTF HOMO resonance. Fig. 4.13 gives information about the dispersive behaviour of the resonances too. PDOS on TTF shows some dependence with the k vector, while PDOS on TCNQ presents no dispersion along the SBZ.

- Charge transfer: Induced density & Bader analysis

The induced electron density (ρ_{ind}) corroborates the donor/acceptor character of the system, and the charge transfer from TTF to TCNQ, deduced from PDOS. Fig. 4.14 shows 3D plots of the ρ_{ind}, for the free standing monolayer [4.14a) top view], and for the TTF-TCNQ on Au(111) [4.14b) & 4.14c) top views, and 4.14d) side view]. It can be seen in

Fig. 4.14a), that when the monolayer is formed a charge accumulation [blue areas] located on TCNQ molecules is induced. In addition, the distribution of this charge density is similar to the shape of the TCNQ LUMO [see Fig. 4.6c)]. On the contrary, there is a charge depletion [pink areas] centred at TTF molecules with the appearance, in part, of the TTF HOMO[10] [see Fig. 4.5c)]. TTF loses charge that is accepted by the TCNQ.

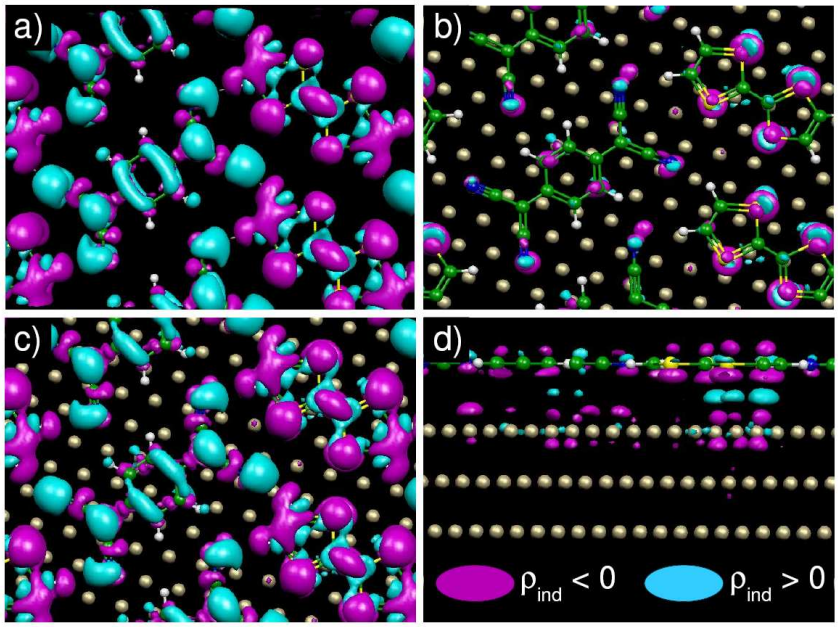

Figure 4.14: Induced electron density: a) $\rho_{\text{ind}} = \rho(TTF-TCNQ) - \rho(TTF) - \rho(TCNQ)$ of TTF-TCNQ monolayer. b) $\rho_{\text{ind}_1} = \rho(TTF-TCNQ/Au) - \rho(Au) - \rho(TTF-TCNQ)$ for the mixed system on Au(111) showing the effect produced by the substrate onto the monolayer, top view and d) side view. c) Induced total electron density, $\rho_{\text{ind}_2} = \rho(TTF-TCNQ/Au) - \rho(Au) - \rho(TTF) - \rho(TCNQ)$ for TTF-TCNQ on Au(111) that also shows the effect due to the interaction between the molecules[a]. Pink areas represent negative values of the induced density and blue areas positive values.

[a]Data belong to the planar molecular layer kept at 3.2 Å from the substrate, without further vertical relaxations.

As far as the mixed TTF-TCNQ phase on Au(111) is concerned, we can separately look for the effect produced by the substrate on the monolayer, ρ_{ind_1} [Fig. 4.14b) & 4.14d)], or the induced total electron density, ρ_{ind_2}, depicted in Fig. 4.14c), that also includes the interaction between the molecules. This interaction is dominated by the charge transfer from TTF to TCNQ, like for the free monolayer (notice the great likeness of both figures). The interaction with the surface though, is mainly driven by the TTF molecule, leaving the TCNQ almost unperturbed. The charge accumulation located halfway the S–Au bond seen in Fig. 4.14d) shows the covalent character of that bond. Hence, TTF chemisorbs on the Au(111) surface, in the same manner as the isolated TTF does [see Sec. 4.3.1].

[10]Actually, it shows a combination of more than one occupied state.

PDOS and induced electron density analysis, give qualitative results proving that the TTF/TCNQ donor/acceptor character is kept upon adsorption on the metallic surface, and that the TCNQ–Surface interaction is weak, while TTF interacts and mixes strongly with gold. For quantitative evaluation of the charge transfer between components, next, we perform a Bader charge analysis. Table 4.2 summarises the results. Within the free

Table 4.2: Bader charge analysis: $\Delta q = q - q_{Isol}$ is the charge difference of a given component as compared with its corresponding charge when isolated. The unit is number of electrons (e^-).

System	$\Delta q(TTF)$	$\Delta q(TCNQ)$	$\Delta q(Substrate)$
TTF-TCNQ	-0.61	+0.61	-
TTF-TCNQ/Au(111)	-0.67	+0.72	-0.05
TTF-TCNQ/Au(111)-H	-0.62	+0.77	-0.15

monolayer the charge transfer accounts ~ 0.6 e^-, that agrees with the transfer within the bulk. For the adsorbed monolayer, despite the differences using H passivated or non-passivated surface, TCNQ gains ~ 0.7 e^-, thanks to some charge transfer from the substrate too.

4.4.2 STS measurements

Scanning tunneling spectroscopy (STS) measurements reveal that the electronic structure of the TTF-TCNQ/Au(111) interface cannot be simply understood within a conventional picture of molecular level alignment [147]. Fig. 4.15a) & 4.15b) compares the differential conductance (dI/dV) spectra of TCNQ embedded in a pure TCNQ island with that of the molecule within the mixed TTF-TCNQ phase. Pure TCNQ islands show a broad resonance at 0.7 V associated to the LUMO, and the shift of the Au(111) surface state's onset. These two fingerprint change on the TTF-TCNQ mixed domains. The broad LUMO resonance on pure TCNQ islands [Fig. 4.15a) blue curve] contrasts with a sharp peak observed at 0.3 V on TCNQ rows in the mixed domains [IS1 in Fig. 4.15b) green curve]. The characteristic spectrum taken on top of a TTF molecule shows another feature at 0.8 V [IS2 in Fig. 4.15b) red curve]. In addition, the distinctive onset of the Au(111) SS is not observed in the TTF-TCNQ layer.

A more complete picture of the spatial localisation of IS1 and IS2 resonances of the mixed phase is provided by mapping dI/dV spectra along given directions of the molecular layer [Fig. 4.15d) & 4.15e)]. Fig. 4.15c) shows an STM image of a boundary between a pure TCNQ island, and a mixed TTF-TCNQ phase. There are marked two main directions,

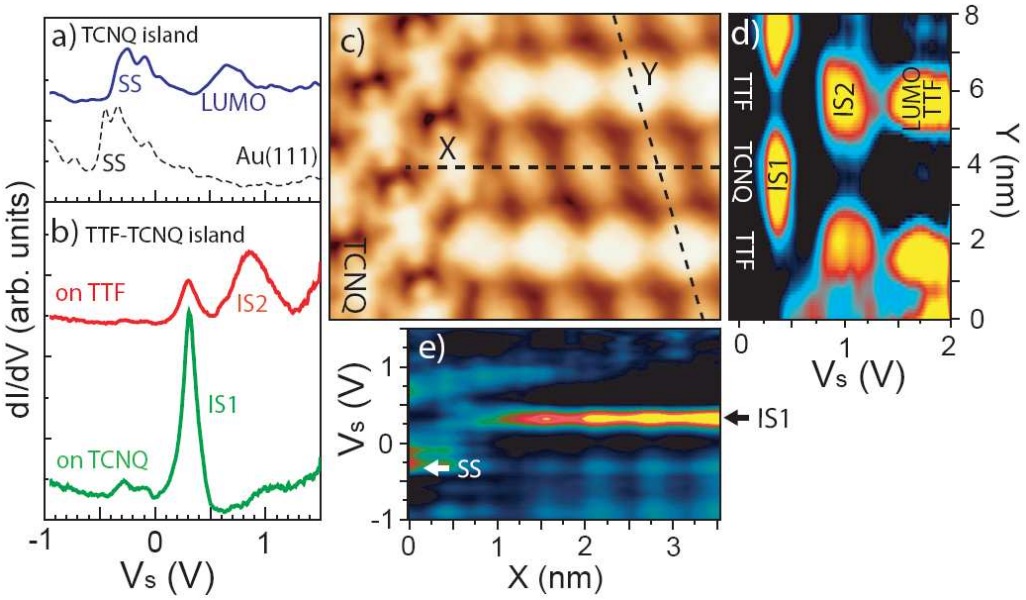

Figure 4.15: Comparison of dI/dV spectra of a) TCNQ pure islands [spectrum taken on a nearby clean Au(111) region shown for comparison] and b) TTF and TCNQ in mixed TTF-TCNQ islands. d) & e) The differential conductance spectra is mapped along the dashed lines shown in the STM image c) (V = 1.9 V, I = 0.07 nA). The maps clearly show the spatial localisation of IS1 and IS2 features on TCNQ and TTF rows, respectively.

across the molecular rows (Y dashed line, crossing TTF and TCNQ molecules) and along the TCNQ rows (X dashed line, crossing the domain boundary).

The collection of spectra taken along Y [Fig. 4.15d)] reveals that IS1 and IS2 features are spatially separated: IS1 has a stronger signal on the TCNQ rows, while IS2 is localised on the TTF rows. It also shows another resonance on TTF molecules at 1.7 V, which corresponds to the signal of the first unoccupied molecular orbital, LUMO of the TTF molecule, as reported for isolated TTF on Au(111) [139]. This already suggests that the origin of these peaks (IS1 & IS2) cannot be directly assigned to resonant tunneling through molecular states. If we recall the calculated PDOS [see Fig. 4.12], this suggestion is further confirmed. There, calculated TTF LUMO lies around 2 eV, and there is no other molecular peak, neither from the TTF nor from the TCNQ, down to the E_F. However, the two features from the experiments appear just in that energy range (IS1 at 0.3 eV and IS2 at 0.8 eV). This range corresponds to that of the hidden features revealed by PDOS(k) plots in Fig. 4.13.

Spectra along X direction [Fig. 4.15e)], that start (from right to left) on TCNQ rows within the mixed phase and ends within the TCNQ pure island, corroborate the strong spatial localisation of the IS1 peak within the TCNQ rows. In addition, the IS1 signal vanishes as we enter the pure island. When the STM tip is located at the domain boundary, the TCNQ LUMO and shifted SS signals appear.

Therefore, the chemisorption of the TTF-TCNQ layer distorts the electronic structure of the Au(111) surface, causing additional features to appear in the unoccupied LDOS. The DFT results substantiate that the origin of the features IS1 and IS2 in the experimental data cannot be simply ascribed to specific molecular orbitals. Thus, they must be a new fingerprint of some interaction between the organic layer and the metal surface.

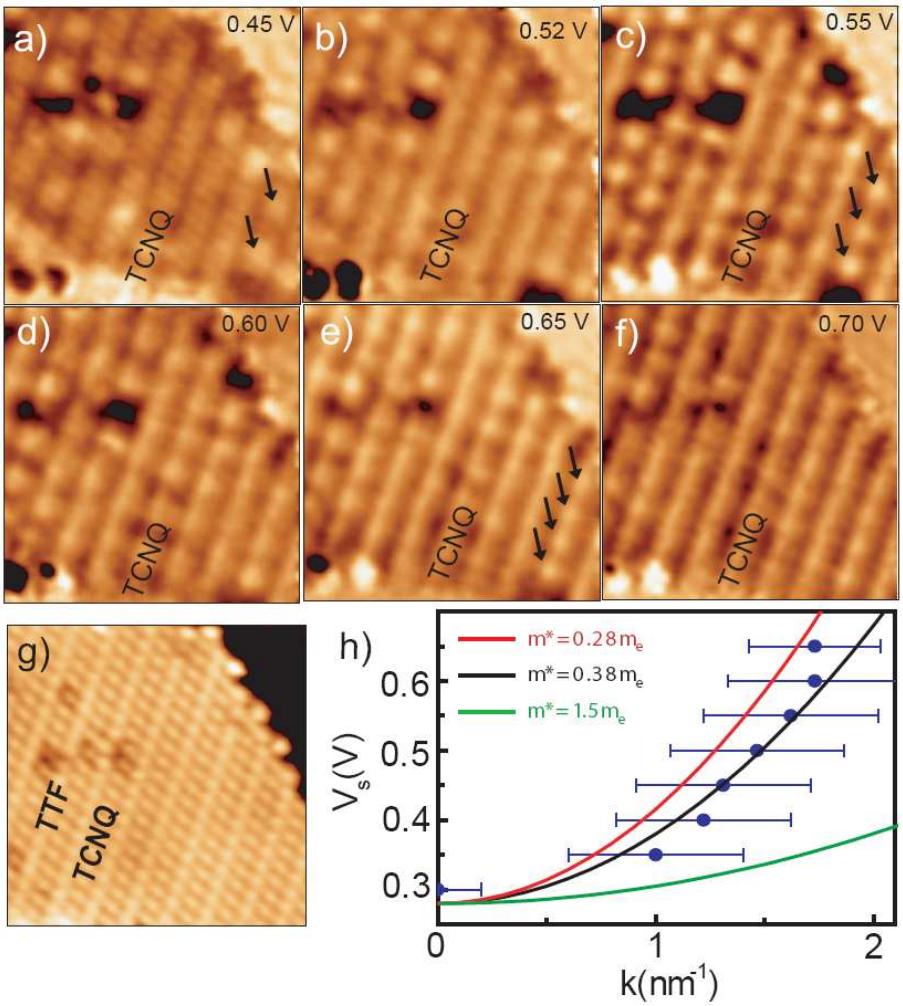

Figure 4.16: a)–f) are dI/dV maps of a TTF-TCNQ island at the indicated sample bias values above the onset of the IS1 resonance (I = 1.0 nA; 16×16 nm^2). The corresponding STM image is shown in g). h) Dispersion relation $E(k)$ obtained after FFT analysis. Black line is a parabolic fit to the data points. Red and green curves are shown for comparison with the dispersion obtained in a metal surface state and a metalorganic compound, respectively.

A hint about the origin of experimental IS1 and IS2 resonances is the dispersive behaviour of IS1. dI/dV maps taken at energies just above the energy of this peak exhibit an oscillatory pattern centred at the TCNQ rows [Fig. 4.16a)–4.16f)]. The periodicity of this oscillation is larger than the molecular corrugation (intermolecular distance) and changes with the bias voltage (V_s). This is a distinctive characteristic of (in-plane) quantum interference of electron states with energy eV_s [148]. Furthermore, these oscillations

are characteristic of a quasi-one dimensional electron band, since they are only observed dispersing along the TCNQ rows. It is in analogy with the case of a particle in a box.

Defects and island boundaries act as scattering centres, forming destructive and constructive interference patterns. According to energy quantisation of a particle in a one-dimensional box, only those rows with the appropriate length will show an oscillation for a certain energy. The arrows in Fig. 4.16a)–4.16f) mark the different number of maxima depending on the bias voltage (energy).

In Fig. 4.16h) the wavelength of the oscillation versus the bias voltage is plotted. We find that it follows a parabolic dispersion relation:

$$E(k) = E_0 + \hbar^2 k^2 / 2m^*, \tag{4.1}$$

where E_0 is the binding energy of the band and m^* is the effective mass. The fitting results in $m^* = (0.38 \pm 0.05)m_e$ and $E_0 = 0.28 \pm 0.02$ eV above the Fermi energy. Electronic bands of molecular solids exhibit effective masses larger than $1m_e$ [125–127]. In contrast, as shown in the figure, the dispersion found here has a a quasi-metallic character. Its value is closer to the m^* of electrons that belong to a metal surface state ($m^* = 0.26m_e$ for a Au(111) surface [149]), than to electrons from a pure molecular conductor ($m^* = 1.5m_e$). This indicates that the IS1 feature has to be related to the underlying metal states [119, 150].

4.5 TTF-TCNQ/Au(111) band structure: Interface bands

To decipher the role of the metal surface, the calculated band structure of TTF-TCNQ adsorbed on Au(111), shown in Fig. 4.17, is analysed. We focus on the $\overline{\Gamma X}$ and $\overline{XM}$ directions, i.e., across and along molecular rows, respectively [see Fig. 4.11c)].

By looking at the spatial charge density distribution through the k-space, we track the states with a significant fraction of charge located at the organic/metal interface; that is, states that have contribution from the metal surface state. Colour dots mark them in the band plot. We find out that there are two interface bands dispersing away from the $\overline{X}$ point. A lower band [marked in green], that shows dispersion only along the molecular rows, and a higher one [marked in red], that exhibits a two-dimensional anisotropic dispersion. The dispersion along the rows ($\overline{XM}$) can be fitted with a parabola [dashed lines in Fig. 4.17], like it was done in the experiment. It results in low effective mass values, $0.54m_e$ and $0.44m_e$ for the red and green band, respectively. Thus, both interface bands have metal-like dispersion.

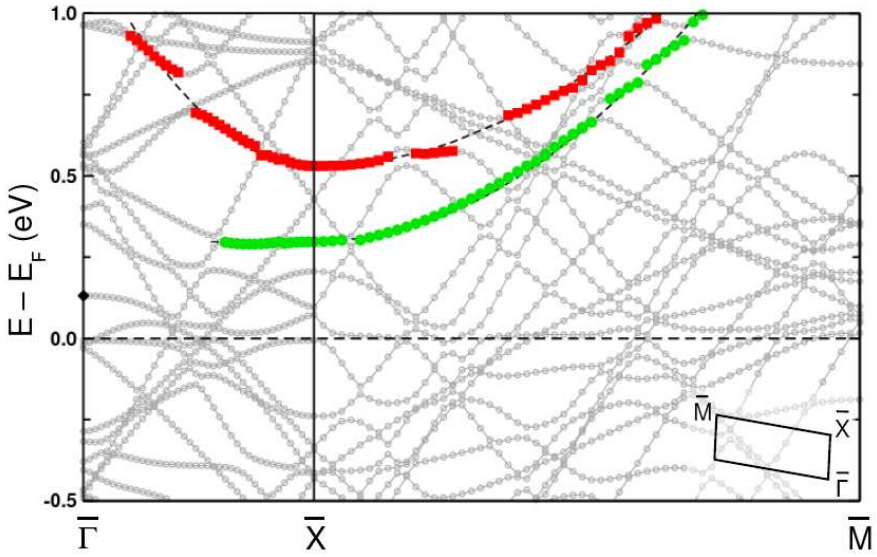

Figure 4.17: Calculated band structure of the TTF-TCNQ/Au(111) system along $\overline{\Gamma XM}$ directions. Green (●) and red (■) dots mark states with charge at the interface. Dashed lines along $\overline{XM}$ show the parabolic fit of the data, giving $m^* = 0.44m_e$ for the green, and $m^* = 0.54m_e$ for the red. Inset depicts the SBZ of the system.

4.5.1 Simple model: Weak periodic potential

The formation of these two interface bands can be partially understood with the help of a simple model [151] of quasi-free electrons in a weak periodic potential along one surface direction. It is known, that any change in the periodicity of a system implies folding of the bands, and that a weak coupling opens gaps at the SBZ boundary, giving rise to states with different symmetry, odd and even states, as sketched in Fig. 4.18.

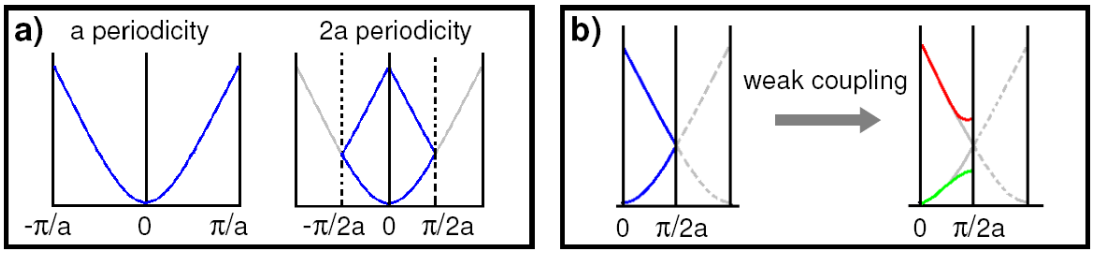

Figure 4.18: a) Sketch of the band folding imposed by a new periodicity. b) Gap opening at the SBZ boundary due to a weak coupling.

Therefore, (i) the charge re-distribution induced by the TTF-TCNQ organic layer modulates the potential of the Au(111) surface along the $\overline{\Gamma X}$ direction with a new periodicity that folds the surface and bulk bands of the metal [see Fig. I.5 in Appendix I], and (ii) the coupling with the overlayer opens gaps at the SBZ boundary ($\overline{X}$ point) giving rise to the upper (red band) and lower (green band) split bands found in the band structure [Fig. 4.17].

4.5.2 Hybrid character of interface bands

This simple model explains part of the story, but the complexity of the system requires a thorough analysis. At the TTF-TCNQ and Au interface, there exists some interaction between the folded metal states and the molecular orbitals. Among all the metal states the main role is played by the Au(111) surface state [blue dots in Fig. 4.19a)]. It interacts effectively with the HOMO of the TTF [pink dots in Fig. 4.19a)] whose energy is close to the minimum of the SS. It is their interaction what generates the two interface bands [red and green]. The SS shifts up and splits at the boundary, while TTF HOMO shifts down

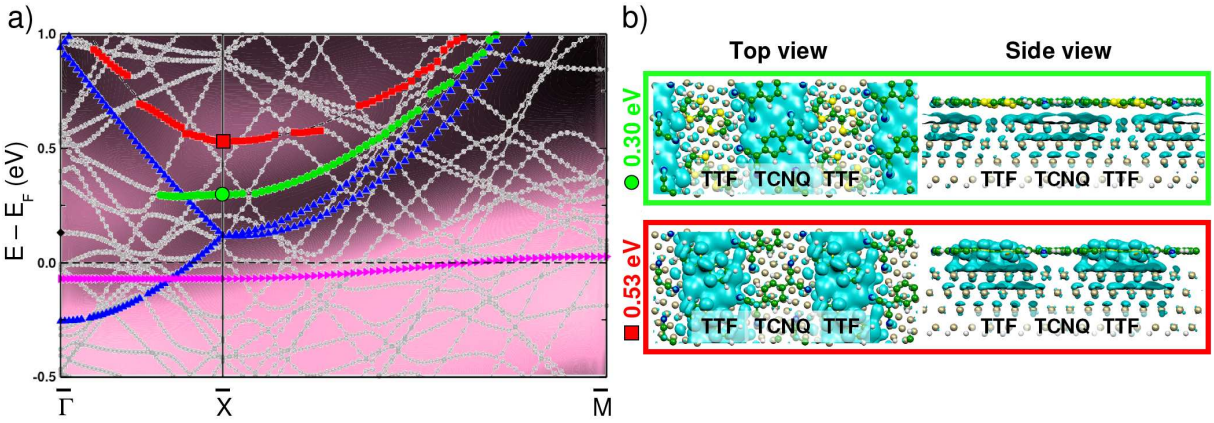

Figure 4.19: a) Combination of the calculated band structure and the PDOS(k) on TTF HOMO to unravel the hybrid character of the interface bands. The blue bands (▲) correspond to the bare Au(111) surface state, and the pink band (►) is the HOMO of the TTF within the free monolayer. b) Constant charge density isosurfaces for two characteristic states located at the $\overline{\text{X}}$ point, showing a selective mixing with TTF.

hybridising strongly with metal states. This shift and the strong mixing are evidenced by the PDOS resolved in electron momentum, shown now as a colour map underneath the band plot in Fig. 4.19a). Pink shadow areas represent states with some weight on the TTF HOMO. There is a main contribution below the Fermi level, as well as two features above E_F: one close to $\overline{\Gamma}$ at $\sim$ 0.1–0.4 eV, and another one dispersing away from $\overline{\text{X}}$ at $\sim$ 0.5 eV. This latter feature coincides with the minimum of the red band.

The hybrid character of the interface bands originates from a mixture of folded bulk and surface metal states with TTF states. The most interesting evidence of a selective mixing of molecular states with the Au(111) SS is found in the partial charge density plots of the bands at the $\overline{\text{X}}$ point [Fig. 4.19b)]. The lower state (at 0.3 eV) is located underneath the TCNQ rows, and has no molecular character [Fig. 4.19b) upper panel]. This is in accord with TCNQ states not contributing to the hybrid band. Furthermore, the symmetry of the state prevents it from mixing with TTF, and leaves it as the pure SS but modulated by the new periodicity imposed by the overlayer. On the contrary, the higher state (at 0.53 eV) appears centred at the TTF rows and has considerable weight on

the TTF HOMO [Fig. 4.19b) lower panel]. As regards the spatial distribution of charge, we can say that the lower and upper states at $\overline{\mathrm{X}}$, are the odd and even states with respect to the TTF rows.

Fig. 4.19a) also shows how the hybrid character of the bands changes along the SBZ. As the bands disperse away from E_F, they both lose molecular weight and essentially recover the character of the corresponding SS branches. For the lower band (green), coupling with the TTF HOMO and folded metal states introduces such a broadening close to the $\overline{\Gamma}$ point that it becomes a surface resonance. That is the reason why the green flat band cannot be followed down to $\overline{\Gamma}$.

The different adsorption properties of TTF and TCNQ on the surface produces a one-dimensional potential lattice across the molecular rows. The system draws an analogy to a Kronig-Penney model [151], as sketched in Fig. 4.20. The chemisorption of TTF (charge at S–Au bonds) would result in a periodic potential along the $\overline{\Gamma\mathrm{X}}$ direction. This potential would be zero at TCNQ sites, since TCNQ molecule does not interact with the surface. The two wavefunctions that solve the model at $\overline{\mathrm{X}}$ are our two split (red and green) interface bands. One solution locates charge above the TTF rows and the other on the TCNQ rows [137].

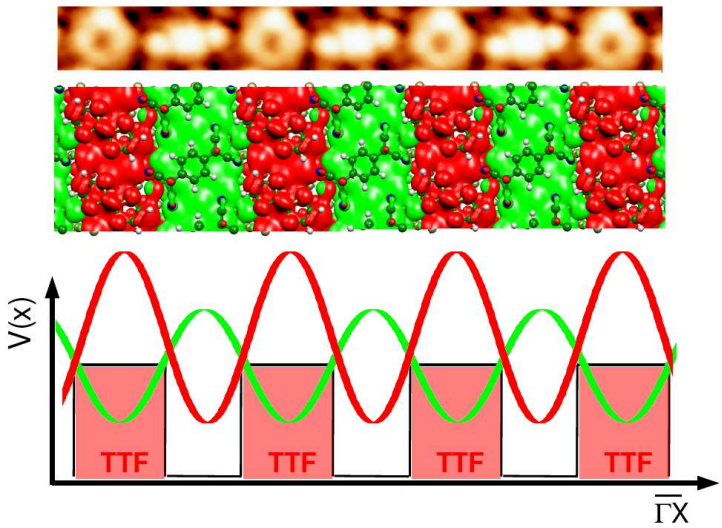

Figure 4.20: Analogy of the TTF-TCNQ/Au(111) system with a one-dimensional Kronig-Penney model. The different adsorption of the molecules generates a potential superlattice along $\overline{\Gamma\mathrm{X}}$ direction.

In conclusion, depending on where in the Brillouin zone we are, the problem can be described with the following 4×4 or 5×5 Hamiltonians:

- At $\overline{\Gamma}$; there is one SS that couples with TTF (HOMO), while TCNQ does not interact with Au. However, to fully described the system, it is necessary to include

at least one Au bulk state that also mixes with TTF:

$$\begin{pmatrix} E_{SS} & 0 & \Delta_s & 0 \\ 0 & E_b & \Delta_b & 0 \\ \Delta_s & \Delta_b & E_{TTF} & 0 \\ 0 & 0 & 0 & E_{TCNQ} \end{pmatrix} \tag{4.2}$$

where Δ_s and Δ_b are the couplings of TTF with Au SS and Au bulk, respectively. By comparison, the rest of the couplings are negligible ($\Delta_{Hb} << \Delta_s, \Delta_b$). Therefore, it results in the TCNQ LUMO close to E_F (at $\sim$ -0.01 eV), and three new states: (i) mainly TTF HOMO and bulk (with some SS) at $\sim$ -0.29 eV, (ii) mainly TTF and SS (with some bulk) at +0.13 eV [marked as a black dot (♦) in Fig. 4.19a], and (iii) mainly TTF and bulk (with some SS) at $\sim$ +0.40 eV.

- At $\overline{\text{X}}$; a 5×5 Hamiltonian is needed to describe the essence of the problem. There are two surface states, gerade (even) and ungerade (odd), two molecular orbitals (TTF HOMO and TCNQ LUMO), and one Au bulk state:

$$\begin{pmatrix} E^g_{SS} & 0 & 0 & \Delta^g_s & 0 \\ 0 & E^u_{SS} & 0 & 0 & 0 \\ 0 & 0 & E_b & \Delta_b & 0 \\ \Delta^g_s & 0 & \Delta_b & E_{TTF} & 0 \\ 0 & 0 & 0 & 0 & E_{TCNQ} \end{pmatrix} \tag{4.3}$$

where Δ^g_s and Δ_b are the couplings between TTF and Au gerade-SS, and TTF and Au bulk, respectively. By comparison, the rest of the couplings are negligible ($\Delta_{Hb} << \Delta^g_s, \Delta_b$). The resulting states are: (i) the TCNQ LUMO at $\sim$ -0.01 eV, (ii) the state at +0.30 eV [marked in green in Fig. 4.19], that has been shown to be essentially the ungerade-SS, (iii) the state at +0.53 eV [marked in red in Fig. 4.19], which is a mixture of TTF HOMO and the gerade-SS, and (iv) two more states located at $\sim$ -0.55 eV and $\sim$ -0.24 eV, formed by a mixture of TTF and Au bulk (with some gerade-SS)[11].

- At $\overline{\text{M}}$; the coupling between the MOs and the two SS branches is very weak. Then, the TTF-TCNQ coupling is not neglible:

$$\begin{pmatrix} E^g_{SS} & 0 & 0 & 0 \\ 0 & E^u_{SS} & 0 & 0 \\ 0 & 0 & E_{TTF} & \Delta_{Hb} \\ 0 & 0 & \Delta_{Hb} & E_{TCNQ} \end{pmatrix} \tag{4.4}$$

[11] It is known from their charge distribution, that is not shown here.

where Δ_{Hb} is the coupling between TTF HOMO and TCNQ LUMO through the H-bonds. It gives rise to the bonding (at $\sim$ -0.01 eV) and antibonding (at $\sim$ + 0.06 eV) states. Furthermore, there are the gerade-SS and ungerade-SS branches at +1.45 and +1.39 eV, respectively[12].

The different couplings (Δ) are the parameters to be adjusted in order to reproduce the energy levels found in the *ab-initio* calculations. They would quantify the strength of the different interactions in the system.

4.5.3 Theory/Experiment agreement: Peak identification

Based on theoretical results we can now associate the two observed peaks in the dI/dV spectra [IS1 and IS2, presented in Sec. 4.4.2] with the two calculated OM interface hybrid bands: IS1 with the lower (green) band and IS2 with the higher (red) one [Fig. 4.21].

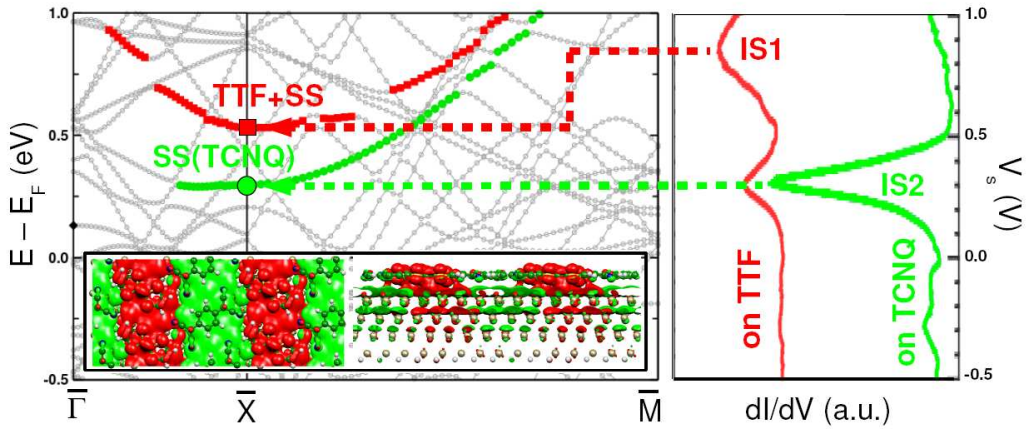

Figure 4.21: Comparison between DFT and experimental results. Theory explains the observed spatial localisation and the lineshape (due to different dispersive behaviour) of IS1 and IS2 resonances.

The calculated spatial partial charge density maps at $\overline{\mathrm{X}}$ are in good agreement with the spatial localisation of the experimental peaks found in the dI/dV profiles: IS1 located on TCNQ rows and IS2 on TTF rows [see Fig. 4.15d)]. Hence, the peak structure in the STS spectra is mostly originated from band states lying close to the $\overline{\mathrm{X}}$ point, because only at this region of the SBZ they are purely localised at the interface (close to $\overline{\Gamma}$ there is mixing with Au bulk states). The lower band is fairly flat across the rows ($\overline{\Gamma\mathrm{X}}$) and disperses parallel to the TCNQ rows ($\overline{\mathrm{XM}}$) in agreement with the one-dimensional dispersion and sharp lineshape of the peak IS1. IS2 appears as a broader peak in the experimental dI/dV spectra in consistency with the two-dimensional anisotropic dispersion of the higher band.

[12]These states are out of range in the depicted band plots.

From the quantitative point of view, the energy position of the IS1 peak agrees with the energy of the green band at $\overline{\mathrm{X}}$. Furthermore, the effective mass value deduced from the conductance maps ($m^* = 0.38m_e$) is also in good agreement with the theoretical dispersion ($m^* = 0.44m_e$). However, the energy of IS2 is not so well described in the theory, that yields an energy closer to E_F than it should. The fact that the penetration of the SS into the bulk cannot be correctly described using a slab made only by four Au layers [see Appendix I], may well explain this discrepancy. In any case, we believe that our description of the SS is correct enough to derive qualitative trustable conclusions, as done in this chapter.

4.6 Conclusions

In this chapter we have characterised, the isolated adsorption of TTF, an electron donor, and TCNQ, an electron acceptor, molecules, and their co-adsorption on Au(111), both structurally and electronically. First, we have shown that pure TTF chemisorbs tilted with covalent S–Au bonds, while TCNQ self-assembles in well ordered islands that interact weakly with the surface. In this case, we have also shown that upon adsorption of the molecular layer there is a shift of the onset of the Au(111) surface state.

Regarding the co-adsorption of both types of molecules, they formed a charge-transfer complex that lies flat on the surface. It gives rise to a mixed phase made of alternating TTF and TCNQ rows. We have shown that the experimental conductance spectrum consists in two fingerprints: one sharp peak localised on the TCNQ rows that disperses along the rows, and a broader peak centred at the TTF rows. DFT calculations allow to understand the origin of these peaks, proving that the TTF-TCNQ/Au(111) system has a characteristic interface band structure. While TCNQ is essentially unperturbed by the underlying surface, TTF hybridises with the Au(111) surface, that is, there is a selective mixing. This distinct coupling creates a weak periodic potential across molecular rows, and yields the formation of two interface bands with both molecular and metal character. The bands exhibit a free-electron metal-like dispersion and the anisotropic structure of the molecular layer, and have been associated to the observed spectroscopic fingerprints. It has been also suggested that simple Hamiltonians can be used to model the system.

On the whole, our results suggest that tuning the strength of donor–metal interaction or spacing between the TTF rows may allow to engineer the organic-inorganic interface band structure and, hence, the functionality of the molecular thin film.

Chapter 5

Self-assembly of complementary polyarenes on Au surfaces

In this chapter the adsorption of naphtalene tetracarboxylic diimide (NTCDI, $C_{14}H_6N_2O_4$) and 1,4-bis(4,6-diamino-1,2,5-triazin-2-yl)benzene (BDG, $C_{12}H_{12}N_{10}$) on Au single crystals is addressed. NTCDI and BDG are planar organic molecules with extended π-systems, that contain complementary amine and imide functional end groups. The chapter starts with a brief introduction to supramolecular self-assembly, and its use to create nanostructured templates and functionalised surfaces. NTCDI and BDG molecules are both individually adsorbed and co-deposited on the flat Au(111) surface. The resulting assemblies are investigated by means of STM measurements and theoretical calculations in the following section. The chapter continues presenting some results of the co-adsorption of NTCDI and BDG on the faceted Au(455) vicinal surface. The next section is devoted to the spectroscopic characterisation of the signature of the amine and imide functional end groups. There, theory and different experimental techniques are combined. Finally, there is a concluding section that summarises the results.

5.1 Introduction

Molecular recognition, that is, selective molecular interaction, is at the basis of fundamental biological processes in living systems (DNA replication, virus attachment to cells, etc.), as well as the driving force in supramolecular self-assembly. Supramolecular chemistry aims at developing complex self-organised systems made of molecular building blocks linked by relatively weak non-covalent interactions (mainly hydrogen bonds and metal–ligand interactions) [8, 9]. Synthetic chemistry allows access to a wide variety of functionally and structurally diverse building blocks that through their interactions lead to a vast range of supramolecular architectures with tailor-made properties. Such networks

can provide different nanostructured templates and functionalised surfaces for nanotechnology applications, such as high-density magnetic media, nanoparticle functionalisation for molecule and cell targeting, or organic molecular multilayer growth [152].

In particular, the self-assembly of two-dimensional (2D) supramolecular structures on solid surfaces has important implications in both basic science and nanotechnology. Surface sensitive techniques, such as STM, permit visualisation and manipulation of matter at the atomic level. Therefore, it can be exploited together with molecular recognition strategies, in the fabrication of nanostructured templates on solid surfaces. This is the so-called "bottom-up" approach to nanofabrication, which promises to revolutionise future device miniaturisation [5–7].

On going from the 3D supramolecular chemistry to the 2D supramolecular assembly, the substrate is a key issue. The influence of the electronic structure, or the topological features of the substrate may be determinant in the molecular arrangements. As the substrate enters into play, it can be used as a tool for steering the self-assembly through the choice of templates with appropriate symmetry, surface patterns or chemical functions. Thus, towards tailoring and controlling supramolecular structures, not only one needs to understand intermolecular interactions, but also the interactions between the adsorbates and the substrate. This is still a scientific challenge. Within the surface approach, the STM analysis allows one to determine the molecule orientation and conformation, but the underlying interactions must be revealed with in-situ spectroscopic techniques. Theoretical calculations are a powerful tool to help in the interpretation of experiments.

To ensure emergence of 2D supramolecular order, balanced molecule–molecule and surface–molecule interactions are required. For such purposes, planar ring systems (polyarenes) are very suitable, particularly with noble metals as substrates, since they adsorb flat and at $T \neq 0$ K, diffuse quickly on the surface plane. This allows functional groups at the molecular periphery to approach easily each other and form non-covalent bonds. In particular, stable supramolecular structures can be obtained by co-adsorbing two molecules with complementary end groups, such as pair of DNA bases [153]. Synthetic chemistry offers the possibility of tuning the size of polyarenes and their symmetry, by inserting functional groups in the appropriate geometry. One good example is the co-adsorption of diamino-triazine (melamine) and perylene tetracarboxylic diimide (PTCDI) [154, 155]. It leads to a supramolecular (H-bonded) honeycomb network driven by both the strong PTCDI–melamine (imide–amine) affinity and the threefold symmetry of the melamine. The complementary amine and imide end groups are frequently chosen to achieve self-organisation of binary organic monolayers [156–160]. By selecting linearly shaped polyarenes with imide/amine end groups, one obtains the 1D analogue heterogeneous molecular network, made of 1D binary chains with strong intermolecular H-bonding.

As noted before, the substrate plays a key role in steering the 2D non-covalent bonding. Assembled patterns spanning large surface areas are effectively limited by terrace morphologies and substrate reconstructions domains [161]. Mesoscopic order can be achieved by self-assembled prepatterned surfaces, such as vicinal surfaces. A vicinal surface is formed by a periodic set of terraces of a crystal surface, that is, 1D arrays of monoatomic steps [162]. The vicinal surface introduces the uniaxial anisotropy in the system, and it can also induce single domains in the mesoscopic scale [163]. Furthermore, one can combine vicinal substrates and a pair of linearly shaped molecules with complementary end groups to achieve self-organised supramolecular assemblies with a well-defined uniaxial anisotropy with respect to a surface direction, namely, the step direction [159, 160].

5.2 BDG and NTCDI adsorption on Au(111)

With the objective of testing the prepatterning-plus-self-assembly approach of binary structures, 1,4-bis(4,6-diamino-1,2,5-triazin-2-yl)benzene (BDG)[1], which is a linear version of melamine, and naphtalene tetracarboxylic diimide (NTCDI), similar to PTCDI, are used, as well as a Au(111) vicinal surface with periodic faceting. The atomic structure of these molecules is schematically shown in Fig. 5.1. The NTCDI and BDG molecules present n-type (acceptor) and p-type (donor) semiconducting properties, respectively [164]. The complementary functionalisation of NTCDI and BDG with imide and amine, respectively, is expected to favour the formation of dimers with strong triple H-bonds, as depicted in Fig. 5.1.

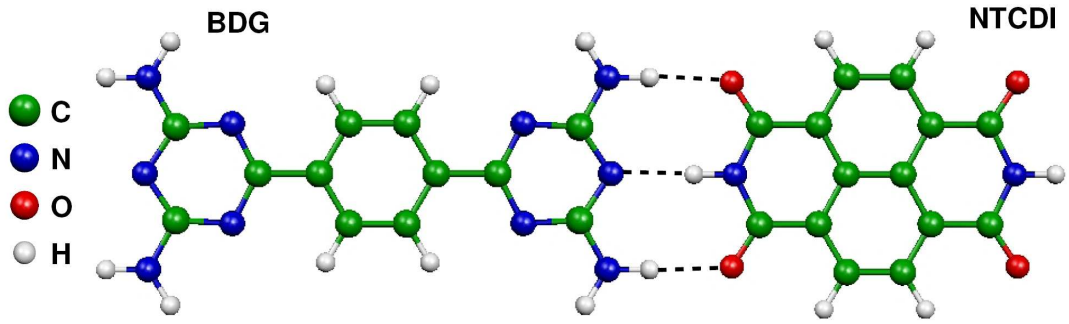

Figure 5.1: BDG and NTCDI molecule structures and formation of a dimer with strong triple H-bonds between the respective amine and imide terminations.

Before studying the co-adsorption of molecules on the vicinal surface, pure BDG and NTCDI, and 50 % mixed BDG + NTCDI 1 monolayer (ML) phases were first studied on

[1]BDG is synthesised by the reaction of dicyandiamide with terephthalonitrile in ethylene glycol monomethyl ether (EGME)/potassium hydroxide under microwave irradiation.

Au(111). The structural parameters observed with the STM are then compared to the geometries obtained from DFT calculations without including the substrate.

5.2.1 STM measurements and theoretical calculations: geometries

The STM experiments were performed at the Nanophysic Laboratory of the applied physics department from the EHU/UPV at Donostia (Spain). An ultrahigh vacuum system (base pressure below 5×10^{-11} mbar) equipped with a commercial Omicron STM that operates at 300 K was used. BDG and NTCDI were evaporated from effusion cells, and all surfaces were prepared by standard sputter-annealing cycles.

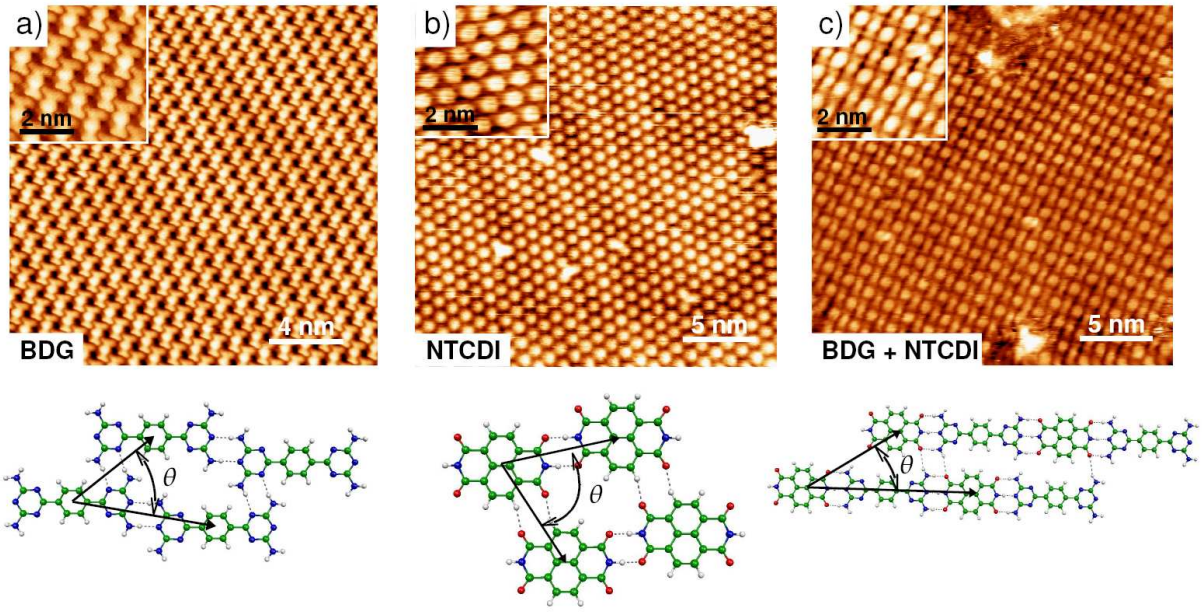

Figure 5.2: STM topographies showing monolayer-thick structures of a) BDG (V = -0.27 V, I = 0.045 nA), b) NTCDI (V = -1.6 V, I = 0.162 nA), and c) NTCDI-BDG (V = -0.6 V, I = 0.103 nA) on Au(111). At the bottom panels, theoretically calculated tetramer structures are shown, with the corresponding 2D lattice vectors.

The images in Fig. 5.2 show characteristic STM topographies for self-assembled monolayer structures of pure BDG [Fig 5.2a)], pure NTCDI [Fig 5.2b)] and the mixed phase [Fig 5.2c)] on Au(111). A smooth undulation related to the herringbone reconstruction of Au(111) is visible underneath the flat monolayer islands. This is an indication of a rather weak interaction between the molecules and the substrate. However, a residual molecule–substrate interaction remains, since the periodicity of the herringbone is slightly modified with respect to the uncovered surface [see Sec. 5.2.3 for details]. The interaction of these kind of planar molecules with the Au substrate is via their π-conjugated electron cloud, i.e., it is mainly a van der Waals interaction. A shortcoming of DFT is that it fails to

describe van der Waals forces. However, as the 2D self-assembly is driven by H-bonds, the experimental structural lattice parameters can be compared with DFT calculations of molecular assemblies without considering the Au surface. Furthermore, the Au(111) has a very low corrugation which means that the surface potential is very flat, and hence, is reasonable to compare calculations of the free standing monolayer with experimental structures on Au(111).

We carried out DFT based theoretical calculations to find out the most stable geometry of BDG, NTCDI and mixed BDG-NTCDI H-bond assemblies. First, using the Gaussian software suit [165], which uses a localised basis set of orbitals, the gas phase geometry of tetramers was elucidated at the polymer science and technology department of the EHU/UPV at Donostia. During the geometry optimisation, all rings were forced to be coplanar[2], but no other constrain was imposed. The respective relaxed structures are shown in the bottom panel of Fig. 5.2. Then, using a 2D periodic cell, based on previous calculations, the 2D periodic geometry was also calculated using the VASP package [32,33] within the PAW method [35] to treat electron–ion interactions, and the GGA (PW91 [30]) for exchange and correlation. During the relaxation, every atom within the free standing monolayer (10 Å of vaccum in the vertical direction) was allowed to move in the three directions until all forces were smaller than 0.01 eV/Å.

Table 5.1: Experimentally measured and theoretically calculated lattice parameters for the pure BDG, pure NTCDI and mixture of BDG-NTCDI assemblies.

	Exp.	**Tetramers**	**2D periodic cell**
BDG	13.4 Å × 11.4 Å $\theta \sim 47.3°$	14.4 Å × 10.3 Å $\theta \sim 49.0°$	14.3 Å × 10.5 Å $\theta \sim 49.0°$
NTCDI	11.0 Å × 10.8 Å $\theta \sim 80.8°$	10.3 Å × 9.4 Å $\theta \sim 72.9°$	10.2 Å × 9.3 Å $\theta \sim 71.7°$
BDG + NTCDI	26.0 Å × 13.7 Å $\theta \sim 35.6°$	24.3 Å × 15.4 Å $\theta \sim 34.0°$	23.9 Å × 15.6 Å $\theta \sim 31.8°$

In Table 5.1 the calculated lattice parameters are summarised along with the experimental ones. We see that there is a reasonable good agreement between theory and experiment. For NTCDI, the minimum energy structure corresponds to the α phase shown in the bottom panel of Fig. 5.2b), where its unit cell is smaller than the measured unit cell. Since the observed structures exhibit registry with the Au fcc lattice underneath, such disagreement may be explained by the residual interaction with the substrate [166]. Nonetheless, the individual molecule orientation on the surface cannot be determined in

[2]NEXAFS experiments confirm the planar adsorption of this molecules, see Sec. 5.4.2.

the present STM image. Then, a packed structure with alternative tilted molecules along the short axis (γ phase), such as the one proposed by Keeling *et al.* [167] for NTCDI on Ag/Si(111), is also possible. Indeed, further STM investigations with better resolution, showed also the existence of the γ phase for NTCDI on Au(111), as shown in Fig. 5.3a). Moreover, recent studies by Cañas-Ventura *et al.* [160] using the PTCDI molecule, which is larger than NTCDI but has the same terminations, show co-existence of α-like phase domains, adjacent to γ-like phase domains [Fig. 5.3b)]. This all suggests that both type of packings are almost isoenergetic.

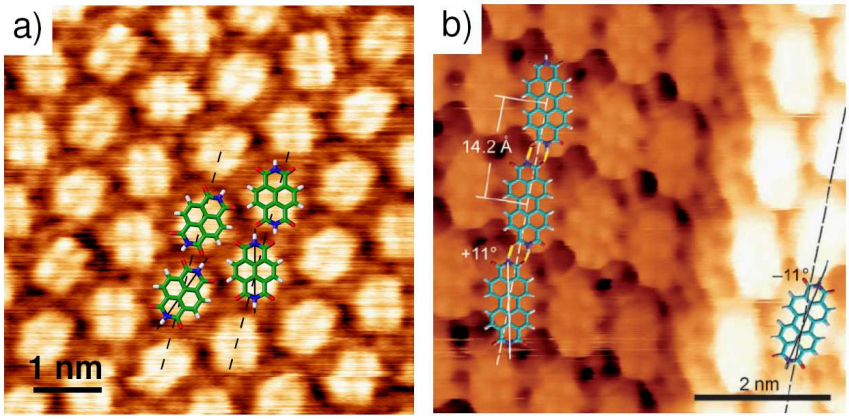

Figure 5.3: a) High resolution STM image of NTCDI self-assembly on Au(111) substrate (V = -0.03 V). It shows a packing with alternating molecular orientations, the γ phase. b) High resolution STM image of PTCDI on Au(11,12,12) vicinal (V = 0.06 V, I = 0.09 nA). Two canted configurations ($\pm 11°$) are visible [160].

In the case of BDG, the calculated long and short axes are expanded and contracted respectively as compared to the experiment. The interaction with the substrate again explains such differences. One can indeed observe that the BDG monolayer is in registry with the herringbone superlattice. With respect the mixed BDG-NTCDI monolayer on Au(111) [Fig. 5.2c)], after co-evaporation of both molecules and additional annealing to $\sim$ 450 K, the self-assembly and mutual molecular recognition steer the system to a packed structure with alternating BDG-NTCDI dimers. Binary chains are not aligned along high symmetry directions of the Au crystal. The calculated lattice constants match reasonably well the measured lattice constants. Thus, molecule–substrate interactions do not appear to have such a strong influence in the assembly of the heterogeneous structure.

From the DFT calculations we can extract the length of the different H-bonds in the 2D supramolecular assemblies[3]. For BDG 2D structure, the corresponding HNH$\cdots$N bonds are 1.89 Å and 2.12 Å, for the frontal and lateral bonds, respectively. There is a relatively strong complementary HNH$\cdots$N doublet along the molecule axis and a weaker sideways bonding. The latter is defined by the interaction of the proton of the remaining

[3]The H-bond lengths within the tetramer structures barely change [159].

NH_2 group with the inner N atom of the triazine. For the α phase of NTCDI, the frontal NH$\cdots$O H-bond accounts for 1.74 Å, and the lateral CH$\cdots$O bond length is 2.12 Å. Finally, in the mixture, the frontal NH$\cdots$N and HNH$\cdots$O bond distances are 1.72 Å and 1.83 Å, respectively, whereas the lateral HNH$\cdots$O bond is 2.55 Å long. Such a difference reflects a weaker hydrogen bond between the 1D chains, as compared to the stronger BDG/NTCDI bonding along chains. We must also note that although defects in the binary structure have been observed, these are mostly limited to stacking fault lines parallel to the 1D chains. Point defects along chains appear very seldom. Therefore, the BDG-NTCDI monolayer can be considered as a 1D stack of alternating, heterogeneous BDG/NTCDI wires. To sum up the three cases, the optimised geometries present shorter frontal H-bonds than lateral ones, i.e., there are weaker H-bonds between adjacent 1D chains, as compared to the stronger bonding along the chains.

The stabilisation energy upon formation of the periodic 2D assembly can be computed as the energy difference between the free standing monolayer, and the isolated components. It turns out to be -0.82±0.02 eV (-18.90±0.46 Kcal/mol) per unit cell for pure BDG and -0.80±0.01 eV (-18.45±0.23 Kcal/mol) for pure NTCDI, while for the mixture it increases to -2.01±0.02 eV (-46.35±0.46 Kcal/mol) per unit cell[4]. This notorious difference can be readily explained. On the one hand, the latter contains two distinct molecules per unit cell forming a dimer with a triple H-bond, thus, there is a larger number of interactions (H-bonds). On the other hand, the strength of the different bondings is not the same. Presumably, the shorter the bonds the larger the energy gain. In order to estimate the binding energy of the different H-bonds, we first count the number of H-bonds per unit cell. It is 4 for the pure structures, and 8 for the binary one. Thus, on the average the interaction energy per H-bond is $\sim$ -4.72 Kcal/mol and -4.61 Kcal/mol for the pure BDG and NTCDI systems, respectively, and $\sim$ -5.79 Kcal/mol in the mixture. This result agrees with our initial postulate about the formation of dimers with strong triple H-bonds. In fact, if we calculate the interaction energy of a BDG-NTCDI dimer as $E_b = E_{BDG-NTCDI} - E_{BDG} - E_{NTCDI}$, which accounts for -0.87±0.01 eV (-20.06±0.23 Kcal/mol), we find out that on the average the interaction energy per H-bond within the dimer is $\sim$ -6.67 Kcal/mol. However, the energy gain per bond in the mixture ($\sim$ 1.13 Kcal/mol) is not as large as deduced from the dimer formation ($\sim$ 2.01 Kcal/mol). This suggests that, in spite of the stronger frontal H-bonds between amine and imide end groups, the lateral interactions within the mixture are slightly weaker than in the pure systems.

[4]The error bar is due to calculations with different smearings.

5.2.2 STM simulations

We have shown that the interaction of these planar ring systems (BDG and NTCDI) with Au(111) is rather weak. They are physisorbed via the long range van der Waals interaction. Therefore, we could not use DFT methods to get accurate adsorption geometries or energies on Au. However, we have checked that, for individual molecules placed above the Au(111) surface, the appearance of simulated Tersoff-Hamann (TH) STM images do not change in a physically acceptable molecule–surface distance around 3 Å. Then, we introduce the Au(111) surface as a source of signal to simulate more realistic STM images than the ones obtained with the bare molecule, since they only show the molecular orbitals. This is represented in Fig. 5.4, where we show a comparison of simulated constant height STM images for both BDG and NTCDI molecules, isolated, and "adsorbed" on Au(111) at different vertical distances. It can be seen, that the effect of the substrate is to smooth the contours, and this effect decreases when the molecule–surface vertical distance increases, recovering the shape of the isolated molecule.

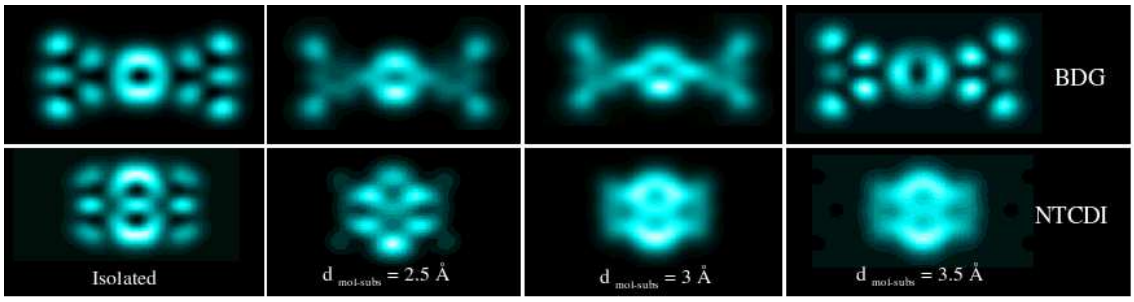

Figure 5.4: Constant height TH STM images with V = -1.5 V, for both BDG and NTCDI individual molecules, in the upper and lower panel, respectively. From left to right, the simulations correspond to isolated molecules, and the molecules placed at 2.5 Å, 3 Å and 3.5 Å from the Au(111) surface. The contour plots have been taken at 2 Å from the molecule.

The ground-state of isolated molecules was calculated using large enough unit cells to avoid residual interactions with neighbour molecules. The size of the unit cells was $22\times15\times10$ Å^3 and $20\times15\times10$ Å^3 for BDG and NTCDI, respectively. The Au(111) surface was modelled with a slab made of four Au planes, and 24 Au atoms per layer. It corresponds to the $6\times2\sqrt{3}$ cell. In order to calculate the individual adsorption of molecules on Au(111), the desired molecule was fixed to a given vertical distance from the substrate (keeping at least ≥ 10 Å of vacuum). Then, without any relaxation we just calculate the charge density of the system and simulate the STM image within the TH approximation as described in Sec. 2.3.4 of Chapter 2.

The shape of the features seen in the experimental STM images is nicely reproduced by our STM simulations. In the case of BDG-NTCDI dimer on Au(111), we use a larger Au slab. It also contains four layers of Au, but 48 atoms per layers ($6\sqrt{3}\times4$ cell). Fig. 5.5

shows a constant current STM simulation for the dimer placed at 3 Å from the surface. It allows us to identify the relative orientation of the more rounded NTCDI molecule within the heterogeneous assembly.

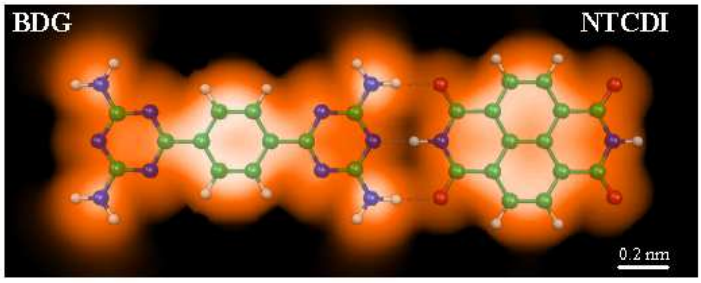

Figure 5.5: Constant current simulated TH STM image with V = -1.5 V, for the BDG-NTCDI dimer adsorbed at 3 Å from Au(111). The plot has been taken at an integrated LDOS = 3×10^{-5} $e^-/Å^3$. Superimposed to the simulated STM image a schematic structure of the BDG-NTCDI dimer is depicted.

5.2.3 Weak-non-negligible surface–molecule interaction

We have mentioned in the previous section that, although the interaction between the NTCDI and BDG with the Au(111) surface is weak, a residual interaction remains. There are different experimental evidences that prove it [166].

Fig. 5.6 shows STM images (top) and surface state band dispersion angle resolved photo-electron spectroscopy (ARPES) measurements (bottom) for NTCDI and BDG covered Au(111), as compared to data from the clean Au(111) surface. The persistence of the Shockley surface state, and the herringbone reconstruction indicates that the interactions between the substrate and the molecular overlayers are relatively weak. In contrast, for highly interacting π-like conjugated molecules such as F_{16}CuPc, the reconstruction is entirely lifted and the surface state quenched [168]. Nonetheless, notice in the present case, the subtle changes in the reconstruction pattern and the surface state band upon molecule adsorption.

The hcp/fcc periodicity of the herringbone reconstruction is measured along the $[1\bar{1}0]$ direction [see Appendix I for details]. For the clean Au(111) substrate a periodicity of 72±3 Å is obtained. This value slightly differs from the perfect herringbone pattern, because it may vary due to the quality of the surface, presence of defects, steps, etc. These values are averages obtained over different areas without remarkable surface defects. On the contrary, for the covered surface, the herringbone periodicity increases to 78±3 Å under NTCDI, and to 82±3 Å under BDG. This result suggests that BDG has a stronger tendency to lift the herringbone reconstruction, and hence it has a stronger interaction

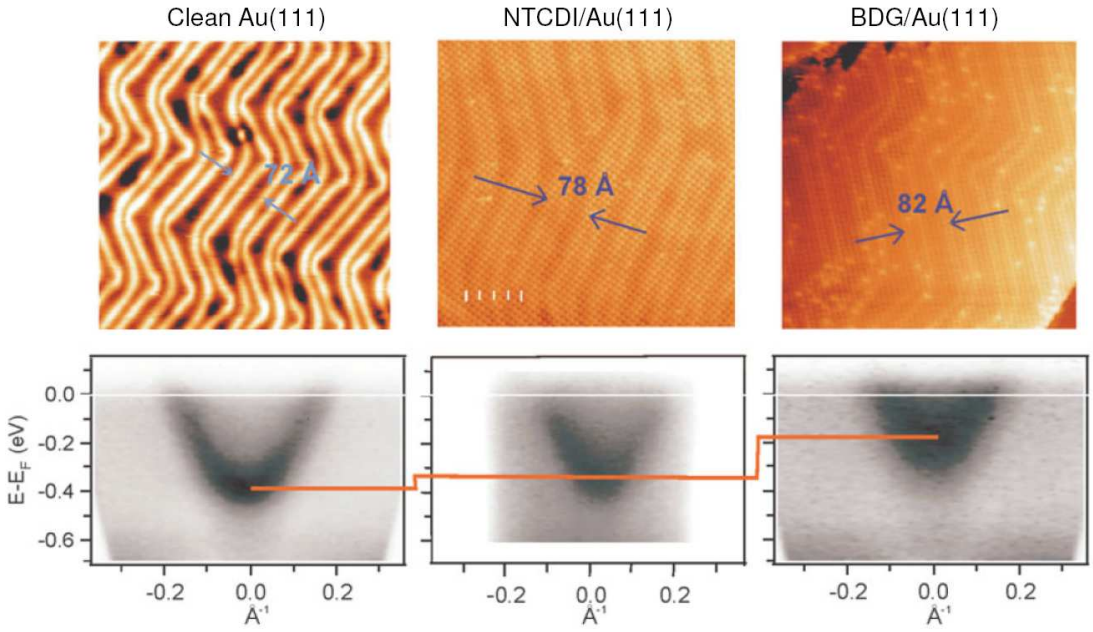

Figure 5.6: STM images (60×60 nm^2) and angle resolved photoemission surface state band measurements of the bare Au(111), as well as NTCDI and BDG covered Au(111). The line in the photoemission data evidences the shift of the surface state, in direct correlation with the modified herringbone reconstruction periodicity as observed by STM [166].

with the Au substrate. Furthermore, photoemission measurements of the surface state band in Fig. 5.6 evidence a shift from -0.39 eV in the clean Au(111) surface to -0.33 eV and -0.18 eV in NTCDI and BDG monolayers, respectively[5]. This trend correlates with the increasing strength of the molecule–substrate interaction from NTCDI to BDG. In fact, despite the limitations of DFT in describing weak dispersive van der Waals forces, theoretical calculations of the binding energy changing the distance from the molecule to the substrate, follow qualitatively a similar trend as the experimental observations. From the interaction curves shown in Fig. 5.7, where binding energy is plotted vs molecule–surface distance, we conclude that BDG interacts stronger with Au than NTCDI. The calculated data have been fitted with a Morse potential. The resulting values are, E_b = -0.26 eV for BDG and -0.06 eV for NTCDI. Besides, the equilibrium vertical distances turn out to be, 3.77 Å and 4.24 Å for BDG and NTCDI, respectively. Therefore, according to DFT, BDG adsorbs closer and stronger to the Au(111) than NTCDI.

It has been already noted previously [Sec. 4.3.2 in Chapter 4], that the origin of surface state's shifts can be attributed to changes in the surface potential due to induced dipoles or charge transfer processes. Obviously, differences in the molecule–surface distance, as well as the geometric structure of the molecule may play a role too. Since the effective mass of the surface state (SS) band is the same in both systems (the dispersion

[5]The binding energy is affected by limited angular resolution (0.6°) in the present photoemission experiment. Actual values should be slightly higher.

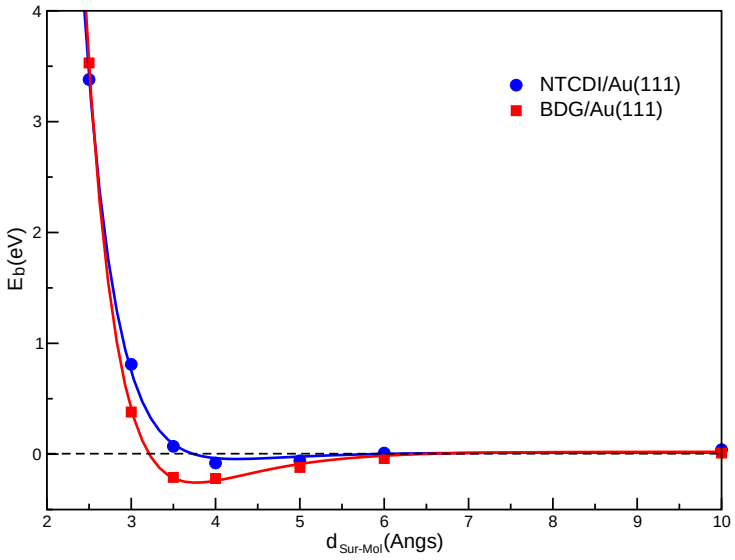

Figure 5.7: Interaction curves for BDG and NTCDI adsorption on Au(111). Solid lines are fittings to a Morse potential, $y = a_0 + a_1 \left(1 - e^{-a_2(x-a_3)}\right)^2$.

close to the minimum is the same), the occupation of the surface state is simply proportional to its binding energy (band minimum). STS experiments show that the LUMO orbitals of both NTCDI and BDG are located more than 1 eV above the Fermi level, that is, a charge transfer process cannot be the reason for the changes in the occupation of the SS band. The charge transfer in both NTCDI and BDG adsorption on Au can be neglected. Furthermore, DFT calculations predict distinct adsorption distances for BDG and NTCDI. This may affect the effective confining potential of the surface electrons [169]. Intuitively, the smaller molecule–surface distance of BDG as compared to NTCDI, could narrow the confinement potential and enhance the surface state energy, in agreement with the photoemission experiments [166].

5.3 Supramolecular binary structures with uniaxial anisotropy

We have shown how the appropriate election of molecules, with a well defined geometry and electronic properties, gives rise to 2D large domains of ordered binary structures on metallic substrates. The mixture shown in Fig. 5.2c) is considered to be a 1D stack of wires formed by alternating BDG-NTCDI dimers, without a preferential alignment with the underlaying Au(111) substrate. However, after co-evaporation of $\sim$ 0.9 ML of 50 % BDG and 50 % NTCDI on the Au(455) vicinal surface, well oriented binary structures are indeed obtained over large portions of the surface [159]. This is shown in Fig. 5.8, where it can be seen that binary structures co-exist with BDG-rich and pure-NTCDI areas.

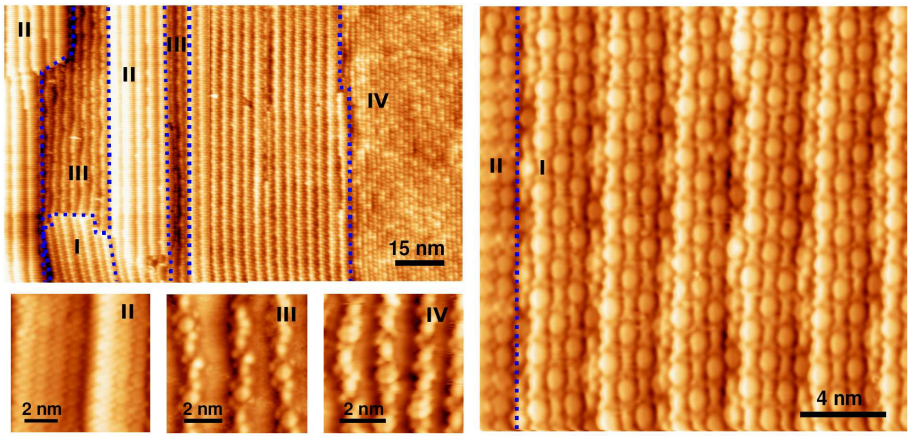

Figure 5.8: STM images after co-adsorption of 0.9 ML of BDG and NTCDI on Au(455). A 1D, multiple phase separation (dotted blue lines) is observed. Right panel shows the binary molecular recognition structure lined up along step edges (phase I). Bottom-left panels show a detailed view of phases II (pure-NTCDI), III (BDG-rich on wide terraces) and IV (BDG-rich on narrow terraces).

The different phases are marked as I, II, III, and IV in the upper-left panel of Fig. 5.8. In the absence of surface defects, the phase boundaries are located at step edges (blue dotted lines), and hence an effective 1D phase separation operates. The Au(455) surface is characterised by a periodic faceting of wide and narrow terraces, that is, alternated Au(233) and Au(677) facets, defined by periodic arrays of $\sim$ 14 Å and $\sim$ 32 Å wide terraces, respectively [170]. Under the molecular overlayer the substrate keeps its periodic faceting[6]. The wide-terrace facets contain phase I (binary), phase II (pure-NTCDI), and phase III (BDG-rich), while the narrow-terrace facets only host the BDG-rich phase IV.

The binary phase I, shown in the right panel of Fig. 5.8, is the heterogeneous molecular recognition structure analogous to the one obtained on Au(111). However, the vicinal surface steers the formation of a single domain aligned with the step array, that is, a binary structure with well defined uniaxial anisotropy. This phase is defined by a compact binary structure, namely, a regular packing of four NTCDI/BDG wires per terrace, and a different packing sequence across steps. We conclude then that a residual interaction between rows in contiguous terraces exists, in contrast to a stronger row-to-row interaction inside the terraces.

Detailed information about phases II, III and IV are extracted from the STM images in the bottom-left panel of Fig. 5.8. Phase II turns out to be a pure-NTCDI structure packed inside wide terraces. Both III and IV phases on the contrary show 3:1 BDG:NTCDI stoichiometry and random step edge decoration. These phases reflect the distinct trend of NTCDI and BDG to aggregate or decorate steps, respectively. In fact, the evaporation

[6]The two characteristic terrace sizes after molecule adsorption change slightly from the bare crystal surface.

sequence of different species does not affect the phase segregation. This points towards energy constraints, that is, competing driving forces as the origin of the presence of frustrated binary phases, excluding the probable reduced kinetics across the steps as its origin.

Moreover, binary structures are not observed within the narrow terraces, which only exhibit decorated steps or partial terrace filling. This strongly suggests terrace size restrictions on the BDG-NTCDI heterogeneous assembly. The experiments indicate that steps introduce a distinct hierarchy of driving forces for each molecule, leading to a multiple phase segregation. As a consequence, the presence of ideal aligned heterogeneous structure appears to be limited to surfaces with relatively wide terraces [159].

5.4 Spectroscopic fingerprint of Amine and Imide functional groups

In order to get a deeper insight into the interactions driving the supramolecular assembly, photon-in spectroscopies, such as X-ray photoemission (XPS), valence-band ultraviolet photoemission (UPS), and near-edge X-ray absorption fine structure (NEXAFS) spectroscopy, appear to be very powerful. They can provide the spectroscopic fingerprints of the different atomic species, in particular, those located at functional groups, that is, those involved in supramolecular bonding.

BDG and NTCDI molecules have strongly active amine and imide functional end groups, respectively. These are in turn characterised by the presence of N and O atoms, which may act as labels of functional groups in atomic-sensitive XPS and NEXAFS. The different spectroscopic features in absorption and core-level photoemission spectra experiments are understood in terms of contributions from different core and molecular levels at N and O atom sites. This is done by combining experiments with DFT calculations [171].

Experiments were carried out at the UE56/2-PGM1 beamline at the BESSY synchrotron in Berlin (Germany), using linearly polarised light and a SPECS 100 high resolution angle-resolved hemispherical analyser. 20 eV pass energy was used for UPS measurements and 50 eV pass energy for XPS, whereas NEXAFS spectra were recorded in Auger yield mode, with 100 eV pass energy and kinetic energies of 260 eV, 375 eV and 510 eV for the C, N, and O K-edges, respectively. Spectra are normalised with those taken for the clean Au(111) surface. The electronic structures of isolated BDG and NTCDI were calculated using the plane-wave based DFT code VASP. After optimisation of the geometry, the self-consistent charge density was used to generate both the projected density of states (PDOS) at the N and O atoms, and the spatial charge density of the series of unoccupied LUMO, LUMO+n molecular levels.

5.4.1 XPS and UPS

First, the measured O 1s and N 1s core-level spectra corresponding to 0.6 ML BDG and 0.6 ML NTCDI on Au(111) are shown in Fig. 5.9a). The photon energy was selected to enhance surface sensitivity. Binding energies are referred to the Fermi level, and Au(111) background emission was subtracted from the measurements. The data are fitted [red lines] using two Lorentzian lines for the N 1s spectrum of BDG, and a single line for the O 1s and N 1s spectra of NTCDI. In all cases the best fit is obtained for a constant peak width of 1 eV. In the N 1s peak of BDG, the two components, A and B, appear at 398.4 eV and 397.4 eV, with a 2:3.4 intensity ratio. This value is close to the 2:3 ratio expected from the relative number of N atoms within the amine groups (4) and within the triazine rings (6). Core-level energies are known to characterise the local oxidation state of an element, that is, the chemical environment. The N in the BDG molecule has two different chemical environments, N within the amine groups and triazine rings. Therefore, the two components in the N 1s peak, with 1 eV core-level shift and ∼2:3 intensity ratio, become identified. For NTCDI, the imide end group contains single N and O atomic species, and hence single peak features at 399.0 eV and 530.1 eV are measured in the respective 1s spectra [171]. These data are useful for later NEXAFS analysis.

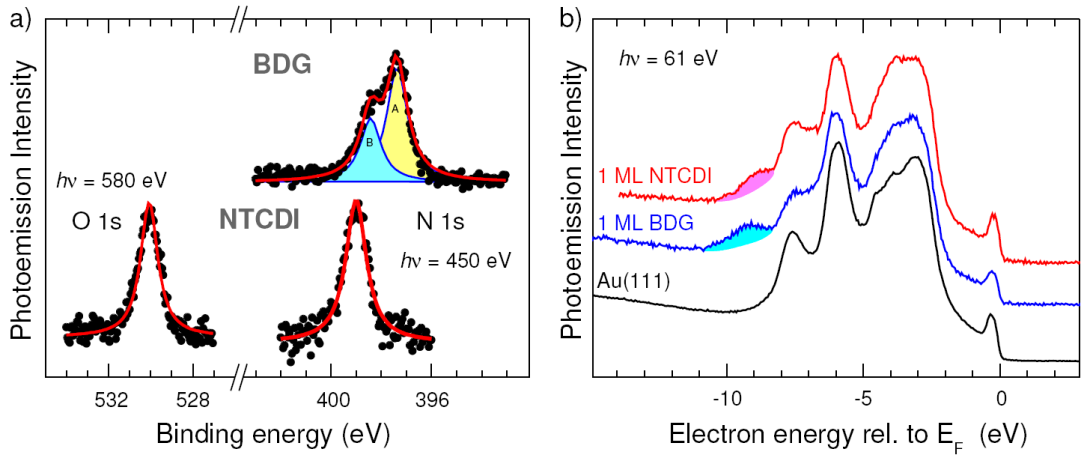

Figure 5.9: a) N 1s and O 1s spectra characterising end group atoms in 0.6 ML of NTCDI (bottom) and BDG (top) on Au(111). The A and B peaks in the BDG spectrum correspond to atoms in triazine rings and amine groups, respectively. b) Angle-resolved, valence-band photoemission spectra from 1 ML BDG and NTCDI on Au(111), and clean Au(111) taken with normal emission geometry. Main features correspond to emission from the Au 5d band and Shockley surface state, which is also visible under molecular layer. Only the shaded feature emerges as a single valence-band fingerprint for BDG and NTCDI [171].

The valence band photoemission results are shown in Fig. 5.9b). The spectra are dominated by the high signal intensity from Au 5d levels that hide occupied molecular level structures. Only the peaks at ∼ -9 eV [shaded peaks] can be attributed to occupied

molecular orbitals. The most remarkable feature is the presence of the Au-like surface state close to E_F in the molecular monolayer spectra, that presents an upward shift of $\sim$ 150 meV with respect to the clean Au(111). This is accord with what has been shown in Sec. 5.2.3.

5.4.2 NEXAFS and LUMO orbitals

In contrast to valence-band photoemission, NEXAFS experiments provide a clear identification of the empty molecular level structure. X-rays are absorbed through excitations of core electrons to empty states above the vacuum or Fermi level. Created holes are then filled by Auger decay. The intensity of the emitted primary Auger electrons is a direct measure of the X-ray absorption process and is used in the so-called Auger electron yield measurements, which are highly surface sensitive, similar to XPS. NEXAFS is element specific because the X-ray absorption edges of different elements have different energies. It is also dependent on the polarisation of the electric field (or the incidence angle). For a planar molecule adsorbed flat on the surface, when the electric field vector $\overrightarrow{E}$ is aligned along the surface normal, i.e., grazing incidence, peaks due to the out-of-plane π^* orbitals are probed, and when $\overrightarrow{E}$ is parallel to the surface, that is, normal incidence, resonances due to the in-plane σ^* orbitals are dominant. This shows whether a molecule lies down or stands up on the surface, as it is schematically depicted in Fig. 5.10.

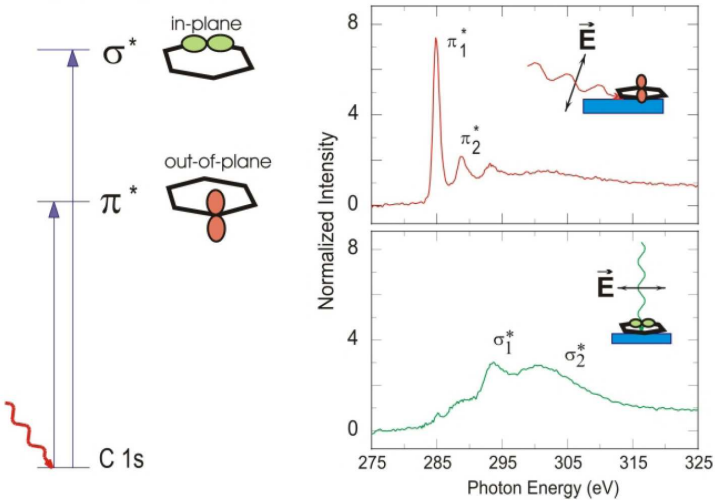

Figure 5.10: Polarisation dependent NEXAFS spectra of benzene on Ag(110), illustrating the capability to determine molecular orientations [172].

Fig. 5.11 shows the spectra of the N and O K-edges for NTCDI [Fig. 5.11 a)] and the N K-edge for BDG [Fig. 5.11 b)] compared to calculated PDOS. The PDOS on N and O atomic sites were obtained from DFT calculations of BDG and NTCDI isolated molecules, as described in the methodology section [Sec. 2.3.3]. The thick lines are spectra

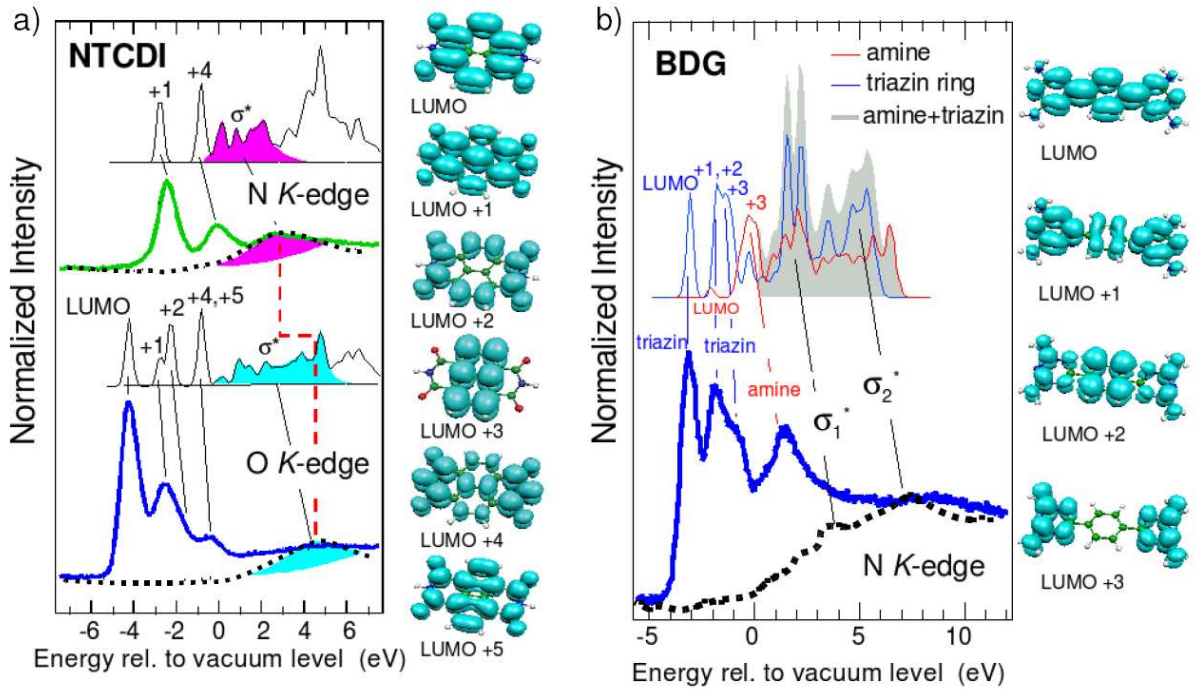

Figure 5.11: NEXAFS spectra from the NTCDI monolayer on Au(111) measured at N and O K-edges a) and from the BDG monolayer measured at the N K-edge b). The thick and dotted lines respectively correspond to *p*- and *s*- like polarisations. Calculated PDOS onto N and O atoms (on top) and the spatial charge distribution for empty levels (right panel) of each isolated molecule are also shown. The energy scale in the DFT calculation is defined by matching theory and experiment at the LUMO peak. The shaded areas indicate the σ^* character.

taken with 80° light incidence with respect to the surface normal (*p*-polarisation) and the dotted lines spectra recorded with 10° incidence (*s*-polarisation). The latter shows a dramatic quenching of the π^*-like features, demonstrating the planar conformation of the molecules with respect to the surface. For a proper comparison of the different edges, the usual photon energy scale is converted into a binding energy scale using the vacuum level as a reference [173]. This is done by subtracting the corresponding 1s core-level binding energies referred to the vacuum level. Note that the vacuum level reference in Fig. 5.11a) leads to a consistent alignment (± 50 meV) of the whole series of molecular levels for N and O spectra.

The assignment of NEXAFS peaks to the different molecular levels can be readily done in the light of the PDOS calculated for end group atoms (N and O). The energy scale in the theoretical calculation is shifted to match the lowest-energy LUMO feature in the NEXAFS spectra. As frequently observed in physisorbed molecules, such LUMO alignment neglects the core-hole screening energy, which is present in NEXAFS and not accounted for in the DFT approach. The core-hole screening decreases as we move away from the LUMO level, leading to an overall stretching of the NEXAFS spectra with respect to the calculated PDOS, as observed in Fig. 5.11.

For NTCDI we find six π^* levels in the low-energy side, from LUMO to LUMO+5, which are easily found in the NEXAFS spectra. The LUMO+4,+5 peak is actually defined by two different levels split by 30 meV, which are thus indistinguishable in NEXAFS. The most remarkable observation in Fig. 5.11a) is the quenching of particular molecular level features in the N and O spectra. This is explained by the locally depleted charge density of molecular levels. For a better description of this effect, on the right of Fig. 5.11a) we show the spatial charge distribution for empty levels[7]. The LUMO, LUMO+2, LUMO+3 and LUMO+5 charge density is zero at N sites (blue balls), in contrast to the significant charge density in the LUMO+1 and LUMO+4 levels. For O, only the charge density at the LUMO+3 level is significantly reduced, and hence the corresponding absorption peak is absent.

In the case of BDG, we find four π^* levels from LUMO to LUMO+3, with LUMO+1 and LUMO+2 split by only 0.1 eV. Note that in Fig. 5.11b) we separately display the calculated PDOS for N atoms within triazine rings and at amine sites. In fact, for a correct comparison with the experiments one has to take into account the core-level shift between them, shown in Fig. 5.9a). Therefore, the PDOS of the amine N (red line) must be shifted up by 1 eV with respect to the PDOS of the triazine N. The LUMO PDOS at amine N is not relevant, which is also reflected in the spatial charge distribution shown in the right side of Fig. 5.11b). Then, such a shift and the fact that at amine the LUMO is not relevant, leaves the π^* emission from triazine N (blue line) as the only contribution to the lowest three features in the NEXAFS spectra. For the same reason, the fourth NEXAFS peak can be assigned to absorption into the LUMO+3 orbital of amine N.

For π-conjugated molecules that adsorb flat on the surface, such as NTCDI and BDG, local σ^* orbitals in end group atoms are central to an understanding of supramolecular bonding. The σ^* orbitals along the plane of the molecule are expected to undergo major changes upon molecule–molecule binding as compared to out-of-plane orbitals. By contrast, π^* levels extend perpendicular to the molecule plane and do not significantly interact from molecule to molecule. In this case only minor polarisation effects are expected. The σ^*-like character of molecular orbitals in the planar adsorption geometry is probed by switching the polarisation of the light to *s*-like [dotted-line spectra in Fig. 5.11]. In Fig. 5.11 the shaded areas[8] mark the position of the strongest σ^* features at N and O sites, which are also reflected in the corresponding PDOS calculation. For BDG, the σ^* maximum does not contain any particular triazine-ring or amine-group character. However, for NTCDI it is interesting to note that the centre of gravity of the PDOS σ^* band moves upward from N to O sites, as observed in the NEXAFS spectra.

[7] 3D plots have been made using MOLEKEL 4.3 [174].

[8] For BDG, the grey shaded area in Fig. 5.11b) is the sum of the PDOS for triazine and amine N atoms, which are already weighted with the relative number of atoms.

5.5 Summary and conclusions

Experimentally it has been observed that the co-adsorption of linear, planar molecules with complementary end groups gives rise to supramolecular binary structures with strong uniaxial anisotropy. DFT methods cannot describe correctly the interaction of this kind of molecules with the Au(111) surface. However, they can be used to calculate the geometries of the 2D assemblies in the absence of gold, comparing reasonably well with measured lattice parameters. Furthermore, we have included the presence of the Au(111) surface in the simulations of STM images as a source of signal, and nicely reproduce the shapes found in the experiment. This allows us to identify with no doubt the relative orientation of molecules within the assembly. We have also demonstrated that although for BDG and NTCDI on Au(111) the molecule–substrate interaction is weak, this is not negligible. Both the surface state and herringbone reconstruction remains after molecular adsorption, but both suffer subtle changes. Interestingly, experiment and theory agree in that BDG has a stronger interaction with the surface than NTCDI. This cannot be explained as charge transfer processes, but as a change in the effective confining potential of surface electrons. The use of prepatterned surfaces, such as a Au(111) vicinal surface, steers the formation of single domains of binary structures aligned with the step edges. Nevertheless, as the steps introduce a distinct hierarchy of driving forces for each molecule, the presence of a perfect heterogeneous structure is somehow limited to surfaces with relatively wide terraces.

Finally, we give the spectroscopic fingerprints of BDG and NTCDI molecules in supramolecular assemblies. We show that DFT calculations for isolated molecules, combined with an analysis of photoemission and NEXAFS spectra, allows us a thorough electronic state description of individual N and O species that characterise the strongly active amine and imide functional end groups.

Chapter 6

Summary

A study of the geometries and electronic properties of organic molecular thin films adsorbed on Au(111) has been presented in this thesis. It contains DFT-based *first principles* calculations, that have been compared to experimental results, mainly STM/STS measurements. Three different systems have been analysed in detail: chemisorption of small thiolates, donor–acceptor charge-transfer complex adsorption, and co-adsorption of complementary polyarenes. These systems cover a wide range of the different strategies used to grow SAMs. Indeed, the relative strength of the interactions that steer the self-assembly of such films, ranging from strong to weak adsorbate–substrate interactions with distinct adsorbate–adsorbate interactions, results in a perfect playground to understand the underlaying physics in the formation of SAMs. With that aim we have used different theoretical tools throughout this work, that include, besides relaxed geometries and energetic analysis, induced electron densities, PDOS on atomic sites and molecular orbitals, band structure calculations, charge transfer analysis, etc.

First, the singular S–Au bond, determinant in molecular junctions or in the assembly of different SAMs has been characterised in detail. This has been done by studying the S–Au dimer, the adsorption of S on Au(111), as well as the adsorption of SH and SCH_3 on Au(111). After a thorough analysis, we have found that the essence of the S-Au interaction is already contained in the simplest case, i.e., the S–Au dimer. A comparison with other dimers has revealed that relativistic effects are responsible for the unique properties of this bond. The S–Au bond, both at the dimer and on the extended Au(111) surface, mostly originates from the sharing of charge between S(3p) and Au(5d) orbitals. What changes is the spatial charge rearrangement. This strong adsorbate–substrate interaction, with covalent character, is the ideal framework to use DFT based calculations.

The addition of a molecular backbone (–H or $–CH_3$) to the S-head does not modify the electronic properties. PDOS and induced densities have permitted us to show that there exists a charge transfer from the substrate to the singly occupied HOMO and to

the LUMO. However, the adsorption geometry does differ due to steric forces, which also explain why the bridgelike site is energetically more favourable than the hollow site. Despite the intense research done on the adsorption of methylthiolate (SCH_3) on Au(111), there are still open questions that have been addressed in this work. By means of comparing theoretical calculations with experimental data, we have confirmed that the most stable adsorption configuration corresponds to the tilted bridge-fcc, instead of to the top or hollow sites. Furthermore, our calculations at T = 0 K have concluded that the minimum energy configuration belongs to the $(\sqrt{3}\times\sqrt{3})$R30° structure and not to the c(4×2) structure as pointed out by some previous studies. Nevertheless, the energy differences are relatively small, and hence we do not deny the possibility of co-existence of both phases at finite temperatures.

The next chapter presented in this thesis has been devoted to the adsorption of TTF and TCNQ molecules on Au(111), both individually and as a binary mixture. While TTF chemisorbs through two S–Au bonds, in a similar fashion as thiolates do, TCNQ self-assembles in a saturated hydrogen-bonded network that presents a rather weak interaction with the substrate. DFT calculations is at its limit to describe this kind of physisorption, and thus, comparison with experimental data is essential.

This chapter has focused on the study of the electronic properties at organic–metal interfaces, and in particular, on the formation of hybrid bands at the interface of the TTF-TCNQ thin film and the Au(111) surface. DFT calculations allowed us to interpretate STM/STS experiments. Co-adsorption of TTF-TCNQ forms a donor–acceptor complex that lies flat on the surface. It gives rise to a stoichiometric mixed phase of alternating TTF and TCNQ rows, as shown by STM experiments. Conductance measurements have probed two distinct spectroscopic fingerprints: a sharp peak centred on the TCNQ rows that disperses along the rows, and a broader peak centred at the TTF rows. The origin and nature of these features have been understood thanks to the calculated band structures, and PDOS resolved in momentum space, as well as to 3D plots of the charge density distribution at different points of the Brillouin zone. While TCNQ is essentially unperturbed by the underlaying substrate, TTF hybridises with the Au(111) surface. This selective coupling creates a weak periodic potential across the molecular rows, and yields the formation of two interface bands split at the SBZ boundary. There, odd (charge at TCNQ) and even (charge at TTF) states with respect to the TTF rows are found. The interface bands exhibit a free-electron metal-like dispersion and the anisotropic structure imposed by the overlayer, and can be directly associated with the observed fingerprints. They present both molecular and metal character, but this hybrid character changes along the SBZ as the adsorbate–substrate coupling changes. A conceptual picture at the molecular scale describing the formation of OM hybrid bands has been given. This is important to design functional OM interfaces, that would successfully combine the high carrier mobil-

ity of metals with the advantageous properties of organic compounds. In particular, our results suggest that organic–inorganic interfaces may be engineered by tuning two factors: (i) the strength of donor–metal interaction and, (ii) the spacing between the donor (TTF) rows.

Finally, we have shown that the co-adsorption of BDG and NTCDI, two planar molecules with complementary amine and imide end groups, gives rise to a 2D supramolecular binary structure with a strong uniaxial anisotropy. Calculated geometries of free standing monolayers of pure BDG, pure NTCDI, and BDG-NTCDI mixture, agree quite well with the lattice parameters obtained from STM images. An analysis of the energetics and the H-bond lengths have demonstrated that lateral interaction between chains is weaker than the intra-chain interaction, as well as that the binary structure has somewhat stronger H-bonds due to complementary amine–imide bond formation. Since DFT is not able to account for the dispersive interaction between such polyarenes and Au(111), the effect of the substrate has been introduced as a source of signal to simulate realistic STM images, which have allowed us to identify the relative orientation of molecules within the assembly. The herringbone reconstruction and the surface state of Au(111) remain after molecular adsorption, but suffer subtle changes that are larger for BDG than for NTCDI. These are due to changes in the surface potential caused by the organic overlayer. The experiments have also shown that the use of a vicinal surface steers the alignment of heterogeneous chains with the step edges. However, as it introduces a distinct hierarchy of interactions for each kind of molecule, the presence of a perfect binary structure gets limited to rather wide terraces.

In addition, the spectroscopic fingerprint of BDG and NTCDI molecules in supramolecular assemblies have been given. We have proved that theoretical calculations of isolated molecules are useful to interpretate spectroscopic measurements. The combined analysis of photoemission data, NEXAFS spectra, calculated PDOS on N and O orbitals, and spatial charge distribution of LUMO+n states have permitted us to give a detailed description of the electronic state of individual N and O species. They characterise the active amine and imide functional end groups, which are commonly added to aromatic ring structures to force supramolecular motifs. Molecules with chemically different N atoms, like BDG, will give rise to complex N spectra with different components, that can be difficult to be sorted out. In contrast, the rather simple spectra of single-oxygen species, like NTCDI or PTCDA, may serve as an appropriate label to trace the amine/imide groups.

Appendix I

The Au(111) surface

I.a The Herringbone reconstruction

The Au(111) surface is a close packed surface, that exhibits the well known $(22\times\sqrt{3})$ herringbone reconstruction [175–183]. This reconstruction is formed by a surface contraction along the $[1\bar{1}0]$ direction. The surface stress is induced by an extra Au atom placed in the topmost layer for every 22 bulk lattice sites, i.e., 23 atoms sit above 22 atoms. It creates a surface modulation parallel to $[1\bar{1}0]$ direction with a periodicity of 63 Å. The $(22\times\sqrt{3})$ unit cell alternates regions of surface atoms sitting in hcp sites, and regions where the atoms occupy fcc sites. A corrugation of 0.2 Å has been measured between the hcp and fcc stacking regions[1]. Both regions are separated by stacking faults domains, the so-called soliton lines [Fig. I.1a)]. This lines run parallel to the $[11\bar{2}]$ direction, and rotates periodi-

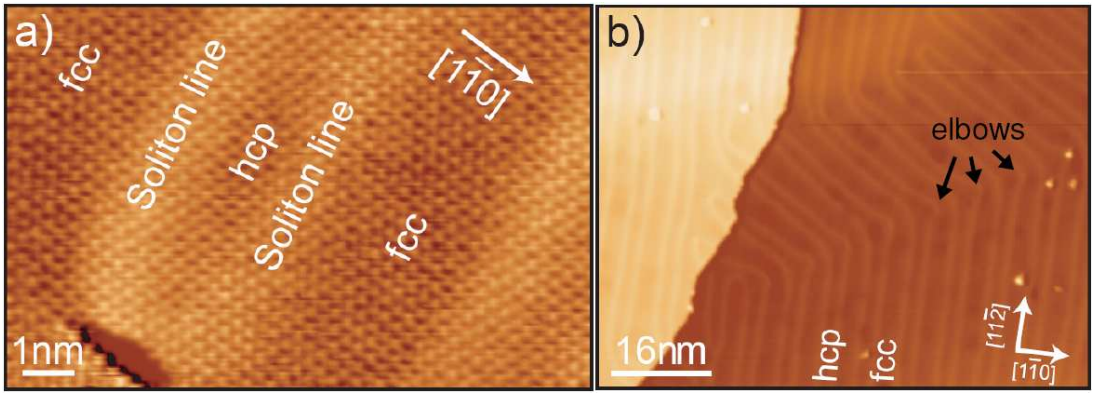

Figure I.1: a) Atomically resolved STM image revealing the atomic arrangement along the $[1\bar{1}0]$ direction that divides the surface in different regions separated by higher soliton lines (V = 1.2 V, I = 14 nA). b) Large STM image showing the Au(111) herringbone reconstruction on the surface (V = 0.86 V, I = 0.29 nA) [137].

[1]The width of the hcp domains is narrower than the width of the fcc domains.

cally by 120° creating the characteristic zig-zag pattern of the herringbone reconstruction [Fig. I.1b)]. The elbows of the reconstruction contain a single point dislocation with a lower potential. Thus, they act as preferential adsorption sites for adsorbates [183].

I.b Au(111) Shockley surface state

In addition to topographic features, the Au(111) surface has a characteristic electronic band structure that presents a two-dimensional intrinsic surface state (SS) band [184]. Typical of various (111) surfaces, the intrinsic surface states are originated by the breaking of the crystal symmetry at the surface. They are localised near the topmost atomic layer. These singular electronic states exist at the surface, but cannot exist in the bulk. In the quasi-free electron approximation (weak periodic potential), an energy gap opens at the Brillouin zone boundary [36]. Within this gap, states with real wave vector (k) are forbidden. However, Bloch's theorem does not prevent from solutions with imaginary k-vector to exist. Indeed, if we consider states with imaginary k-vector, although the solution (wavefunction) explodes in the solid, it does not in a semi-infinite crystal. Therefore, a wavefunction with imaginary wave vector can exist within the energy gap at the metal surface. This crystal-induced surface state, is called Shockley state [136]. Its corresponding wavefunction is maximum on the surface and decays exponentially away from the surface. Shockley SS emerges from a formalism (two band model) generally applied to the description of *sp*-bands in metals. There exists also a second type of surface state: Tamm states [185], which are split-off states of d- and f- valence band states.

The surface state electrons are confined to the topmost atomic layer of the metal, and hence, act as a quasi-2D free electron gas, giving rise to an electronic band with parabolic dispersion close to the minimum [see Eq. (4.1)]. Recent reported values of the Au(111) Shockley surface state's effective mass (m^*) and binding energy (E_0), measured both by photoelectron spectroscopy [149], and by STM [186] agree in $0.26m_e$ and -0.48±0.01 eV, respectively[2]. The signature of the Shockley surface state in the local dI/dV spectra is a sudden increase in the conductance at around the corresponding binding energy. It reflects as a steplike feature in the spectra, and it is used as a quality label of the clean metal substrate in STM experiments.

The metal surface used in the calculations throughout this thesis is Au(111). The computational cost in such *first principles* calculations is large, thus, it is fundamental to find a balance between unit cell's size and accuracy. As explained in Sec. 2.2, we use a slab made of atomic layers to model the desired surface. The larger number of planes, the better description of the continuous band structure of the metal.

[2]Other previous room temperature STM studies, that observed standing wave patterns at the Au(111) surface, give a different value for the effective mass ($m^* = 0.15m_e$) [148, 187].

In a symmetric slab, there are two (111) surfaces, the top and the bottom faces of the slab. Then, one expects two surface states, each located at each side of the slab. Ideally, both states should have the same energy, and same dispersion, i.e., they should be degenerated (wavefunctions differ in symmetry). This would be the case with a sufficient large slab, but for a typical slab size of seven planes, this is not the case. Fig. I.2a) shows the band structure for a Au(111) surface made of seven layers of gold, and using the 1×1 unit cell. We obtain two non-degenerate surface states [marked in red and green]. The planar average charge density along z-axis of the states at $\overline{\Gamma}$ is plotted in Fig. I.3a), where we see the localisation of the states at both surfaces. The states' density oscillates within the slab, but their amplitude decays away from the surface. Nonetheless, due to the presence of the two states, the amplitude reaches the minimum in the middle of the slab and it does not vanish completely.

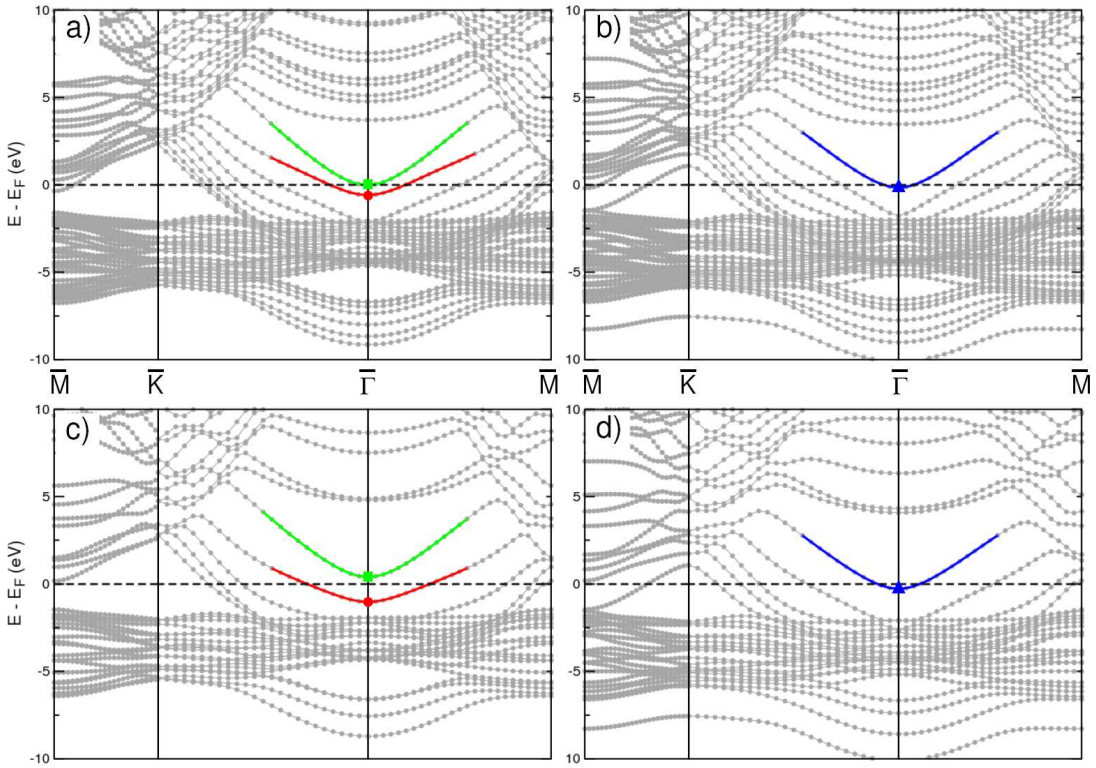

Figure I.2: Calculated band structure of Au(111) surface using the 1×1 unit cell. a) A slab modelled with seven gold layers. The two surface states are marked in green and red. b) Passivated seven layer Au slab, with the surface state in blue. c) Metal slab made of four atomic layers with surface states in red and green, and d) four layer Au slab passivated with H atoms on the bottom. The surface state is marked in blue.

Usually, molecules (or atoms) are adsorbed in one side of the slab (at the top), and we are interested in studying that interface in particular. In that case, a very effective way to quench one of the surface states, and obtain a more realistic surface state localised only at one of the surfaces, consists in passivating with hydrogen atoms the bottom of

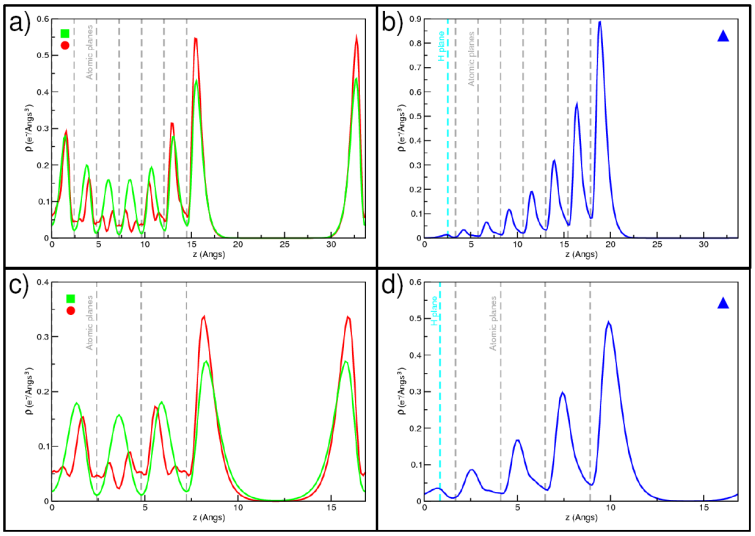

Figure I.3: Planar average charge density distribution of the surface states presented in Fig. I.2 at $\overline{\Gamma}$, plotted along z-axis. a) Slab made of seven gold layers. b) Seven Au layers slab passivated with H. c) Slab modelled with four metal layers, and d) four layers of gold and one H layer. Surface states are localised at the surface, and their amplitude decays within the slab.

the slab. Hydrogen atoms are adsorbed in fcc sites, one H atom per each Au atom. The resulting band structure in the case of a Au slab made of seven layers and passivated with H, is shown in Fig. I.2b). We see that there exists only one surface state [marked in blue], which is strongly localised at the slab's top surface, as shown in Fig. I.3b). Although the binding energy, E_0 = -0.16 eV, does not agree with the experimental binding energy of Au(111)'s SS, the spatial charge density distribution shows how it effectively decays within the slab, and it vanishes at the bottom.

In order to study the adsorption of TTF-TCNQ molecules on Au(111) [see Chapter 4], due to the large size of the system, we decided to model the metal slab with only four layers of gold passivated with H atoms. Contrary to what one may think, we demonstrate here that this slab is enough to obtain a qualitatively well described surface state. The calculated band structures with and without hydrogen are shown in Fig. I.2c) and I.2d), respectively. Again, we found two states [marked in green and red] localised at the surfaces (at $\overline{\Gamma}$) when the slab is not passivated with H at the bottom [Fig. I.3c)], while adsorption of H atoms suppresses one of the SS. In that case, it exists only one dispersing surface state [marked in blue], highly localised at the top surface [Fig. I.3d)]. If we compare the splitting of the two surface states with seven and four layers of gold (non-passivated), we can see how it decreases with the number of metal layers ($\sim$ 40% in this case).

Takeuchi *et al.* [188] succeeded to correctly reproduce the dispersion and energy of the Au(111) surface state using a slab model made of 15 gold planes [Fig. I.4a)]. They show that the surface state is localised in the top two or three layers [Fig. I.4b)]. Therefore, our assumption of the suitability of a metal slab made by four layers is further suppported.

The unit cell required to study the mixed adsorption of TTF and TCNQ molecules, described in Sec. 4.2, contains 19 atoms per layer. Its corresponding band structure is shown in Fig. I.5, where we see that all metal states (bulk and surface state) appear folded

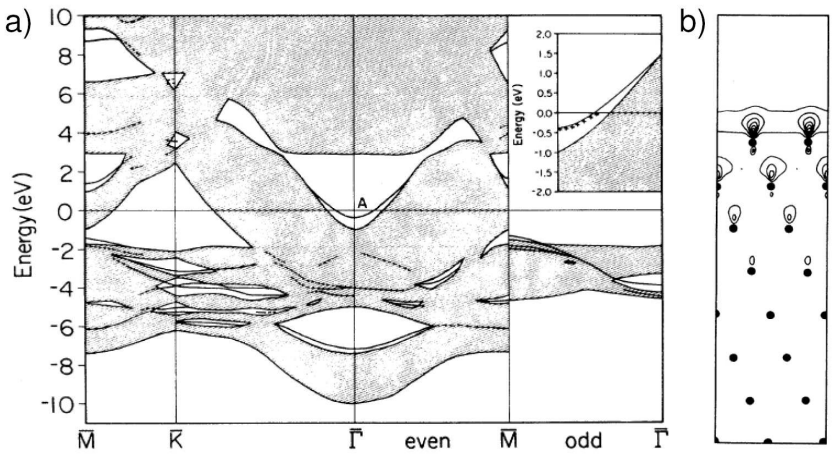

Figure I.4: a) Projected band structure along high symmetry lines for Au(111). Shaded areas indicate regions where bulk states can exist. The inset compares the dispersion of the surface state labelled A with photoemission data marked by crosses. b) Contour plots of the charge density of the surface state A at the $\overline{\Gamma}$ point [188].

due to the new periodicity of the cell, as compared to the 1×1 cell. In particular, we show the Au(111) surface state [marked in blue] and its backfolding at the SBZ boundary ($\overline{\text{X}}$ point). It is interesting to note, that along the $\overline{\text{XM}}$ direction of the SBZ the degeneracy at the zone boundary breaks. Thus, two dispersing surface states are found there. This is because, the $\overline{\text{XM}}$ direction does not correspond to any high symmetry direction of the 1×1 cell. At $\overline{\Gamma}$, the SS has a parabolic dispersion with a binding energy of -0.26 eV, and effective mass of 0.29m_e, in reasonable agreement with the experimental values [149,186].

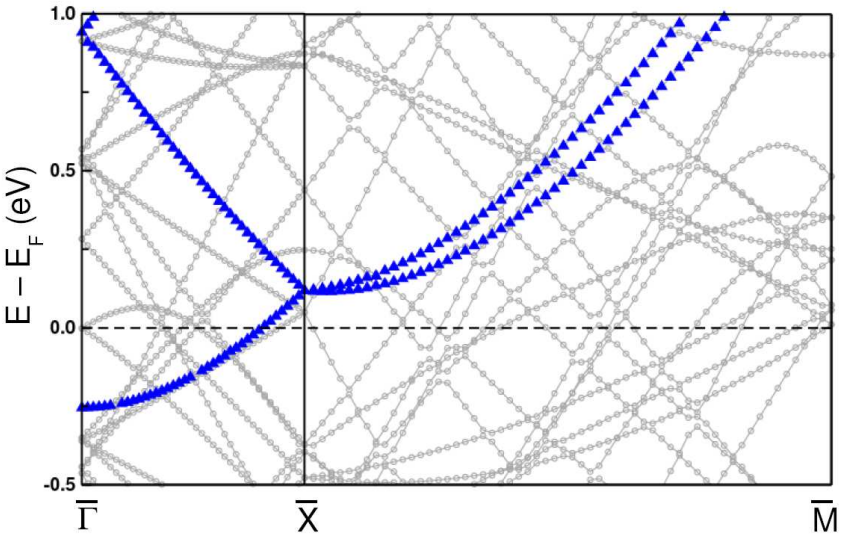

Figure I.5: Calculated band structure for Au(111) using the C19 cell along the $\overline{\Gamma\text{XM}}$ directions. Blue bands (▲) correspond to the surface state folded due to the new periodicity of the cell.

Laburpena euskaraz

Jadanik 1959. urtean, Richard Feynman-ek bere "There's plenty of room at the bottom" hitzaldi ospetsuan, tresna egokien laguntzaz atomoak eta molekulak mugi zitezkeela iradoki zuen [2]. Objektu baten osagaien neurria txikitzen goazen heinean, oso fenomeno interesgarriak sor zitezkeela adierazi zuen, gauza guztiak ez bait dira proportzio berean txikitzen. Esaterako, oso eskala txikian, grabitatearen eragina arbuiagarria gerta liteke molekulen arteko van der Waals indarrarekin konparatuz. Gogoan izan behar da, mekanika kuantikoaren legeek aginduta dagoela nanoeskalan gertatzen den fisika. Hartaz, gure ezaguera makroskopikoak ez digu balio. Feynman-en ideia ez zen soilik gauzak neurriz txikiagoak egitea, baizik eta gauzak erabilgarriak ere egitea. Hala ere, ez zen 1954. urtera arte, Norio Taniguchi-k "nanoteknologi" hitza asmatu zuela [3]. Molekulen eta atomoen eskalan materiaren kontrola helburutzat duen zientzia aplikatua da nanoteknologia. Kontrol horrek, nanoeskalan agintzen duen fisika eta prozesu kimikoen ezagutza zehatza eskatzen du.

Nanoteknologiak azken bizpahiru hamarkadatan izan duen sustapenean, besteak beste, 1981. urtean G. Binnig eta H. Rorher [4] zientzialariek asmatutako tunel efektuan oinarritutako mikroskopioak (STM) zerikusi handia izan du. Mikroskopio honi esker, materia eskala atomikoan ikusi daiteke. Nanomaterialek duten nano-neurria dela eta propietate bereziak dituzte. Ondorioz, bai oinarrizko zientzia eta baita teknologiaren ikuspuntutik ere, nanomaterial erabilgarriak garatzeko motibazio handia egon da. Nanozientziak alor ezberdinak biltzen ditu bere baitan; hara nola, fisika, kimika eta biologia. Hori dela eta, teknika ezberdin ugari erabili izan dira nanomaterialak egiterakoan. Orohar, teknika hauek bi multzotan bil daitezke, *top-down* bezala ezagutzen dena batetik, eta *bottom-up* hurbilketa [5–7] bestetik. Lehena, abiapuntu bezala osagai handiak hartuz tresna txikiagoak egitean datza. Hots, gure ordenagailuek dituzten mikroprozesadoreak etab. eraikitzeko erabili izan ohi diren teknikatan oinarritzen da. Bigarrena berriz, molekula eta atomoen auto-antolaketaren bidez osagai konplexuagoak eraikitzean oinarritzen da. Auto-antolaketa hau, molekulak elkarrengandik bereizteko duten gaitasuna eta kimika supramolekularra deritzonari esker ematen da [8, 9].

Molekulak elkarrengandik bereizteko gaitasuna, izaki bizidunetan gertatzen diren pro-

zesu biologikoen oinarria da, baita antolaketa supramolekularra gidatzen duenarena ere. Molekulez osatuta dauden eta interakzio ez-kobalente ahulen bitartez (batik bat hidrogeno loturak) auto-antolatutako sistema konplexuak lortzea da kimika supramolekularraren helburua. Kimika sintetikoaren bidez mota askotako molekulak eraiki daitezke, eta ondorioz, ezaugarri bereziak dituzten mota askotako sare supramolekularrak sortu. Hartaz, aplikazio nanoteknologikoetarako erabilgarriak diren funtzionalizatutako gainazalak edo nano-patroiak eraiki ditzakegu; esate baterako, dentsitate handiko diska magnetikoak, zelula edo molekula konkretuetan eragiten duten nanopartikula funtzionalizatuak, eta molekula organikoz osatutako multi-geruzak [152].

Gainazal solido, hau da, substratu baten gainean hazten diren bi-dimentsioko (2D) egitura supramolekularrek bereziki, interes handia piztu dute azken urteotan [10]. Auto-antolatutako geruza hauek, "Self-assembled Monolayer" (SAM) bezala ezagutzen dira eta tesi honen ikerketa gai dira. Hiru-dimentsioko (3D) egituretatik bi-dimentsiokotara pasatzean, gainazal solidoa izango da giltza. Substratu honen egitura elektroniko edo ezaugarri topologikoen eragina funtsezkoa gerta liteke gainean jartzen diren molekulen antolaketan. Honela, molekula egokiak aukeratzeaz gain, hauen auto-antolaketa zuzenduko duen oinarri egokia aukera daiteke ere. Prozesu guzti hau kontrolatu ahal izateko, molekulen artean gertatzen diren elkarrekintzez gain, molekula eta substratuaren artean ematen direnak ulertzea ere ezinbestekoa izanen da. Oraindik ere, hau zientziak duen erronka bat da. Lehen aipatu dugun bezala, molekulak eta atomoak gainazalean nola antolatuta dauden jakiteko STM-a erabili daiteke, baina azpian dirauten elkarrekintzak erakusteko in-situ teknika espektroskopikoak beharrezkoak dira. Honez gain, esperimentuen emaitzak azaltzerakoan kalkulu teorikoak oso baliogarriak suertatzen dira.

Izaera ezberdineko SAM-ak hazteko garaian, estrategia ezberdinak erabili izan dira. Hidrogeno loturen (H-lotura) bidez eraikitako molekula lauez osatutako sareetatik, geruza berezi batekiko kidetasuna azaltzen duten molekula-burudun konposatu kimikoetara. Moldatutako propietateak dituzten SAM-ak diseinatu ahal izateko, auto-antolaketa prozesua eragiten duten indarrak sakonki ulertu behar dira. Eratzen den geruzaren egitura finkatzeko garaian, sisteman parte hartzen duten elkarrekintzen indar erlatiboa garrantzitsua da oso. Molekula eta substratuaren arteko elkarrekintza molekulen arteko elkarrekintzarekin konparatuz ahula bada, adib. van der Waals indarrak *versus* H-loturak; geruzaren egitura batik bat molekulen arteko elkarrekintzek finkatuko dute. Molekula–substratu elkarrekintza molekulen artekoa baino indartsuagoa bada ostera, lotura kobalenteak *versus* van der Waals indarrak; azken honek ez du paper garrantzitsurik jokatuko eta SAM-aren neurria substratuarenarekin bat etorriko da. Azkenik, bai molekula–molekula, bai molekula–substratu arteko elkarrekintzak paretsuak badira, uraren kasuan bezala [11]; zein egitura agertuko den aurreratzea oso zaila gerta liteke.

Au(111) gainazalean jarritako geruza molekular mehen egitura geometriko eta pro-

pietate elektronikoen ikerketa teorikoa aurkezten da tesi honetan. Dentsitatearen funtzionalaren teoria (Density Functional Theory, DFT) erabiltzen duten *ab-initio* kalkuloak aurkezten dira bertan. Hauek emaitza esperimentalekin alderatu dira ahal den neurrian. Hiru sistema ezberdin aztertu dira xehetasunez: alkanetiol laburren adsortzio sendoa, emaile-hartzaile karga-transferentzi konplexuen adsortzioa, eta poliareno osagarri biren adsortzioa. Sistema hauen aukeraketa STM esperimentu batzuek sustatua izan arren, gure helburua ez da emaitza horiek azaltzea izan soilik; baizik eta geruza horien antolaketa prozesuaren eta propietate elektronikoen funtsean dagoen fisika ulertzea. Hori lortu ahal izateko, tresna teoriko ezberdinak erabili ditugu, hara nola, erlaxatutako geometria eta energia minimoen azterketa, induzitutako dentsitate elektronikoak, atomo eta orbital molekularren gain proiektatutako egoera dentsitatea (PDOS), banda egituraren kalkulua, etab.

Ikerketaren abiapuntua, Au(111) gainazalean dauden alkanetiolen jokaera, eta bereziki, STM irudietan ikusten den zig-zag egitura aztertzea izan da. Alkanetiolaren ezaugarri nagusia, sufrea duen molekula-buru bat, eta karbonoz zein hidrogenoz osatutako isats bat izatea da. Sufre-burua urrearekin lotzen den bitartean, isatsa zutik edo etzanda geratzen da inguruko molekula kopuruaren arabera. Geruza hauen eraketa, adsortzio lekuaren hautaketa eta ondoz-ondoko isatsen arteko indar ahuletan datza. Gure interesa jaso zuenak ordea, S–Au elkarrekintza berezia ulertzea izan da. Are eta gehiago, lan honen enborra S–Au elkarrekintza honen inguruan antolatu da, molekula–substratu elkarrekintzaren indar erlatiboari jarraituz: sendotik ahulera.

Ikerketan zehar erabilitako metodologia aurkeztu dugu tesiaren lehenengo kapituluan, eta hurrengo kapituluan S-Au lotura aztertu dugu. Horretarako, S–Au dimeroa, S atomoaren adsortzioa Au(111) gainazalean, eta baita SH eta SCH_3 molekulen adsortzioa Au(111)-n ere aztertu dira. Analisi sakon baten ostean, S–Au loturaren funtsa jadanik kasu sinpleenean, S–Au dimeroan, agertzen dela ikusi dugu. Beste dimero batzuekin alderatuz, lotura honen propietate bereizgarrien jatorria efektu erlatibistetan dagoela ondorioztatu dugu. S–Au lotura, bai dimeroan bai Au(111) gainazalean, S-ren $3p$ eta Au-ren $5d$ orbitalen artean elkarbanatutako kargak sortua da batez ere. Bi sistema horietan aldatzen dena, kargaren berrantolaketa da. Lotura kobalente sendo hau, DFT-n oinarritutako kalkuluak erabiltzeko oso aproposa da.

S-buruari isats molekular bat (–H edo $–CH_3$) gehitzeak ez ditu geruzaren propietate elektronikoak aldatzen. Kalkulatutako PDOS eta induzitutako dentsitateek, urrearen egoera elektronikoetatik molekularen beteriko azken orbitalera (HOMO), eta baita hutsik dagoen lehen orbitalera (LUMO) ere, karga transferentzia bat badagoela erakutsi digute. Hala ere, adsortzio geometriari so eginez badira aldeak. Azken urteotan SCH_3/Au(111)-ren inguruan ikasketa ugari izan arren, irekiak zirauten hainbat galderei kasu egin diegu lan honetan. Gure kalkuluak emaitza esperimentalekin alderatuz, molekula hau bridge-fcc

izeneko lekuan makurturik jartzen dela baietsi dugu. Gainera, T = 0 K-tan energia minimoko konfigurazioa ($\sqrt{3} \times \sqrt{3}$)R30° deritzonari dagokiola ondorioztatu izan ahal dugu, beste lan batzuek proposatzen zuten c(4×2) konfigurazioa arbuiatuz. Hala eta guztiz ere, bien arteko energia diferentzia oso txikia dela aipatzekoa da, eta zero ez diren tenperaturetan biak agertzeko aukera ez dugu ukatzen.

Jada aipatu dugun molekula–substratu elkarrekintzaren indar erlatiboaren irizpideari jarraituz, ondorengo kapitulua Au(111)-n gaineko TTF eta TCNQ molekulen adsortzioaz arduratu da. TTF-a bi S–Au loturen bidez gainazalera sendo lotzen da, alkanetiolek egiten duten antzera; TCNQ-k berriz, gainazalarekin elkarrekintza ahula duen H-loturen bitartez eraturiko sare bat osatzen du. Kapitulu honetan metal eta geruza organikoaren arteko interfazearen (metal-organiko interfazea) propietate elektronikoen azterketan arreta jarri da; Au(111) gainazala eta TTF-TCNQ geruzaren artean sortzen diren banda hibridoetan hain zuzen ere. DFT kalkuluei esker STM/STS esperimentuen emaitzak ulertu ditugu. Bi molekula hauek elkarrekin jartzean, etzanda kokatzen diren emaile–hartzaile konplexuak osatzen dituzte. STM irudiek erakusten dutenaren arabera, TTF eta TCNQ molekulek txandakako lerroez osaturiko 1:1 estekiometria duen geruza bat eratzen dute. Konduktantzia espektroetan bi trazu bereizgarri azaltzen dira: trazu estu bat TCNQ lerroetan eta beste trazu zabalago bat TTF gainean. Seinale hauen jatorria eta izaera tresna teoriko ezberdinei esker ulertu dugu. TCNQ-k azpiko gainazalaren eraginez aldaketarik jasaten ez badu ere, TTF-a Au(111)-ren egoera elektronikoekin dexente nahasten da. Honek, lerro molekularren artean potentzial periodiko ahul bat sortzen du, eta Brillouin gunearen mugan banaturiko bi interfaze-banda agertarazten ditu. Elektroi-askeen metal antzerako dispertsioa eta geruza organikoak bultzatutako anisotropia azaltzen dute interfaze-banda hauek. Batek, TTF gainean pilatzen du karga eta besteak berriz, TCNQ gainean. Halaber, banda hauek esperimentuan aurkitutako bi seinaleekin zuzenki erlazionatuta daude. Atal honetan zehar, banda metal-organiko hibridoen eraketa eskala molekularrean deskribatzen duen irudi kontzeptual bat aurkezten da. Hori, metal-organiko interfaze erabilgarriak diseinatu ahal izateko garrantzitsua da oso.

Azkenik, BDG eta NTCDI deritzen, amina eta imida talde kimiko osagarriak dituzten bi molekula lauen adsortzioa aztertu da. Hauen adsortzioak, bai banaka bai elkarrekin, 2D-tan antolatutako sare supramolekularrak sortzen dituela erakusten dute STM esperimentuek. BDG hutsa, NTCDI hutsa eta BDG-NTCDI nahasketaren kasuan urrea kontutan izan gabe kalkulatu ditugun geruzen geometriak STM irudietan ikusten direnekin bat egiten dute. H-loturen energi eta neurriei so eginez, ondoz-ondo dauden molekula lerroen arteko elkarrekintza indarra, lerroetan bertan dauden molekulen artekoa baina ahulagoa dela esan dezakegu. Molekula lau hauen eta Au(111) artean ematen den elkarrekintza oso ahula da eta ezin da DFT-ren bidez deskribatu. Hala ere, STM irudi errealistagoak simulatu ahal izateko, gainazal metalikoa seinale iturri bezala sartu dugu gure kalku-

luan. Simulazio hauen bidez, molekula bakoitza sarean nola kokatuta dagoen jakin ahal dugu. Bestalde, kapitulu honetan, kalkulu teorikoak neurtutako espektroak ulertzeko lagungarriak direla ere erakusten da. Teoria eta esperimentu konbinazioari esker, amina eta imida talde kimikoek bereizgarri bezala dituzten N eta O atomoen egoera elektronikoa deskribatu dugu zehatz-mehatz. Talde hauek egitura supramolekularrak lortu ahal izateko askotan erabiltzen direnez, beraien aztarna aurkitzeko gaitasuna izatea garrantzitsua dela iruditzen zaigu.

Ikertu ditugun sistema guztiek, Au(111) gainazala dute amankomunean. Hori dela eta, tesiaren eranskin batean gainazal metaliko honetaz arduratu gara. Gainazal egoera eta "herringbone" izeneko berreraiketa du Au(111)-k ezaugarritzat. Kasu askotan, ezaugarri bi horien aldaketak molekula–substratuaren arteko elkarrekintzaren aztarna jarraitzeko balio izaten du. Bestalde, Au(111)-ren gainazal egoeraren propietateak ezagunak direnez, gure kalkuluetan erabili dugun gainazal teorikoaren zehaztasuna ezagutzeko erreferentzia puntu bezala erabili dugu.

Bibliography

[1] G. E. Moore, *Electronics* 38(8), **1965**.

[2] R. P. Feynman, 'There's plenty of room at the bottom', First published in Engineering and Science magazine, no. 5, **1960**.

[3] N. Taniguchi, in *Proc. Intl. Conf. Prod. Eng.*, vol. Part II, Tokyo, **1974**. Japan Society of Precission Engineering.

[4] G. Binnig, H. Rohrer, *IBM J. Res. & Dev.* 30, 4, **1986**.

[5] S. Hecht, *Angew. Chem. Int. Ed.* 42, 24–26, **2003**.

[6] J. V. Barth, G. Constantini, K. Kern, *Nature* 437, 671–679, **2005**.

[7] J. V. Barth, *Annu. Rev. Phys. Chem.* 58, 375–407, **2007**.

[8] J.-M. Lehn, *Supramolecular Chemistry: Concepts and Perspectives*. VCH, Weinheim, Germany, **1993**.

[9] J.-M. Lehn, *Rep. Prog. Phys.* 67, 249–265, **2004**.

[10] F. Schreiber, *Pro. Surf. Sci.* 65, 151–256, **2000**.

[11] M. A. Henderson, *Surf. Sci, Rep.* 46, 1–308, **2002**.

[12] R. G. Parr, W. Yang, *Density Functional Theory of Atoms and Molecules*. Oxford University Press, New York, **1989**.

[13] R. M. Dreizler, E. K. U. Gross, *Density Functional Theory: An Approach to the Quantum Many-Body Problem*. Springer-Verlag, Berlin, **1990**.

[14] C. Fiolhais, F. Nogueira, M. Marques (eds.), *A primer in Density Functional Theory*, vol. 620. Springer, Lecture Notes in Physics, **2003**.

[15] K. Burke, 'The abc of dft', Department of Chemistry, Rutgers University, 610 Taylor Rd, Piscataway, NJ 08854, **2003**.

[16] K. Capelle, 'A bird's-eye view of density-functional theory', Departamento de Física e Informática, Universidade de São Paulo, **2005**.

[17] P. Hohenberg, W. Kohn, *Phys. Rev.* 136, B864, **1964**.

[18] D. R. Hartree, *Proc. Cambridge Phil. Soc.* 24, **1928**.

[19] P. M. A. Dirac, *Proc. Roy. Soc. London* 112, 661, **1926**.

[20] J. C. Slater, *Phys. Rev.* 34, 1293, **1929**.

[21] V. Fock, *Z. Phys.* 61, 126, **1930**.

[22] W. Khon, L. J. Sham, *Phys. Rev.* 140(4), A1133, **1965**.

[23] S. H. Vosko, L. Wilk, M. Nusair, *Can. J. Phys.* 58, 1200, **1980**.

[24] J. P. Perdew, A. Zunger, *Phys. Rev. B* 23, 5048, **1981**.

[25] J. P. Perdew, Y. Wang, *Phys. Rev. B* 45, 13244, **1993**.

[26] D. M. Ceperley, B. J. Alder, *Phys. Rev. Lett.* 45, 566, **1980**.

[27] J. P. Perdew, Y. Wang, *Phys. Rev. B* 33, 8800, **1986**.

[28] J. P. Becke, *Phys. Rev. A* 38, 3098, **1988**.

[29] C. Lee, W. Yang, R. G. Parr, *Phys. Rev. B* 37, 785, **1988**.

[30] J. P. Perdew, Y. Wang, *Phys. Rev. B* 45, 13244–13249, **1992**.

[31] J. P. Perdew, K. Burke, M. Ernzerhof, *Phys. Rev. Lett.* 77, 3865–3868, **1996**.

[32] G. Kresse, J. Hafner, *Phys. Rev. B* 49(20), 14251, **1994**.

[33] G. Kresse, J. Furthmüller, *Phys. Rev. B* 54(16), 11169, **1996**.

[34] D. Vanderbilt, *Phys. Rev. B* 41, 7892, **1990**.

[35] P. E. Blochl, *Phys. Rev. B* 50(24), 17953, **1994**.

[36] N. W. Ashcroft, N. D. Mermin, *Solid State Physics*. Harcourt College, **1976**.

[37] R. M. Martin, *Electronic Structure*. Cambridge University Press, **2004**.

[38] H. J. Monkhorst, J. D. Pack, *Phys. Rev. B* 13(12), 5188–5192, **1976**.

[39] G. Chiarotti, *Numerical Data and Functional Relationships in Science and Technology - New Series, Group III Condensed Matter*, vol. 24a. Springer, Heidelberg, **1993**.

[40] R. Hoffmann, *Rev. Mod. Phys.* 60(3), 601, **1988**.

[41] N. Lorente, M. Persson, *Faraday Discuss.* 117, 277–290, **2000**.

[42] N. Lorente, M. F. G. Hedouin, R. E. Palmer, M. Persson, *Phys. Rev. B* 68, 155401, **2003**.

[43] C. Bai, *Scanning Tunneling Microscopy and Its Applications*. Springer Series in Surface Science, 2nd edn., **1999**.

[44] J. Bardeen, *Phys. Rev. Lett.* 6(2), 57–59, **1961**.

[45] J. Tersoff, D. R. Hamann, *Phys. Rev. B* 31(2), 805, **1985**.

[46] R. S. Mulliken, *J. Chem. Phys.* 23, 1841, **1955**.

[47] R. F. W. Bader, *Atoms in Molecules – A Quantum Theory*. Oxford University Press, Oxford, **1990**.

[48] R. F. W. Bader, P. L. A. Popelier, T. A. Kleith, *Angew. Chem. Int. Ed.* 33, 620, **1994**.

[49] G. Henkelman, A. Arnaldsson, H. Jónsson, *Comput. Mater. Sci.* 36, 254–360, **2006**.

[50] E. Sanville, S. D. Kenny, R. Smith, G. Henkelman, *J. Comp. Chem.* 28, 899–908, **2007**.

[51] H. Basch, M. A. Ratner, *J. Chem. Phys.* 119(22), 11926, **2003**.

[52] F. Schreiber, *J. Phys.: Condens. Matter* 16, R881–R900, **2004**.

[53] J. C. Love, L. A. Estroff, J. K. Kriebel, R. G. Nuzzo, G. M. Whitesides, *Chem. Rev.* 105, 1103–1169, **2005**.

[54] Y. Akinaga, T. Nakajima, K. Hirao, *J. Chem. Phys.* 114(19), 8555, **2001**.

[55] E. Barrena, E. Palacios-Lidón, C. Munuera, X. Torrelles, S. Ferrer, U. Jonas, M. Salmeron, C. Ocal, *J. Am. Chem. Soc.* 126(1), 385–395, **2004**.

[56] C. Vericat, M. E. Vela, R. C. Salvarezza, *Phys. Chem. Chem. Phys.* 7, 3258–3268, **2005**.

[57] F. P. Cometto, P. Paredes-Olivera, V. A. Macagno, E. M. Patrito, *J. Phys. Chem. B* 109, 21737–21748, **2005**.

[58] M. Konôpka, R. Rousseau, I. Stich, D. Marx, *Phys. Rev. Lett.* 95, 096102, **2005**.

[59] G. Heimel, L. Romaner, J.-L. Brédas, E. Zojer, *Surf. Sci.* 600, 4548–4562, **2006**.

[60] P. G. Lustemberg, M. L. Martiarena, A. E. Martínez, H. F. Busnengo, *Langmuir* 24, 3274–3279, **2008**.

[61] J. Zhou, F. Hagelberg, *Phys. Rev. Lett.* 97, 045505, **2006**.

[62] I. I. Rzeźnicka, J. Lee, P. Maksymovych, J. J. T. Yates, *J. Phys. Chem. B* 109(33), 15992–15996, **2005**.

[63] G. J. Kluth, C. Carraro, R. Maboudian, *Phys. Rev. B* 59(16), 10449, **1999**.

[64] M. C. Vargas, P. Giannozzi, A. Selloni, G. Scoles, *J. Phys. Chem. B* 105, 9509–9513, **2001**.

[65] Y. Yourdshahyan, A. M. Rappe, *J. Chem. Phys.* 117(2), 825, **2002**.

[66] M. G. Roper, M. P. Skegg, C. J. Fisher, J. J. Lee, V. R. Dhanak, D. P. Woodruff, R. G. Jones, *Chem. Phys. Lett.* 389, 87–91, **2004**.

[67] M. Yu, N. Bovet, C. J. Satterley, S. Bengió, K. R. J. Lovelock, P. K. Milligan, R. G. Jones, D. P. Woodruff, V. Dhanak, *Phys. Rev. Lett.* 97, 166102, **2006**.

[68] P. Maksymovych, D. C. Sorescu, J. J. T. Yates, *Phys. Rev. Lett.* 97, 146103, **2006**.

[69] R. Mazzarello, A. Cossaro, A. Verdini, R. R. ad L. Casalis, M. F. Danisman, L. Floreano, S. Scandolo, A. Morgante, G. Scoles, *Phys. Rev. Lett.* 98, 016102, **2007**.

[70] N. Gonzalez, N. Lorente, A. Arnau, *Surf. Sci.* 600, 4039–4043, **2006**.

[71] N. Gonzalez-Lakunza, N. Lorente, A. Arnau, *J. Phys. Chem. C* 111(33), 12383–12390, **2007**.

[72] P. Pyykkö, J.-P. Desclaux, *Acc. Chem. Research* 122, 276, **1979**.

[73] P. Pyykkö, *Angew. Chem. Int. Ed.* 43, 4412–4456, **2004**.

[74] P. Pyykkö, *Inorg. Chim. Acta* 358, 4113–4130, **2005**.

[75] D. J. Gorin, F. D. Toste, *Nature* 446, 395–403, **2007**.

[76] L. Strong, G. M. Whitesides, *Langmuir* 4, 546, **1988**.

[77] C. E. D. Chidsey, D. N. Loiacono, *Langmuir* 6, 682, **1990**.

[78] L. H. Dubois, R. G. Nuzzo, *Annu. Rev. Phys. Chem.* 43, 437, **1992**.

[79] L. H. Dubois, B. R. Zegarski, R. G. Nuzzo, *J. Chem. Phys.* 98, 678, **1993**.

[80] P. Fenter, A. Eberhardt, P. Eisenberger, *Science* 266, 1216, **1994**.

[81] E. Paradis, P. Rowntree, *J. Electroanal. Chem.* 550–551, 175–185, **2003**.

[82] F. T. Arce, M. E. Vela, R. C. Salvarezza, A. J. Arvia, *J. Chem. Phys.* 109, 5703, **1998**.

[83] G. E. Poirier, M. J. Tarlov, *Langmuir* 10, 2853, **1994**.

[84] E. Delamarche, B. Michel, C. Gerber, D. Anselmetti, H.-J. Güntherodt, H. Wolf, H. Ringsdorf, *Langmuir* 10, 2869, **1994**.

[85] J. P. Bucher, L. Santesson, K. Kern, *Appl. Phys. A* 59, 135, **1994**.

[86] Y. Morikawa, T. Hayashi, C. C. Liew, H. Nozoye, *Surf. Sci.* (507–510), 46–50, **2002**.

[87] P. Pyykkö, *Angew. Chem. Int. Ed.* 41, 3573–3578, **2002**.

[88] L. Pauling, *The Nature of the Chemical Bond and the Structure of Molecules and Crystals: An Introduction to Modern Structural Chemistry*. Cornell Univ. Press, Ithaca, NY, 3rd ed. edn., **1960**.

[89] A. L. Allred, *J. Inorg. Nucl. Chem.* 17, 215, **1961**.

[90] J. Gottschalck, B. Hammer, *J. Chem. Phys.* 116(2), 784, **2002**.

[91] J. A. Rodriguez, J. Dvorak, T. Jirsak, G. Liu, J. Hrbek, Y. Aray, C. Gónzalez, *J. Am. Chem. Soc.* 125(1), 276–285, **2003**.

[92] G. S. Karlberg, *Phys. Rev. B* 74, 153414, **2006**.

[93] T. Hayashi, Y. Morikawa, H. Nozoye, *J. Chem. Phys.* 114(17), 7615, **2001**.

[94] Y. Cao, Q. Ge, D. J. Dyer, L. Wang, *J. Phys. Chem. B* 107, 3803–3807, **2003**.

[95] P. Maksymovych, D. C. Sorescu, J. J. T. Yates, *J. Phys. Chem. B* 110, 21161–21167, **2006**.

[96] A. Ulman, *Chem. Rev.* 96, 1533, **1996**.

[97] H. Grönbeck, A. Curioni, W. Andreoni, *J. Am. Chem. Soc.* 122(16), 3839–3842, **2000**.

[98] L. M. Molina, B. Hammer, *Chem. Phys. Lett.* 360, 264–271, **2002**.

[99] A. Ferral, P. Paredes-Olivera, V. A. Macagno, E. M. Patrito, *Surf. Sci.* 525, 85–99, **2003**.

[100] H. Kondoh, H. Nozoye, *J. Phys. Chem. B* 102, 2367–2372, **1998**.

[101] C. Corriol, F. Calleja, A. Arnau, J. J. Hinarejos, A. L. V. de Parga, W. A. Hofer, R. Miranda, *Chem. Phys. Lett.* 405, 131–135, **2005**.

[102] N. Camillone III, C. E. D. Chidsey, G.-Y. Liu, G. J. Scoles, *J. Chem. Phys.* 98, 3503, **1993**.

[103] P. Fenter, P. Eisenberger, K. S. Liang, *Phys. Rev. Lett.* 70, 2447, **1993**.

[104] P. Fenter, F. Schreiber, L. Berman, G. Scoles, P. Eisenberger, M. J. Bedzyk, *Surf. Sci.* 412/413, 213–235, **1998**.

[105] G. E. Poirier, W. P. Fitts, J. M. White, *Langmuir* 17, 1176, **2001**.

[106] W. P. Fitts, G. E. Poirier, J. M. White, *Langmuir* 18, 2096, **2002**.

[107] S. R. Forrest, *Chem. Rev.* 97, 1793, **1997**.

[108] C. W. Tang, S. A. Slyke, *Appl. Phys. Lett.* 51, 913, **1987**.

[109] J. H. Burroughes, D. D. C. Bradley, A. R. Brown, R. N. Marks, K. Mackay, R. H. Friend, P. L. Burns, A. B. Holmes, *Nature* 347, 539–541, **1990**.

[110] M. Granstrom, K. Petritsch, A. C. Arias, A. Lux, M. R. Andersson, R. H. Friend, *Nature* 395, 257–260, **1998**.

[111] P. Peumans, S. R. Forrest, *App. Phys. Let.* 79, 126–128, **2001**.

[112] P. Peumans, S. Uchida, S. R. Forrest, *Nature* 425, 158–162, **2003**.

[113] C. D. Dimitrakopoulos, D. J. Mascaro, *IBM J. Res. & Dev.* 45(1), 11–27, **2001**.

[114] C. D. Dimitrakopoulos, P. R. L. Malenfant, *Adv. Mat.* 14, 99, **2002**.

[115] C. R. Kagan, D. B. Mitzi, C. D. Dimitrikopoulos, *Science* 286, 945, **1999**.

[116] X.-Y. Zhu, *Surf. Sci. Rep.* 56, 1–83, **2004**.

[117] H. Ishii, K. Sugiyama, E. Ito, K. Seki, *Adv. Mat.* 11(8), 605–625, **1999**.

[118] A. Kahn, N. Koch, W. Gao, *J. Polym. Sci., Part B: Polym. Phys.* 41, 2529, **2003**.

[119] R. Temirov, S. Soubatch, A. Luican, F. S. Tautz, *Nature* 444, 350–353, **2006**.

[120] N. Nicoara, E. Román, J. M. Gómez-Rodríguez, J. A. Martín-Gago, J. Méndez, *Org. Elect.* 7, 287–294, **2006**.

[121] S. Lukas, G. Witte, C. Wöll, *Phys. Rev. Lett.* 88(2), 028301, **2002**.

[122] Y. Pennec, W. Auwärter, A. Schiffrin, A. Weber-Bargioni, A. Riemann, J. V. Barth, *Nat. Nanotech.* 2, 99, **2007**.

[123] A. Ferretti, C. Baldacchini, A. Calzolari, R. D. Felice, A. Ruini, E. Molinari, M. G. Betti, *Phys. Rev. Lett.* 99(4), 046802, **2007**.

[124] J. Ferreris, D. O. Cowan, V. W. Jr., J. H. Perlstein, *J. Am. Chem. Soc.* 95(3), 948–949, **1973**.

[125] N. Koch, A. Vollmer, I. Salzmann, B. Nickel, H. Weiss, J. P. Rabe, *Phys. Rev. Lett.* 96, 156803, **2006**.

[126] G. Koller, S. Berkebile, M. Oehzelt, P. Puschnig, C. Ambrosch-Draxl, F. P. Netzer, M. G. Ramsey, *Science* 317, 351–355, **2007**.

[127] N. Toyota, M. Lang, J. Müller, *Low-dimensional molecular metals*. Springer, **2007**.

[128] A. J. Berlinsky, J. F. Carolan, L. Weiler, *Can. J. Chem.* 52(19), 3373–3377, **1974**.

[129] R. N. Compton, C. D. Cooper, *J. Chem. Phys.* 66, 4325, **1977**.

[130] M. Sing, U. Schwingenschlögl, R. Claessen, P. Blaha, J. M. P. Carmelo, M. Martelo, P. D. Sacramento, M. Dressel, C. S. Jacobsen, *Phys. Rev. B* 68, 125111, **2003**.

[131] T. J. Kistenmacher, T. E. Phillips, D. O. Cowan, *Struct. Cryst. Cryst. Chem.* 30(3), 763–768, **1974**.

[132] N. Ara, A. Kawazu, H. Shigekawa, K. Yase, M. Yoshimura, *App. Phys. Lett.* 66(24), 3278, **1995**.

[133] D. Jérome, *Chem. Rev.* 104(11), 5565–5592, **2004**.

[134] J. Fraxedas, *Molecular Organic Materials: From Molecules to Crystalline Solids*. Cambridge University Press, Cambridge, England, **2006**.

[135] F. Zwick, D. Jérome, G. Margaritondo, M. Onellion, J. Voit, M. Grioni, *Phys. Rev. Lett.* 81(14), 2974–2977, **1998**.

[136] W. Shockley, *Phys. Rev.* 56, 317–323, **1939**.

[137] I. Fernández-Torrente, *Local Spectroscopy of bi-molecular assemblies: screening, charge transfer, and magnetism at the molecular scale*, Ph.D. thesis, Department of Physics of the Freie Universität Berlin, **2008**.

[138] I. Horcas, R. Fernández, J. M. Gómez-Rodríguez, J. Colchero, J. Gómez-Herrero, A. M. Baró, *Rev. Sci. Inst.* 78, 013705, **2007**.

[139] I. Fernández-Torrente, S. Monturet, K. J. Franke, J. Fraxedas, N. Lorente, J. I. Pascual, *Phys. Rev. Lett.* 99, 176103, **2007**.

[140] I. Fernández-Torrente, K. J. Franke, J. I. Pascual, *Int. J. Mass Spectrom.* 277, 269–273, **2008**.

[141] J. Repp, G. Meyer, S. M. Stojković, A. Gourdon, C. Joachim, *Phys. Rev. Lett.* 94(2), 26803, **2005**.

[142] G. A. Jeffrey, *An Introduction to Hydrogen Bonding*. Oxford University Press, Oxford, **1997**.

[143] T. Steiner, *Angew. Chem. Int. Ed.* 41, 48–76, **2002**.

[144] F. Foster, G. Nicolay, F. Reinert, D. Ehm, S. Schmidt, S. Hüfner, *Surf. Sci.* 532, 160–165, **2003**.

[145] J. Repp, G. Meyer, K. H. Rieder, *Phys. Rev. Lett.* 92, 036803, **2004**.

[146] H. Vázquez, R. Oszwaldowski, P. Pou, J. Ortega, R. Pérez, F. Flores, K. Kahn, *Europhys. Lett.* 65(6), 802–808, **2004**.

[147] N. Gonzalez-Lakunza, I. Fernández-Torrente, K. J. Franke, N. Lorente, A. Arnau, J. I. Pascual, *Phys. Rev. Lett.* 100, 156805, **2008**.

[148] Y. Hasegawa, P. Avouris, *Phys. Rev. Lett.* 71(7), 1071–1074, **1993**.

[149] F. Reinert, G. Nicolay, S. Schmidt, D. Ehm, S. Hüfner, *Phys. Rev. B* 63, 115415, **2001**.

[150] C. D. Lindstrom, M. Muntwiler, X. Y. Zhu, *J. Phys. Chem. B* 109, 21492, **2005**.

[151] C. Kittel, *Introduction to Solid State Physics*. John Wiley & Sons, New York, 5th edn., **1976**.

[152] R. F. Service, P. Szuromi, J. Uppenbrink, *Science* 295, 2395–2491, **2002**.

[153] S. Xu, M. Dong, E. Rauls, R. Otero, T. R. Linderoth, F. Besenbacher, *Nano Lett.* 6, 1434–1438, **2006**.

[154] J. A. Theobald, N. S. Oxtoby, M. A. Philips, N. R. Champness, P. H. Beton, *Nature* 424, 1029–1031, **2003**.

[155] L. M. A. Perdigão, E. W. Perkins, J. Ma, P. A. Stainec, B. L. Rogers, N. R. Champness, P. H. Beton, *J. Phys. Chem. B* 110, 12539–12542, **2006**.

[156] S. M. Barlow, R. Raval, *Surf. Sci. Rep.* 50, 201–341, **2003**.

[157] P. Jonkheijm, A. Miura, M. Zdanowska, F. J. M. Hoeben, S. D. Feyter, A. P. H. J. Schenning, F. C. D. Schryver, E. W. Meijer, *Angew. Chem. Int. Ed.* 43, 74–78, **2004**.

[158] M. Stöhr, M. Wahl, C. H. Galka, T. Riehm, T. A. Jung, L. H. Gade, *Angew. Chem. Int. Ed.* 44, 7394–7398, **2005**.

[159] M. Ruiz-Osés, N. Gonzalez-Lakunza, I. Silanes, A. Gourdon, A. Arnau, J. E. Ortega, *J. Phys. Chem. B* 110, 25573–25577, **2006**.

[160] M. E. Cañas-Ventura, W. Xiao, D. Wasserfallen, K. Müllen, H. Brune, J. V. Barth, R. Fasel, *Angew. Chem. Int. Ed.* 46, 1814–1818, **2007**.

[161] S. Clair, S. Pons, H. Brune, K. Kern, J. V. Barth, *Angew. Chem. Int. Ed.* 44, 7294–7297, **2005**.

[162] V. Repain, G. Baudot, H. Ellmer, S. Rousset, *Europhys. Lett.* 58, 730–736, **2002**.

[163] J. Kuntze, A. Mugarza, J. E. Ortega, *Appl. Phys. Lett.* 81, 2463–2465, **2002**.

[164] C. R. Newman, D. Frisbie, D. A. da Silva Filho, J.-L. Bredas, P. C. Ewbank, K. R. Mann, *Chem. Mater.* 16, 4436, **2004**.

[165] M. J. Frisch, et al., *Gaussian 03*, Gaussian Inc., Wallindorf CT, revision c.02 edn., **2004**.

[166] M. Ruiz-Osés, D. G. de Oteiza, I. Fernández-Torrente, N. Gonzalez-Lakunza, T. Kampen, K. Horn, A. Gourdon, A. Arnau, J. E. Ortega, *Submitted* , **2008**.

[167] D. L. Keeling, N. S. Oxtoby, C. Wilson, M. J. Humphry, N. R. Champness, P. H. Beton, *Nano Lett.* 3, 9–12, **2003**.

[168] E. Barrena, D. G. de Oteiza, H. Dosch, Y. Wakayama, *ChemPhysChem* 8, 1915–1918, **2007**.

[169] A. Hotzel, G. Moos, K. Ishioka, M. Wolf, G. Ertl, *Appl. Phys. B* 68, 615–622, **1999**.

[170] S. Rousset, F. Pourmir, J. M. Berroir, J. Klein, J. Lecoeur, P. Hecquet, B. Salanon, *Surf. Sci.* 422, 33–41, **1999**.

[171] M. Ruiz-Osés, T. Kampen, N. Gonzalez-Lakunza, I. Silanes, P. M. Schmidt, A. Gourdon, A. Arnau, K. Horn, J. E. Ortega, *ChemPhysChem* 8, 1722–1726, **2007**.

[172] http://www-ssrl.slac.stanford.edu/nexafs.html.

[173] J. Stör, *NEXAFS spectroscopy, Springer Series in Surface Sciences*. Springer, Heidelberg, **2003**.

[174] S. Portmann, H. P. Lüthi, *MOLEKEL: An interactive Molecular Graphics Tool; CHIMIA* 54, 766–770, **2000**.

[175] J. Perderau, J. P. Biberian, G. E. Rhead, *J. Phys. F: Met. Phys.* 4, 798, **1974**.

[176] H. Melle, E. Menzel, Z. Naturforsch, *A* 33, 282, **1978**.

[177] M. A. van Hove, R. J. Koestner, P. C. Stair, J. P. Biberian, L. L. Kesmodel, I. Bartos, G. A. Somorjai, *Surf. Sci.* 103, 189, **1981**.

[178] K. Takayanagi, K. Yagi, *Trans. Jpn. Ins. Met.* 24, 337, **1983**.

[179] U. Harten, A. M. Lahee, J. P. Toennies, C. Wöll, *Phys. Rev. Lett.* 54, 2619, **1985**.

[180] C. Wöll, S. Chiang, R. J. Wilson, P. H. Lippel, *Phys. Rev. B* 39, 7988, **1989**.

[181] K. G. Huang, D. Gibbs, D. M. Zehner, A. R. Sandy, S. G. J. Mochrie, *Phys. Rev. Lett.* 65, 3313, **1990**.

[182] J. V. Barth, H. Brune, G. Ertl, R. J. Behm, *Phys. Rev. B* 42, 9307, **1990**.

[183] D. D. Chambliss, R. J. Wilson, S. Chiang, *Phys. Rev. Lett.* 66, 1721, **1991**.

[184] P. Heimann, H. Neddermeyer, *J. Phys. F: Met. Phys.* 7, L37–L42, **1977**.

[185] I. E. Tamm, *Z. Phys.* 76, 849, **1932**.

[186] W. Chen, V. Madhavan, T. Jamneala, M. C. Crommie, *Phys. Rev. Lett.* 80(7), 1469–1472, **1998**.

[187] M. F. Crommie, C. P. Lutz, D. M. Eigler, *Nature* 363, 524, **1993**.

[188] N. Takeuchi, C. T. Chan, K. M. Ho, *Phys. Rev. B* 43(17), 13899–13906, **1991**.

Publications

Part of the work described in this thesis has been published in the following publications:

- **Non-covalent interactions in supramolecular assemblies investigated with electron spectroscopies**
  M. Ruiz-Osés, D. G. de Oteiza, I. Fernández-Torrente, N. Gonzalez-Lakunza, T. Kampen, K. Horn, A. Gourdon, A. Arnau, J. E. Ortega;
  Submitted to Advanced Materials

- **Formation of Dispersive Hybrid Bands at an Organic-Metal Interface**
  N. Gonzalez-Lakunza, I. Fernández-Torrente, K. J. Franke, N. Lorente, A. Arnau, J. I. Pascual;
  Phys. Rev. Lett. 100, 156805, **2008**

- **Spectroscopic fingerprints of amine and imide functional groups in supramolecular monolayers**
  M. Ruiz-Osés, T. Kampen, N. Gonzalez-Lakunza, I. Silanes, P. M. Schmidt, A. Gourdon, A. Arnau, K. Horn, J. E. Ortega;
  ChemPhysChem 8, 1722–1726, **2007**

- **Chemisorption of sulphur and sulphur-based simple molecules on Au(111)**
  N. Gonzalez-Lakunza, N. Lorente, A. Arnau;
  J. Phys. Chem. C 111, 12383–12390, **2007**

- **Self-assembly of Heterogeneous Supramolecular Structures with Uniaxial Anisotropy**
  M. Ruiz-Osés, N. Gonzalez-Lakunza, I. Silanes, A. Gourdon, A. Arnau, J. E. Ortega;
  J. Phys. Chem. B 110, 25573–25577, **2006**

- **Methylthiolate adsorption on Au(111): energetics, vibrational modes and STM imaging**
  N. Gonzalez-Lakunza, N. Lorente, A. Arnau;
  Surf. Sci. 600, 4039–4043, **2006**